

# 1

## Crystal Chemistry of Cobalt Oxides

### 1.1 Introduction

Most of the advances in the knowledge of the properties of materials have been the outcome of a systematic observation of the properties of closely related materials, this is because of the fact that often small crystal or microstructural differences are associated with marked changes in physical properties. Thus, prior to the investigation of physical properties, it is very essential to pay attention to the structural features and the relationship between crystal structure and electronic properties. In this regard, we will sum up the structural features of different types of cobalt oxides and the related factors influencing the crystal structure.

Like manganese, iron, and copper, cobalt exhibits several possible oxidation states –  $\text{Co}^{2+}$ ,  $\text{Co}^{3+}$ , and  $\text{Co}^{4+}$  – and several types of coordinations, that is, tetrahedral, pyramidal, and octahedral. Consequently, cobalt oxides offer a wide field for the creation of many frameworks, not only stoichiometric oxides but also nonstoichiometric oxides, involving a mixed valency of cobalt and/or the presence of oxygen vacancies. A property which distinguishes the cobalt oxides from other 3d metal oxides deals with the ability of cobalt to be present in various spin states, that is, low spin (LS), high spin (HS), and intermediate spin (IS). These probable spin states make the physics of the cobalt oxides so complicated that it has not been completely understood so far. The complexity in spin state originates from the fact that the crystal field splitting  $\Delta_{\text{cf}}$  of the 3d energy level of the cobalt ion in cobalt oxides is of the same order of magnitude as the Hund's rule intraatomic exchange energy  $J_{\text{H}}$  and the 3d-orbital bandwidth. In cobalt oxides, the selection decided by the Hund's coupling makes that  $\text{Co}^{2+}$  is always in high-spin state  $t_{2g}^5 e_g^2$  ( $S = 3/2$ ), whereas  $\text{Co}^{4+}$  usually adopts the low-spin state  $t_{2g}^5 e_g^0$  ( $S = 1/2$ ) due to the crystal field splitting. In contrast, for  $\text{Co}^{3+}$  the three different spin states are possible, that is, low-spin  $t_{2g}^6 e_g^0$  ( $S = 0$ ), high-spin  $t_{2g}^4 e_g^2$  ( $S = 2$ ), and intermediate spin  $t_{2g}^5 e_g^1$  ( $S = 1$ ) due to the fact that  $\Delta_{\text{cf}}$  is very sensitive to changes in the Co–O bond length and Co–O–Co bond angle, modifying easily the spin state of  $\text{Co}^{3+}$ . Spin state transitions can, therefore, be easily provoked by varying the temperature and the pressure, applying a magnetic field and photon and/or by tuning the structural parameters (oxygen content and type of counteraction) of the material.

The spin state of cobalt ions is influenced by the valence state and coordination number and all the three have a primordial role in the manifestation of intriguing physical and structural properties. Interestingly, the peculiar feature of cobalt oxides is that the cobalt ions exhibit different functionality in their different valence states. In a divalent  $\text{Co}^{2+}$  ion, in its high-spin state an electron is easily localized on the site forming a small polaron. Owing to the small transfer energy of the  $t_{2g}$  bands, it is difficult for an electron located on  $\text{Co}^{2+}$  to hop to the high-spin  $\text{Co}^{3+}$ . It also cannot hop to a  $\text{Co}^{3+}$  ion in the low-spin state since it is associated with a huge spin flip from  $S = 3/2$  to  $S = 0$ . This drives the pure  $\text{Co}^{2+}$  oxides to be magnetic insulators, while for the intermediate valence between  $\text{Co}^{2+}$  and  $\text{Co}^{3+}$ , carriers are often confined to the  $\text{Co}^{2+}$  sites. This makes a mixed  $\text{Co}^{2+}/\text{Co}^{3+}$  system to be sensitive for charge segregation and charge and/or spin ordering. As a consequence, the cobalt oxides having a cobalt valence state in between +3 and +2 often exhibit high dielectric constants. On the other hand,  $\text{Co}^{4+}$  in the low-spin state is chemically much less stable. The oxygen ligand hole is likely to exist in the  $\text{Co}^{4+}$  system. The ligand hole tends to be itinerant and ferromagnetic metallic compounds are often realized in the intermediate valence between  $\text{Co}^{3+}$  and  $\text{Co}^{4+}$ . Another interesting feature of the  $\text{Co}^{4+}$  valence state is the large entropy associated with the hole in  $t_{2g}^5$  level that causes a large thermopower. Thus, thermoelectric cobalt oxides can be realized in systems with cobalt valences intermediate between  $\text{Co}^{3+}$  and  $\text{Co}^{4+}$ . In the case of pure  $\text{Co}^{3+}$  oxides, the close competition between the crystal field splitting and the on-site exchange interaction often induces spin state transitions and/or crossover against temperature and pressure as will be shown further for  $\text{LaCoO}_3$ . This is an important difference between the cobalt oxides and the manganese oxides, where  $\text{Mn}^{3+}$  always remains in high-spin state.

The common way of the appearance of different valence states from a prevailing valence state is the disproportionation reaction, that is,  $2\text{Co}^{3+} \leftrightarrow \text{Co}^{2+} + \text{Co}^{4+}$  that plays a profound role in the electrical conduction and magnetic properties and will be discussed later. Again, since the sizes of the ions in different valence state are not similar, they influence the lattice energy, which in turn affects the physical and structural properties.

The valence state describes the number of electrons available to fill the energy bands. The electron (or hole) concentration is equivalent to the cobalt valence state and it may change linearly as shown, for example, in the  $\text{Ln}_{1-x}\text{A}_x\text{CoO}_3$  perovskite. It is the primary cause of changes in electronic behavior because the  $\text{Ln}^{3+}$  and  $\text{A}^{2+}$  ions do not contribute to the states around the Fermi level. As the hole concentration increases from  $x > 0$ , the nonmagnetic insulating state gives way to the ferromagnetic metallic state; this feature of cobaltites is reminiscent of manganites.

## 1.2 Stoichiometric Perovskites $\text{LnCoO}_3$

The studies on structural details of the class of rare-earth cobaltites  $\text{LnCoO}_3$  ( $\text{Ln} = \text{yttrium or lanthanide}$ ) were started long back and have been reviewed in

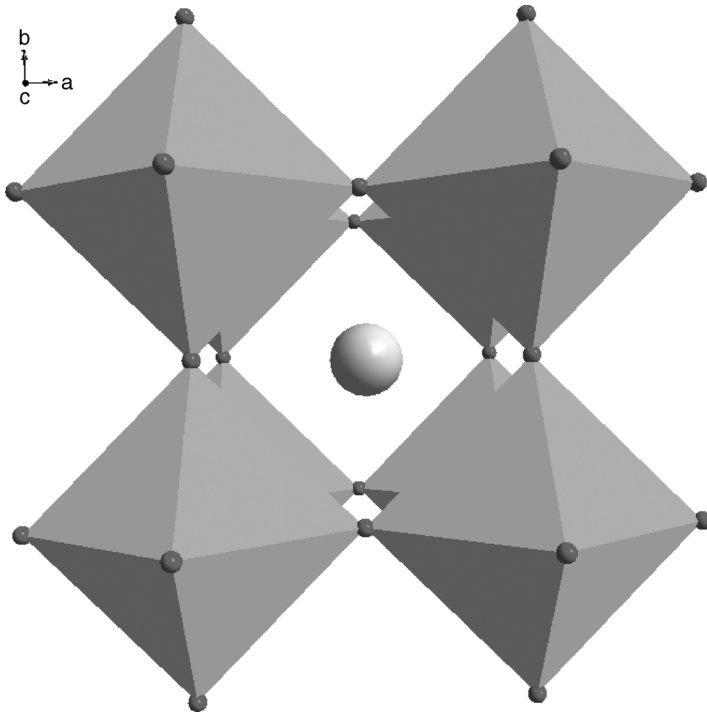


**Figure 1.1** Ideal cubic structure of the perovskite  $\text{LnCoO}_3$ .

subsequent reports [1–9]. None of the  $\text{LnCoO}_3$  stoichiometric oxides exhibits the ideal cubic perovskite structure characterized by  $Pm\bar{3}m$  space group (Figure 1.1).

All the cobaltites of the series  $\text{Ln} = \text{Pr}$  to  $\text{Lu}$  and  $\text{Y}$  show an orthorhombic distortion of the perovskite cell characterized by the space group  $Pbnm$  (or the equivalent group  $Pnma$  obtained by exchanging crystallographic axes) [10–15].

The magnitude of distortion depends on the kind of  $\text{Ln}^{3+}$  ions. For example,  $\text{NdCoO}_3$  shows a very small distortion and crystallizes in an almost cubic structure. In all the compounds, the cobalt ion is surrounded by weakly distorted oxygen  $\text{CoO}_6$  octahedra, whereas the rare-earth ions are in somewhat distorted cubo-octahedra formed of 12 oxygen ions (Figure 1.1). Of the 12  $\text{Ln}-\text{O}$  bonds, 3 are long bonds, 6 are medium-length bonds, and the rest 3 are short bonds. The cell volume change follows the lanthanide contraction. The structure is very sensible to the change in temperature. The magnitude of structural distortions changes significantly with the change in temperature.

The crystal structure of  $\text{LaCoO}_3$  is different from all the other members of the  $\text{LnCoO}_3$  series. At room temperature,  $\text{LaCoO}_3$  has a rhombohedrally distorted cubic perovskite structure whose unit cell belongs to the spatial group  $R\bar{3}c$ ,  $D_{3d}^6$  and has two formulas per unit cell. However, a monoclinic distortion of the structure (space group  $I2/a$ ) was found recently in  $\text{LaCoO}_3$  [16, 17].

It is well established that with the decrease in ionic radius of A cation the perovskite changes from higher to lower symmetry like cubic to orthorhombic.

The  $\text{BO}_6$  octahedra rotate about the  $b$ -axis in mostly encountered space group  $Pbnm$ , making  $b > a$ . It was shown that beyond a critical ionic radius, a distortion of the  $\text{BO}_6$  octahedra takes place, which inverts  $b > a$  to  $a > b$  before the perovskite transforms from orthorhombic  $Pbnm$  to rhombohedral  $R-3c$  symmetry [18]. The  $\text{LnCoO}_3$  family is one of the few that exhibits the  $Pbnm$  to  $R-3c$  crossover with increasing ionic radius:  $\text{LaCoO}_3$  has a rhombohedral symmetry and  $b > a$  in orthorhombic  $\text{NdCoO}_3$  changes to  $a > b$  in orthorhombic  $\text{PrCoO}_3$  [19].

With the increase in ionic radius,  $V$  is increased continuously while the orthorhombic splitting with  $b > c/\sqrt{2} > a$  is reduced progressively, becoming pseudo-cubic at  $\text{Ln} = \text{Nd}$  and then turning to  $a > c/\sqrt{2} > b$  for  $\text{Ln} = \text{Pr}$  before transforming to the rhombohedral  $R-3c$  structure in  $\text{Ln} = \text{La}$ . The increasing rotation of the  $\text{CoO}_6$  octahedra with decreasing ionic radius reduces  $\langle \theta \rangle$  from  $180^\circ$  in the ideal cubic perovskite to  $164\text{--}146^\circ$  in  $\text{LnCoO}_3$ . On the other hand,  $\langle \text{Co-O} \rangle$  remains almost constant except for  $\text{Ln} = \text{La}$ , with a broad maximum at  $r_{\text{Ln}} = 1.1 \text{ \AA}$ . The substitution for  $\text{La}^{3+}$  of an  $\text{Ln}^{3+}$  ion of smaller ionic radius introduces a chemical pressure on the  $\text{CoO}_3$  array that allows cooperative rotations of  $\text{CoO}_6$  octahedra, which relieve the compressive stress on the  $\text{Co-O}$  bond. Consequently, the  $\text{Co-O}$  bond length changes little with ionic size [19].

The evolution of the structure of these cobaltites versus temperature is of vital importance since it governs their physical properties, especially magnetism and transport properties. For this reason, numerous investigations have been carried out in this field.

The neutron diffractions study of  $\text{LaCoO}_3$  versus temperature [20] showed that there is no deviation from the  $R-3c$  symmetry, though significant anomalies of the bond lengths are observed. The temperature effect is nonmonotonic and an anomalous thermal expansion of rare-earth cobaltites is a striking feature of their behavior. The linear thermal expansion coefficient of  $\text{LnCoO}_3$  (where  $\text{Ln} = \text{La}, \text{Dy}, \text{Sm}, \text{Pr}, \text{Y}, \text{Gd},$  or  $\text{Nd}$ ) is a nonmonotonic function of temperature and the anomaly is associated with the physical changes in the system [21, 22]. The nonstandard temperature variation in lattice expansion was suggested to be associated with the normal lattice expansion for individual spin state, spin state changes, and metal-insulator transition. The anomaly is connected with the latter two processes. An anomalous expansion takes place due to the increasing population of excited (IS or HS) states of  $\text{Co}^{3+}$  ions over the course of the diamagnetic-paramagnetic transition and an excitation of  $\text{Co}^{3+}$  ions to another paramagnetic state accompanied by an insulator-metal transition is also observed. Interestingly, the anomalous expansion is governed by parameters that are found to vary linearly with the  $\text{Ln}^{3+}$  ionic radius [21].

A significant change in the lengths of the  $\text{Co-O}$  bonds caused by the cooperative orbital ordering was established at a temperature close to 100 K. The Jahn-Teller distortion was taken into account to describe the orbital ordering that needs to decrease the symmetry to a space group  $I2/a$ . Such an ordering is associated with the intermediate-spin state of  $\text{Co}^{3+}$  ions. However, these anomalies were not found by high-resolution neutron diffraction studies [5, 20]. The suppression of the lattice contribution to the thermal conductivity suggests a considerable bond length fluctuation at room temperature [23]. However, unlike  $\text{LaCoO}_3$  no pronounced anomalies in

the Co–O bond lengths were observed for  $\text{NdCoO}_3$  up to  $T = 540$  K [24]. A pronounced distortion of the  $\text{CoO}_6$  octahedra was observed near the insulator–metal transition, suggesting an increase in the concentration of  $\text{Co}^{3+}$  ions in the IS state.

Bearing in mind the above results, it is of great interest to compare the structural evolution versus temperature of the rhombohedral structure of  $\text{LaCoO}_3$  with that of the orthorhombic structure of  $\text{YCoO}_3$ . The neutron powder diffraction (NPD) in high temperatures up to 1000 K for  $\text{YCoO}_3$  revealed that the structure remains orthorhombic in the whole temperature range, space group  $Pbnm$  [25, 26]. The predominant deviation from the ideal cubic symmetry in  $\text{YCoO}_3$  arises from the rotation of the cobalt-centered octahedra [25]. The relation  $b > c/\sqrt{2} > a$  observed for  $\text{YCoO}_3$  is typical for structures of the so-called O type, where the buckling of the octahedral network is the dominant source of the orthorhombic distortion.

There is a clear distinction in the thermal expansion between  $\text{LaCoO}_3$  and  $\text{YCoO}_3$ . The Co–O–Co bond angles in  $\text{YCoO}_3$  decrease with temperature above the onset of the spin transition, contrary to  $\text{LaCoO}_3$ , where the Co–O–Co angles steadily increase with temperature. The different behavior of  $\text{LaCoO}_3$  can be associated with the closeness of its  $R-3c$  structure to the high-temperature cubic phase. The Co–O–Co bond angle of  $\text{YCoO}_3$  is very small ( $\sim 148^\circ$ ) and practically remains stable up to 600 K, followed by a decrease with temperature above the onset of the spin transition. This leads to a slightly larger expansion of the  $\text{CoO}_6$  octahedra compared to the lattice expansion. On the other hand, at room temperature, in  $\text{LaCoO}_3$  the Co–O–Co bond angle is  $\sim 164^\circ$  and permanently increases with temperature, leading to a slightly smaller expansion of the  $\text{CoO}_6$  octahedra with respect to the lattice expansion [20]. Such a different behavior was attributed to a higher symmetry of the  $\text{LaCoO}_3$  structure compared to  $\text{YCoO}_3$  ( $Pbnm$ ) [26].

The charge, orbital, or spin ordering, either commensurate or incommensurate, is an usual phenomenon in transition metal oxides such as cuprates, nickelates or manganites. Interestingly, cobaltites do not exclude to exhibit such fascinating phenomenon. In cobaltites, charge ordering occurs in a phase where electrons are strongly localized and can therefore be understood as a correlated polaron glass with nanoscale patches of commensurate charge order superlattices. However, the long-range coherence leads to frustration by charge neutrality requirement. From high-resolution X-ray synchrotron data on  $\text{LaCoO}_3$ , refined in the space group  $I2/a$  (subgroup of  $R-3c$ ) [16], a significant change in the lengths of the Co–O bonds was detected at 100 K and attributed to orbital ordering caused by cooperative Jahn–Teller distortions. However, such an orbital ordering was not detected by high-resolution neutron diffraction studies [5, 20].

### 1.3 Stoichiometric $\text{Ln}_{1-x}\text{A}_x\text{CoO}_3$ Perovskites ( $\text{A}=\text{Ca}, \text{Sr}, \text{Ba}$ )

The substitution of a divalent cation such as  $\text{Ca}^{2+}$ ,  $\text{Sr}^{2+}$ , or  $\text{Ba}^{2+}$  for  $\text{Ln}^{3+}$  in the  $\text{LnCoO}_3$  perovskites is of great interest since it allows the mixed valence  $\text{Co}^{3+}/\text{Co}^{4+}$  to be generated.

The perovskites  $\text{La}_{1-x}\text{Sr}_x\text{CoO}_3$  ( $0 < x \leq 1$ ) have been the object of numerous investigations, showing remarkable changes in the crystal structure [8, 27–29], associated with a metal–insulator transition, [27] and ferromagnetic behavior [30]. It was shown that the substitution of strontium for lanthanum in  $\text{LaCoO}_3$  reduces progressively the  $R\text{-}3c$  rhombohedral distortion [30–35]. The space group was assigned to rhombohedral  $R\text{-}3c$  in the range  $0 \leq x \leq 0.5$  by most of the authors, though the diffraction pattern in the range  $0 \leq x \leq 0.30$  was analyzed in both the space groups  $R\text{-}3c$  and  $I2/a$  [36]. For  $x > 0.50$ , most of the authors reported the cubic symmetry  $Pm\text{-}3m$ . Nevertheless, it must be emphasized that, for higher Sr contents ( $x > 0.70$ ), the possibility of oxygen deficiency in the cubic lattice should be considered, which is not always taken into consideration unfortunately by several authors. This is the case, at least for  $x \geq 0.8$  as shown in the next section [37]. The limit cubic perovskite  $x = 1$ ,  $\text{SrCoO}_3$  can be synthesized only under high oxygen pressure superior to 15 MP [38, 39] or by soft chemistry method [40].

The detailed analysis of the Co–O bond lengths and Co–O–Co and O–Co–O bond angles of  $\text{La}_{1-x}\text{Sr}_x\text{CoO}_3$  has been carried out by many authors. A decrease in the Co–O distance and increase in the Co–O–Co angle was observed for  $x < 0.30$  [27, 32, 41]. In fact, the rhombohedral distortion is measured by the departure from  $180^\circ$  of the Co–O–Co angle, whereas the deviation of the O–Co–O angle from  $90^\circ$  gives the distortion of  $\text{CoO}_6$  octahedra. For the substitution of  $\text{La}^{3+}$  by larger size  $\text{Sr}^{2+}$  cation, the rhombohedral distortion gradually decreases with the increase in Sr content.

Since the hole concentration ( $\text{Co}^{3+}/\text{Co}^{4+}$  ratio) and the crystal structure have been changed simultaneously in  $\text{La}_{1-x}\text{Sr}_x\text{CoO}_3$ , it is difficult to get the pure effect of the lattice expansion by  $\text{Sr}^{2+}$  substitution. The  $\text{Ln}_{1-x}\text{Sr}_x\text{CoO}_3$  stoichiometric perovskites with  $\text{Ln} \neq \text{La}$  exhibit a smaller homogeneity range when prepared under normal pressure conditions, that is,  $x \leq 0.50$ . The symmetry of the structure may be maintained, that is, orthorhombic  $Pbmn$  (or  $Pnma$ ), as shown for  $\text{Gd}_{0.50}\text{Sr}_{0.5}\text{CoO}_3$  [42, 43] and  $\text{Nd}_{0.5}\text{Sr}_{0.5}\text{CoO}_3$  [44, 45], or monoclinic  $P2_1/m$  as shown for  $\text{Pr}_{0.5}\text{Sr}_{0.5}\text{CoO}_3$  [46] and  $\text{Eu}_{0.5}\text{Sr}_{0.5}\text{CoO}_3$  [44]. In most of the cases, for low doping values, that is,  $x < 1/3$ , the orthorhombic symmetry is maintained. Nevertheless, the Sr substitution introduces a significant distortion of the octahedra and thereby a change in the electric crystal field at the  $\text{Co}^{3+}$  site as shown for  $\text{Nd}_{0.67}\text{Sr}_{0.33}\text{CoO}_3$  at 225 K [47], which exhibits a broad range of Co–O distances from 1.74 to 2.09 Å. This altering trend of the Co–O bond length coincides with the crossover of the lattice parameters from  $a > b$  to  $a < b$ , indicating an anisotropic effect of the substitution on the structure [11, 47].

The study of the perovskites  $\text{La}_{0.7}\text{Ln}_{0.05}\text{Sr}_{0.25}\text{CoO}_3$  [48] doped with 5% of various lanthanides shows that doping with a smaller  $\text{Ln}^{3+}$  cation does not change the rhombohedral structure. However, a linear and isotropic shrinkage of the lattice was observed with decreasing  $\langle r_A \rangle$  according to the sequence  $\text{La}^{3+} > \text{Nd}^{3+} > \text{Gd}^{3+} > \text{Y}^{3+} > \text{Ho}^{3+}$ . Importantly, this shrinkage has no apparent effect on the Co–O bond length while it bends the Co–O–Co bond angle significantly

The  $\text{Ln}_{1-x}\text{Sr}_x\text{CoO}_3$  phases for  $\text{Ln} = \text{Y}^{3+}$  and  $\text{Ho}^{3+}$  for  $0 \leq x \leq 1$  were prepared under high pressures (6 GPa) and temperatures 1450–1650 °C and reported to be

$\sqrt{2a_p} \times \sqrt{2a_p} \times \sqrt{2a_p}$  orthorhombic but no space group or structures were reported [49]. The highly substituted phases,  $x \geq 0.5$  for  $Y^{3+}$  and  $x \geq 0.6$  for  $Ho^{3+}$ , were shown to be cubic, and for  $x = 0.40$  the system was observed to be biphasic (cubic/orthorhombic). Unfortunately, no chemical analysis of the oxygen content of these phases was carried out. The evolution of the crystal structure of  $La_{1-x}Sr_xCoO_3$  versus temperature shows that this phase keeps the  $R-3c$  symmetry for  $4 K < T < 300 K$ , at least up to a level  $x \sim 0.5$  [32, 50]. The Co–O bond length is the largest for  $x = 0.20$ , that is, close to the metal–insulator transition composition. The Co–O bond length shows normal temperature variation. However for,  $x = 0.3$  the Co–O bond length increases dramatically in the paramagnetic phase [32].

For the  $La_{1-x}Ba_xCoO_3$  stoichiometric perovskites, the crystal structure also remains  $R-3c$  for lower substitution levels [51, 52] and becomes cubic ( $Pm\bar{3}m$ ) for higher level [44]. The room-temperature crystal structure of  $La_{0.5}Ba_{0.5}CoO_3$  is cubic  $Pm-3m$  [53]. However, at low temperature the data can be refined, using the  $P4/mmm$  space group with the long-range tetragonal distortion. Nevertheless, there exist two other forms, called ordered  $LaBaCo_2O_6$  and nanoscale ordered  $LaBaCo_2O_6$  [53–55], which will be discussed later in this chapter.

The substitution of  $La^{3+}$  by a smaller cation,  $Ca^{2+}$ , enhances the stabilization of the orthorhombic symmetry. The perovskites  $La_{1-x}Ca_xCoO_3$  show a structural transition from rhombohedral  $R-3c$  to orthorhombic  $Pnma$  for  $x \geq 0.2$  [51, 56–58]. Thus, the structure depends on the size of the A-site cations, which is usual [44, 58–60].

## 1.4

### Oxygen-Deficient Perovskites: Order–Disorder Phenomena in the Distribution of Anionic Vacancies

#### 1.4.1

##### The Perovskites $ACoO_{3-\delta}$ (A-Ca, Sr, Ba)

Starting from the octahedral lattice of the stoichiometric “ $ACoO_3$ ” perovskites, the great ability of cobalt to adopt lower coordinations, such as pyramidal or tetrahedral, explains that the presence of oxygen vacancies will play a major role in the crystal chemistry of  $ACoO_{3-\delta}$  cobaltites. This multiple coordination of cobalt, and the higher stability of  $Co^{3+}$  compared to  $Co^{4+}$ , makes that for  $A = Sr$ , besides the stoichiometric  $SrCoO_3$  perovskite that can be synthesized only under particular conditions (high pressure or electrochemical reaction), there exist oxygen-deficient perovskites  $SrCoO_{3-\delta}$ , which exhibit various distributions of the oxygen vacancies, depending on the  $\delta$ -value. Consequently,  $SrCoO_{3-\delta}$  presents a rich phase diagram with different crystal structures as a function of the oxygen deficiency and also depending on the preparative conditions [61, 62], all belonging to the family of nonstoichiometric perovskites. The cobaltite  $SrCo_2O_5$  ( $\delta = 0.50$ ) was reported to crystallize in the well-known brownmillerite-type structure  $Imma$  with the orthorhombic unit cell  $\sqrt{2a_p} \times 4a_p \times \sqrt{2a_p}$  [61, 63] and was more recently described in the orthorhombic  $Ima2$

space group [64]. Whatever the space group, this structure can be described as an ordered anion-deficient perovskite with one-sixth of the oxygen sites being vacant. Oxygen vacancies are ordered in alternate  $(001)_p$   $\text{CoO}_2$  planes of the cubic structure, so that  $[110]_p$  rows of oxide anions are alternatively missing (Figure 1.2). Thus, the oxygen vacancies are ordered in a layered manner resulting in sheets with tetrahedral  $\text{CoO}_4$  units that alternate with octahedral ones.

Note that this brownmillerite phase, derived from the perovskite, can be prepared in normal conditions of pressure, contrary to  $\text{SrCoO}_3$ , but is still metastable, and can indeed be obtained only by quenching from high temperature into liquid nitrogen. Slow cooling gives rise to the decomposition of the brownmillerite phase into  $\text{Sr}_6\text{Co}_5\text{O}_{15}$  [65] and  $\text{Co}_3\text{O}_4$ . Besides that, above 1073 K, a cubic perovskite-type phase is stabilized. The structural evolution of  $\text{Sr}_2\text{Co}_2\text{O}_5$  brownmillerite-like phase from room temperature to 1475 K has been recently revisited [66].

For intermediate compositions,  $0.5 < \delta < 1$ , a complete disordering of the oxygen vacancies can also be obtained, as observed for the cubic perovskite  $\text{SrCoO}_{2.64}$  [67], which crystallizes in the  $Pm-3m$  space group. These changes from the cubic symmetry for  $\text{SrCoO}_{3-\delta}$  to the orthorhombic symmetry of  $\text{SrCo}_2\text{O}_5$  were studied a long time ago [68]. In fact, the oxygen stoichiometry and vacancy ordering can be modified not only by controlling the temperature and/or the oxygen partial pressure but also by electrochemical oxidation. In this sense, the structural changes occurring during the electrochemical oxidation of  $\text{SrCoO}_{2.50}$  to  $\text{SrCoO}_3$  have been recently investigated and two new ordered phases have been found for  $\text{SrCoO}_{2.87}$  and  $\text{SrCoO}_{2.75}$  [69]. This is exemplified by the tetragonal structure of the oxygen-deficient perovskite  $\text{SrCoO}_{2.87}$  (Figure 1.3) determined in the space group  $I4/mmm$  ( $a \sim 2a_p/\sqrt{2}$  and  $b \sim 2a_p$ ), which consists of rows of  $\text{CoO}_5$  pyramids, alternating with rows of  $\text{CoO}_6$  octahedra and mixed rows of  $\text{CoO}_5/\text{CoO}_6$  polyhedra.

Thus, a wide range of  $\text{SrCoO}_{3-\delta}$  perovskites can be synthesized, where the cobalt valency varies from  $\text{Co}^{4+}$  for the stoichiometric perovskite to  $\text{Co}^{3+}$  for the brownmillerite-type phase  $\text{Sr}_2\text{Co}_2\text{O}_5$ , with all the possibilities of intermediate mixed valence  $\text{Co}^{3+}/\text{Co}^{4+}$ . Moreover, simultaneously the cobalt coordination changes from octahedral to pyramidal and finally to tetrahedral. These compositional and structural changes drastically affect the magnetic and transport properties of these materials. For example,  $\text{SrCoO}_3$  exhibits ferromagnetism with  $T_C$  close to 266 K [70] and metallic electronic conductivity, whereas  $\text{SrCoO}_{2.50}$  is an antiferromagnetic and charge transfer insulator material [71].

Changing the nature of the A cation of the perovskite cage leads to a dramatic modification of the homogeneity range of this structure. For the substitution of Ba for Sr in  $\text{SrCoO}_{2.50}$ , a nonstoichiometric perovskite  $\text{Sr}_{1-x}\text{Ba}_x\text{CoO}_{2.50}$ , with cubic symmetry, was synthesized for  $0.20 \leq x \leq 0.5$ . It was suggested by several authors that the vacancies are distributed randomly through the anionic sublattice of the perovskite structure, though an ordered phases is expected for such a high-vacancy concentration [72, 73]. The room-temperature oxide  $\text{Sr}_{0.8}\text{Ba}_{0.2}\text{CoO}_{2.5}$  adopts the orthorhombic brownmillerite-like structure ( $Ibm2$ ), containing layers of  $\text{CoO}_6$  octahedra alternating with layers of  $\text{CoO}_4$  tetrahedra along the  $b$ -axis [74].

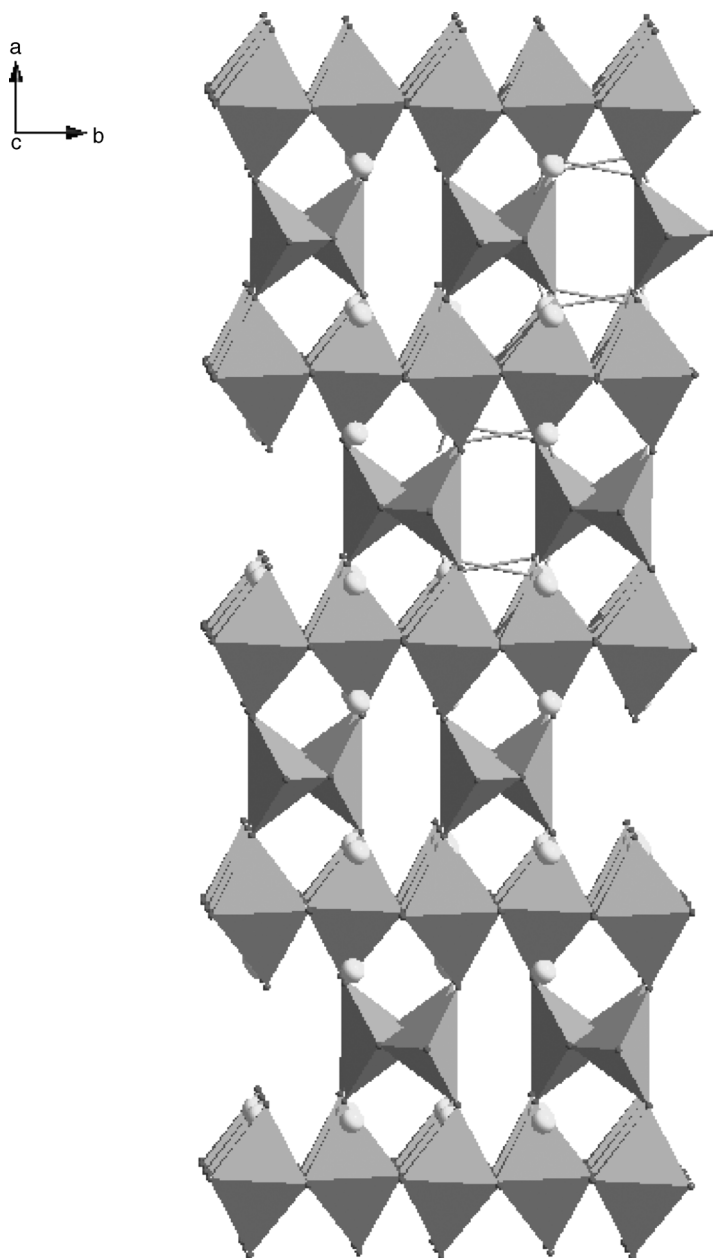


**Figure 1.2** Perspective view of the structure of the brownmillerite-type cobaltite  $\text{Sr}_2\text{Co}_2\text{O}_5$ . Orthorhombic. Adapted from Ref. [64].

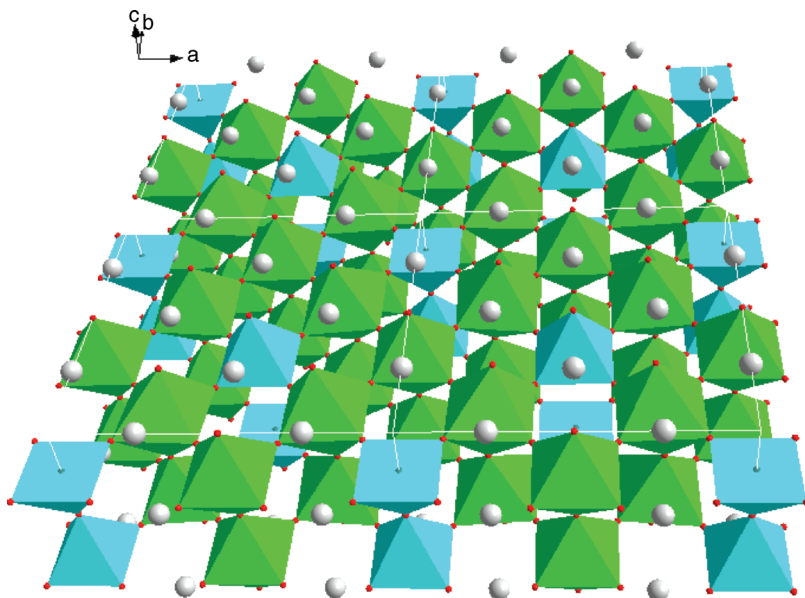


**Figure 1.3** Perspective view of the semioordered structure of  $\text{SrCo}_{2.87}$  forming rows of  $\text{CoO}_5$  pyramids, alternately with rows of corner-sharing  $\text{CoO}_6$  octahedra and with mixed rows of  $\text{CoO}_5/\text{CoO}_6$  polyhedra. Adapted from Ref. [69].

For higher barium contents, the oxygen vacancies in the anionic perovskite sublattice is no more stable, leading to structures related to the perovskite, called “hexagonal perovskites” that will be discussed further in Section 1.6.

The smaller size of the A-site cation induces large structural distortions of the  $\text{CoO}_6$  octahedra and decreases the covalency of the  $\text{Co}-\text{O}$  bond. Consequently, the synthesis of  $\text{CaCoO}_3$  is a challenging task. The  $\text{Sr}_{1-x}\text{Ca}_x\text{CoO}_3$  phase with  $x=0.8$  was synthesized under high pressure and high-temperature condition, but the synthesis of  $\text{CaCoO}_3$  was not successful [75]. However, there are reports on the synthesis of nonstoichiometric compound  $\text{CaCoO}_{3-\delta}$  [76, 77].  $\text{CaCoO}_{2.52}$  crystallizes in the orthorhombic structure with  $a \sim b \sim c \sim 2a_p$  [76]. The coexistence of the brownmillerite phase with the orthorhombic structure has also been reported [77]. However, the substitution of a smaller cation, such as Ca for Sr, does not favor the formation of the brownmillerite structure. The oxygen-deficient perovskite  $\text{Ca}_2\text{Co}_2\text{O}_5$  [78–81] was also synthesized: its orthorhombic structure ( $a \sim b \sim 2a_p\sqrt{2}$ ,  $c \sim 2a_p$ ) has been described as an alternated stacking of layers of  $\text{CoO}_5$  pyramids and  $\text{CoO}_6$  octahedra [79, 80]. The [110] rows of anions and anion vacancies alternate along the  $c$ -direction [79]. The brownmillerite-type ordered oxygen-deficient  $\text{Ca}_2\text{Co}_2\text{O}_5$  perovskite can also be stabilized in the form of thin films due to substrate-induced strains [82]. The latter exhibits a different cell  $\text{\AA}$ ,  $a \sim a_p\sqrt{2}$ ,  $b \sim 4a_p$ , and  $c \sim a_p\sqrt{2}$ , and the space group  $Ibm2$ .

## 1.4.2

**The Sr-Rich Perovskites  $\text{Sr}_{1-x}\text{Ln}_x\text{CoO}_{3-\delta}$** 

In contrast to the Ln-rich perovskite cobaltites, the Sr-rich perovskite cobaltites are characterized by a strong tendency to exhibit a large oxygen deficiency with respect to the stoichiometric “O<sub>3</sub>” content. As a consequence, their magnetic and transport properties are strongly influenced by their oxygen stoichiometry. Thus, the studies on such phases make demands of a systematic determination of their oxygen composition in order to avoid an erroneous interpretation of their physical properties.

The introduction of a lanthanide cation on the strontium site stabilizes the perovskite structure, with a rather large oxygen deficiency [29, 37, 83–88]. The Sr-doped rare-earth perovskite cobaltites,  $\text{Sr}_{1-x}\text{Ln}_x\text{CoO}_{3-\delta}$  with  $0.1 \leq x \leq 0.40$ , show a rich variety of crystal structures depending on the size of the  $\text{Ln}^{3+}$  cations, the substitution level  $x$ , and the amount of oxygen vacancies present. Moreover, the detailed structure and nature of their space group are still a matter of controversy among different authors.

One of the most important structural types of these Sr-rich cobaltites deals with the 224 cobaltites, which were synthesized for  $0.1 \leq x \leq 1/3$  for small lanthanides  $\text{Ln} = \text{Er, Ho, Dy, Gd, Sm, Eu, Tb}$  and for Y [29, 83, 85, 89–92]. These compounds crystallize in a modulated tetragonal structure with the space group  $I4/mmm$  and the cell parameters  $a \sim 2a_p$  and  $c \sim 4a_p$ , where  $a_p$  is the cubic perovskite cell parameter [37, 90]. This structure is closely related to that of brownmillerite: it consists of alternating layers of oxygen full  $\text{CoO}_6$  octahedra and oxygen-deficient  $\text{CoO}_4$  tetrahedral sheets. In contrast to the chains of  $\text{CoO}_4$  tetrahedra running along the [110] direction found for the brownmillerite structure, the tetrahedra segregate to  $\text{Co}_4\text{O}_{12}$  units in 224 cobaltites. Figure 1.4 shows the oxygen-deficient layer for  $\text{Sr}_{0.7}\text{Y}_{0.3}\text{CoO}_{2.62}$  together with the tetrahedral layer in the ordered brownmillerite structure. The figure clearly shows the quite different arrangement of oxygen vacancies in these two structures. The tilting of the octahedra is different in this structure compared to the brownmillerite structure and there exists an additional oxygen atom per layer with  $2a_p \times 2a_p$  dimension. Also, as suggested by the chemical formula  $\text{Sr}_{0.7}\text{Y}_{0.3}\text{CoO}_{2.62}$ , the additional oxygen ions are located in the tetrahedral layers so that some of the cobalt ions adopt a trigonal-bipyramidal coordinations [89].

In fact, the phase diagram of the  $\text{Sr}_{1-x}\text{Ln}_x\text{CoO}_{3-\delta}$  perovskites is rather complex for this Sr-rich region as shown in Figure 1.5 [90].

The formation of the single-phase perovskites  $\text{Sr}_{1-x}\text{Ln}_x\text{CoO}_{3-\delta}$ , with  $\text{Ln} = \text{La–Yb}$ , and Y strongly depends on the ionic radius of the rare-earth species [29, 91]. The strontium-doped rare-earth cobaltites  $\text{Sr}_{1-x}\text{Ln}_x\text{CoO}_{3-\delta}$  show that the range of solid solution becomes smaller with decreasing ionic radii. A substantial solid solution range is observed ( $0.1 < x < 1$ ) for the larger ions,  $\text{La}^{3+}$ ,  $\text{Pr}^{3+}$ ,  $\text{Nd}^{3+}$ , and  $\text{Sm}^{3+}$ , while the range contracts for the smaller rare earths from  $0.05 \leq x \leq 0.60$  for  $\text{Gd}^{3+}$  to  $0.05 \leq x \leq 0.20$  for  $\text{Yb}^{3+}$ .

In this diagram, one also observes that the stability range of the 224 perovskite strongly depends on the  $\text{Ln}^{3+}$  size. It varies from  $0.10 \leq x \leq 0.33$  for the larger size ions  $\text{Ln} = \text{Sm–Ho}$  to Y, to  $0.1 \leq x \leq 0.2$  for Er and Tm, and  $x \approx 0.1$  for Yb [29].

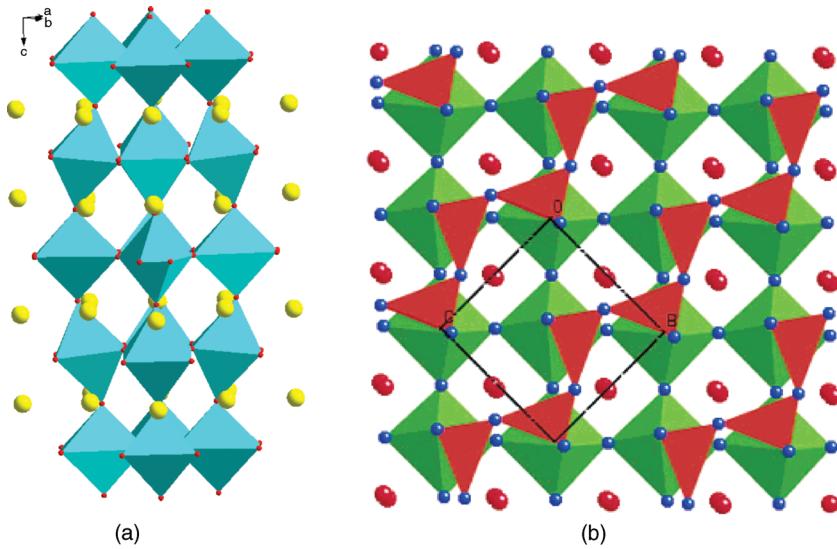


**Figure 1.4** The structure of (a) tetragonal  $\text{Sr}_{0.7}\text{Y}_{0.3}\text{CoO}_{2.62}$  and (b) brownmillerite  $\text{SrCoO}_{2.5}$ . Adapted from Ref. [89].

A different homogeneity range was observed for the 224 phases: nonexistence of the Sm phase,  $0.3 \leq x \leq 0.5$  for Gd,  $0.3 \leq x \leq 0.4$  for Eu and Tb, and  $x \approx 0.3$  for Y and Ho [85]. The 224 superstructure can be obtained also for the La phase for an oxygen content close to 2.75, which poses the question on the A-site ordering [86]. It was

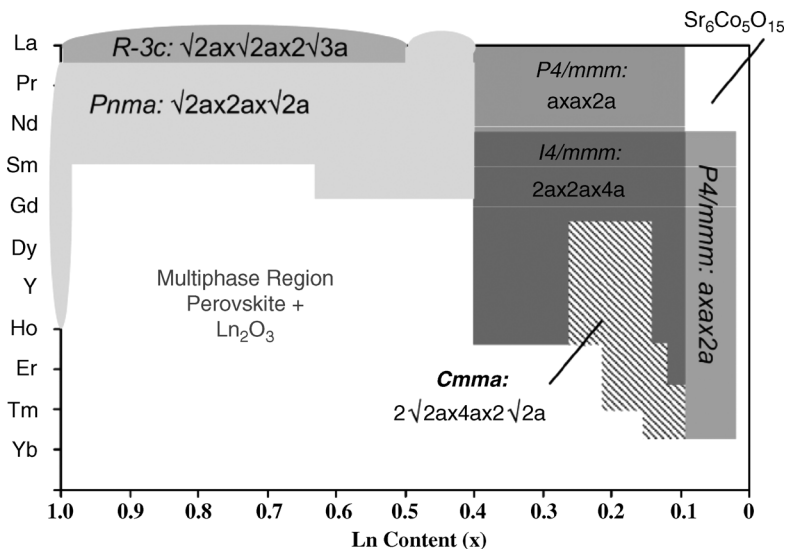


**Figure 1.5** The perovskite phase diagram for  $\text{Sr}_{1-x}\text{Ln}_x\text{CoO}_{3-\delta}$  as a function of rare-earth ionic radii and Sr-doping level. The new orthorhombic family is shown by the black- and white-shaded region. Adapted from Ref. [90].

claimed that in  $\text{La}_{0.33}\text{Sr}_{0.67}\text{CoO}_{2.72}$ , the oxygen vacancy ordering alone is the main reason for the occurrence of this complex superstructure.

Besides the 224 cobaltites with the  $I4/mmm$  symmetry, two other types of oxygen-deficient perovskites with different symmetries were observed. The first type concerns the perovskites involving the tetragonal symmetry  $P4/mmm$  with  $a_p \times a_p \times 2a_p$  cell parameters. The homogeneity range of the latter depends on the size of the rare-earth cation: it is limited to a very small Ln content,  $x \sim 0.05\text{--}0.10$ , for smaller rare-earth cations (Yb–Sm) [90, 91] (Figure 1.5), whereas it covers a broader Ln content,  $0.1 \leq x \leq 0.4$ , for larger rare-earth cations (Nd–La) [90, 93] (Figure 1.5). The second type exhibits an orthorhombic symmetry, corresponding to the space group  $Cmma$  (or equivalent  $Cmcm$ ), with the  $2a_p\sqrt{2} \times 4a_p \times 2a_p\sqrt{2}$  cell parameters and is obtained for Ln = Yb Tm, Er, Ho, Y, and Dy, whose homogeneity range depends on the size of these cations, that is, comprised between 0.1 and 0.28 (Figure 1.5) [90].

In fact, the space group of these perovskites is directly correlated with the distribution of the oxygen vacancies in the structure, inducing various distortions of the polyhedra, and various bucklings of the latter. In the  $I4/mmm$  224 structures, the oxygen vacancies are located at the apical sites of the octahedra, whereas they are located in the basal plane of the octahedra at the equatorial sites in the  $P4/mmm$  structure and in the orthorhombic  $Imma$  brownmillerite structure [94].

It is most probable that these oxides that are characterized by a short-range ordering of the anionic vacancies also exhibit short-range charge ordering of the  $\text{Co}^{3+}/\text{Co}^{4+}$  species as proposed for  $\text{Ho}_{0.1}\text{Sr}_{0.9}\text{CoO}_{3-\delta}$  with  $\delta = 0.2$  [94, 95]. It has also been suggested that the A-site ordering could be responsible for the stabilization of the 224 structure of these oxides [29, 85].

Importantly, the large oxygen deficiency in these cobaltites influences dramatically the cobalt valency, that is, the  $\text{Co}^{3+}/\text{Co}^{4+}$  ratio may vary considerably and has a profound effect on the magnetic and transport properties of these compounds. This effect is amplified also by the possibility of charge ordering that may exist and may induce a physical transition as the temperature varies. Another effect deals with the possibility of charge disproportionation that may appear for  $\text{Co}^{3+}$  into  $\text{Co}^{2+}$  and  $\text{Co}^{4+}$  according to the equation  $2\text{Co}^{3+} \rightleftharpoons \text{Co}^{2+} + \text{Co}^{4+}$ . Thus, the mixed valence of cobalt,  $\text{Co}^{3+}/\text{Co}^{4+}$ , and the oxygen stoichiometry must be determined with accuracy in these oxides, before any physical study, which is not unfortunately the case for many authors. This was shown for Sr-rich cobaltites  $\text{Ln}_{0.1}\text{Sr}_{0.9}\text{CoO}_{3-\delta}$  and  $\text{Ln}_{0.2}\text{Sr}_{0.8}\text{CoO}_{3-\delta}$  [37], where  $\delta$  can vary from 0.10 to 0.40. It was indeed observed that in these oxides,  $\delta$  decreases as the size of the  $\text{Ln}^{3+}$  cation increases for all the series of perovskites prepared in the same conditions in air [37], that is, for the whole series the cobalt valence ( $V_{\text{Co}}$ ) decreases with the size of the lanthanide (Figure 1.6). It will be shown in Chapter 2 that this oxygen nonstoichiometry has a dramatic impact upon the magnetic properties of this material.

The electron energy loss spectroscopy (EELS) can also be used to determine the average cobalt valence with reference to the spectra of a standard specimen with known cation valence states [96, 97]. The EELS analysis shows indeed that the cobalt valence in the oxygen-deficient cobaltite  $\text{La}_{0.5}\text{Sr}_{0.5}\text{CoO}_{2.25}$  is +2 [98].

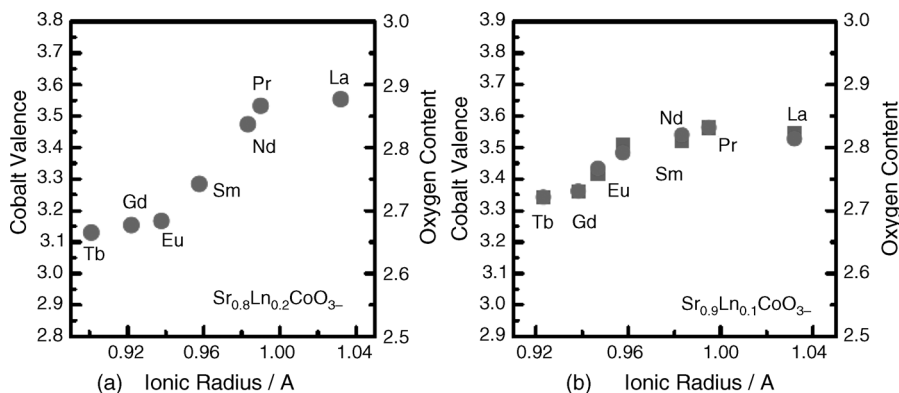


**Figure 1.6** Evolution of the oxygen content (right  $y$ -axis) or cobalt oxidation state (left  $y$ -axis) versus ionic radius for (a)  $\text{Sr}_{0.8}\text{Ln}_{0.2}\text{CoO}_{3-\delta}$  and (b)  $\text{Sr}_{0.9}\text{Ln}_{0.1}\text{CoO}_{3-\delta}$ . Adapted from Ref. [37].

### 1.4.3

#### The Ordered Oxygen-Deficient 112 Perovskites $\text{LnBaCo}_2\text{O}_{5+\delta}$ and $\text{LnBaCo}_2\text{O}_{5.5+\delta}$

When the size difference between  $\text{Ln}^{3+}$  and  $\text{A}^{2+}$  cations becomes large in  $\text{Ln}_{1-x}\text{A}_x\text{CoO}_{3-\delta}$  perovskites, one observes a tendency of these two cations to order in the form of alternate layers, inducing simultaneously an ordering of the oxygen vacancies in the structure. This is the case for a series of cobaltites with  $\text{A} = \text{Ba}$  and  $\text{Ln} = \text{Ho}, \text{Dy}, \text{Tb}, \text{Gd}, \text{Nd}, \text{Pr}, \text{La},$  and  $\text{Y}$  for  $x = 0.50$ .

The first series of 112 cobaltites corresponds to the formula  $\text{LnBaCo}_2\text{O}_5$  and requires particular conditions of synthesis due to their high rate of anionic vacancies with respect to the stoichiometric perovskite. In fact, the 112 “ $\text{O}_5$ ” oxides were first stabilized by the presence of copper leading to the formulation  $\text{LnBaCo}_{2-x}\text{Cu}_x\text{O}_5$  [99], then the oxides  $\text{LnBaCo}_2\text{O}_5$  were synthesized for  $\text{Ln} = \text{Pr}, \text{Nd}, \text{Sm}, \text{Eu}, \text{Tb}, \text{Dy},$  and  $\text{Ho}$ , by using various oxygen pressures during synthesis, and various argon/hydrogen annealings at lower temperature [100–104]. These cobaltites exhibit either the tetragonal  $P4/mmm$  or the orthorhombic (pseudotetragonal)  $Pmmm$  or  $Pmma$  symmetry, with  $a_p \times a_p \times 2a_p$  cell parameters. They are, in fact, isotypic with the quasi-two-dimensional oxides  $\text{YBaFeCuO}_5$  [105] and  $\text{LaBaMn}_2\text{O}_5$  [106]. This structure (Figure 1.7a) consists of double layers of corner-sharing  $\text{CoO}_5$  pyramids interleaved with  $\text{Ln}^{3+}$  cations, the  $\text{Ba}^{2+}$  cations being located within the pyramidal layers, in the perovskite cages formed by the latter. In fact, this  $[\text{Co}_2\text{O}_5]_\infty$  framework derives from the  $[\text{Co}_2\text{O}_6]_\infty$  framework of the stoichiometric perovskite by elimination of one layer of apical oxygen atoms out of two along the  $c$ -direction. This two-dimensional character of the structure is induced by the fact that one  $\text{Ln}^{3+}$  layer alternates with one  $\text{Ba}^{2+}$  layer.

The second series of 112 cobaltites is generally described by the formula  $\text{LnBaCo}_2\text{O}_{5.50}$ . First observed as an  $a_p \times 2a_p \times 2a_p$  superstructure of the perovskite [100, 107], it was later confirmed and refined either in the space group  $Pmmm$  or in the space group  $Pmma$  by many authors [108–119]. The structure of these oxides (Figure 1.7b) is directly derived from the 112  $\text{LnBaCo}_2\text{O}_5$  structure by

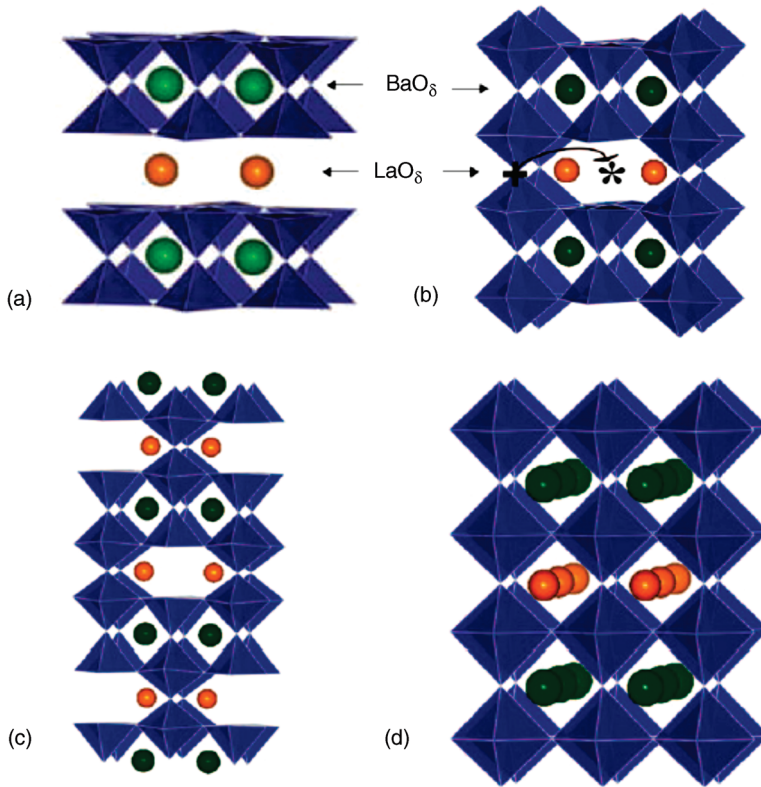


**Figure 1.7** Perspective view of the 112 structures of (a) LnBaCo<sub>2</sub>O<sub>5</sub> cobaltite made of corner-shared CoO<sub>5</sub> pyramids interleaved with Ln<sup>3+</sup> cations, (b) LnBaCo<sub>2</sub>O<sub>5.5</sub> cobaltite made of (010) layers of CoO<sub>6</sub> octahedra interconnected with rows of CoO<sub>5</sub> pyramids. In both structures,

Ln<sup>3+</sup> layers alternate with Ba<sup>2+</sup> layers along  $\bar{c}$ . (c) LnBaMn<sub>2</sub>O<sub>5.5</sub>-type structure, observed as small domains in LaBaCoO<sub>5.50</sub> matrix (~9% of the structure). (d) LaBaCo<sub>2</sub>O<sub>6</sub> ordered layered perovskite where layers of La<sup>3+</sup> and Ba<sup>2+</sup> cations alternate along  $\bar{c}$ .

inserting oxygen atoms at the level of the Ln<sup>3+</sup> layers, between the basal planes of the pyramids in an ordered way, that is, in the anionic vacancies that form the perovskite framework. One [010] row of vacancies of the LnBaCo<sub>2</sub>O<sub>5</sub> structure out of two is filled with oxygen in those layers (Figure 1.7a), leading to the formation of (010) layers of octahedra in the LnBaCo<sub>2</sub>O<sub>5.5</sub> structure. The latter are interconnected through rows of CoO<sub>5</sub> pyramids (Figure 1.7b).

Thus, the crystal structure of the oxides LnBaCo<sub>2</sub>O<sub>5.5</sub> can be described as an ordered sequence of [CoO<sub>2</sub>]-[BaO]-[CoO<sub>2</sub>]-[LnO<sub>δ</sub>] layers stacked along the  $c$ -axis (Figure 1.7b). These ordered oxygen-deficient perovskites are characterized by a 1 : 1 ordering of the Ba<sup>2+</sup> and Ln<sup>3+</sup> cations in the form of alternating planes. As a consequence, the ideal crystallographic description consists of layers of CoO<sub>6</sub> octahedra along the ( $a,c$ ) planes. These layers are interconnected by two-leg ladders along the  $a$ -direction of the rows of CoO<sub>5</sub> pyramids. In between these ladders, the six-sided tunnels are occupied by Ln<sup>3+</sup>

cation. Such a structure is very flexible, that is, sensitive to tiny variations in the oxygen content and to the size of the  $\text{Ln}^{3+}$  cation, so that long-range ordered superstructure or even local distortions can be obtained, leading to dramatic variations in the magnetic properties from one sample to the other [101, 120–122].

In fact, these materials are very sensitive to the method of synthesis (oxygen pressure, temperature, etc.), leading to a more general formula  $\text{LnBaCo}_2\text{O}_{5.50\pm\delta}$ . This nonstoichiometric system  $\text{LnBaCo}_2\text{O}_{5.50\pm\delta}$  is more complex. Due to oxygen vacancy ordering, superstructures can arise, which vary with oxygen content. In addition, the oxygen content does also depend on the size of the  $\text{Ln}^{3+}$  cations [100, 123]. The systematic synthesis in air of the samples  $\text{LnBaCo}_2\text{O}_{5.50\pm\delta}$  ( $\text{Ln} = \text{Pr, Nd, Sm, Eu, Gd, Tb, Dy, and Ho}$ ) samples shows that their oxygen content decreases as the size of the lanthanide decreases, with  $\text{Ln} = \text{Eu, Gd}$  being closest to  $\delta = 0$  [100]. The structural degree of freedom of this family of compounds provides a strong playground to explore the interrelation between electronic, magnetic, and structural properties. The structural study of the 112 cobaltites,  $\text{LaBaCo}_2\text{O}_{5.50}$  [124], shows such a complex oxygen nonstoichiometry phenomenon. The orthorhombic matrix of this phase exhibits the classical 112 cobaltite structure described above (Figure 1.7b), but the NPD data and the electron microscopy investigations reveal that  $\sim 9\%$  of the apical oxygen site of  $\text{CoO}_6$  octahedra (denoted by an asterisk in Figure 1.7b) is vacant, whereas  $\sim 9\%$  of the neighboring site labeled + on (Figure 1.7b) is occupied by oxygen. In fact, the structure consists of domains of  $\text{LaBaMn}_2\text{O}_{5.5}$ -type structure [125] embedded in the matrix of  $\text{LaBaCo}_2\text{O}_{5.5}$  type. This imbrication of the two structure types is easily understood by considering their very close relationships. The  $\text{LaBaMn}_2\text{O}_{5.50}$ -type structure (Figure 1.7c) exhibits similar to the cobaltite  $\text{LaBaCo}_2\text{O}_{5.50}$  (Figure 1.7b) layers of  $\text{La}^{3+}$  and  $\text{Ba}^{2+}$  cations stacked alternately along  $c$ -direction, with the same number of corner-sharing  $\text{CoO}_6$  octahedra and  $\text{CoO}_5$  pyramids, but differs from the latter by the fact that the pure octahedral layers have disappeared. One indeed observes quadruple ribbons of cobalt polyhedra made of double chains of corner-shared  $\text{CoO}_6$  octahedra, sandwiched between two single chains of  $\text{CoO}_5$  pyramids. In summary, this 112-type manganite structure is simply described from the type I cobaltite structure by the shifting of one oxygen atom along  $b$  from the \* to the + position in one  $\text{LaO}_{0.5}$  layer out of two (see arrows in Figure 1.7b). It results in a quadrupling of the periodicity of the structure along  $c$ .

## 1.5

### The Ordered Double Stoichiometric Perovskite $\text{LaBaCo}_2\text{O}_6$

In alkaline earth-rich cobaltites, the possibility to synthesize a stoichiometric perovskite  $\text{A}_{1-x}\text{La}_x\text{CoO}_3$  ( $\delta = 0$ ) increases as the size of the A-site cation increases. It is the case of the stoichiometric perovskite  $\text{La}_{0.5}\text{Ba}_{0.5}\text{CoO}_3$  that can be synthesized easily in air by solid-state reaction from oxides and barium carbonate [53, 126]. In the latter, the  $\text{Ba}^{2+}$  and  $\text{La}^{3+}$  cations are distributed at random and for this reason this cubic phase with the  $Pm\bar{3}m$  symmetry is called disordered perovskite ( $a \sim a_p$ ). The neutron diffraction studies have shown that the crystal structure of  $\text{LaBaCo}_2\text{O}_6$  at

room temperature is the pure cubic perovskite one and the  $\text{La}^{3+}$  and  $\text{Ba}^{2+}$  cations are distributed statistically on the same site [127]. This could be due to the small size difference between the  $\text{La}^{3+}$  and  $\text{Ba}^{2+}$  cations.

Keeping in mind that  $\text{LaBaCo}_2\text{O}_5$  and  $\text{LaBaCo}_2\text{O}_{5.5}$  ordered oxygen-deficient perovskites can be synthesized, the possibility of existence of a stoichiometric ordered perovskite  $\text{LaBaCo}_2\text{O}_6$  with a layered structure has been considered. By using a different method of synthesis, that is, a two-step method, with a preliminary synthesis in reducing conditions followed by annealing in oxygen at lower temperature, the ordered perovskite  $\text{LaBaCo}_2\text{O}_6$  was synthesized [54, 55, 126].

The structure of the latter (Figure 1.7d) derives from the 112 oxygen-deficient perovskite  $\text{LaBaCo}_2\text{O}_{5.50}$ , just by filling the oxygen vacancies, so that one  $[\text{LaO}]_\infty$  layer alternates with one  $[\text{BaO}]_\infty$  layer along the  $c$ -axis of the tetragonal cell ( $a \sim a_p, c \sim 2a_p$ ) with the  $P4/mmm$  space group.

Then, the third form of this perovskite was discovered [54, 55], called nanoscale ordered perovskite, whose symmetry is apparently cubic ( $a \sim a_p$ , space groups  $Pm\bar{3}m$ ). However, its electron diffraction patterns and high-resolution studies show that it consists of  $90^\circ$ -oriented 112-type domains fitted into each other, as shown from the HREM image in Figure 1.8. Such a nanoscale ordered perovskite should not be confused with microdomains of the 112 ordered  $\text{LaBaCo}_2\text{O}_6$  in the cubic  $\text{La}_{0.5}\text{Ba}_{0.5}\text{CoO}_3$  matrix: it develops indeed large strains in the material that modify the crystallographic parameters, inducing atomic-scale lattice distortions.

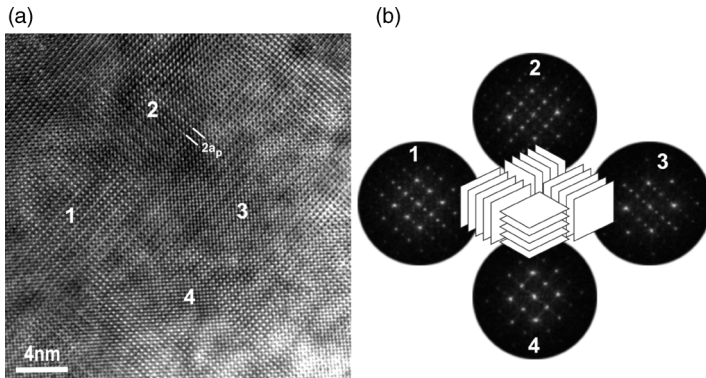


**Figure 1.8** (a)  $\langle 100 \rangle_p^*$  HREM image showing the  $90^\circ$ -oriented domain texture of the nanoscale ordered  $\text{LaBaCo}_2\text{O}_6$ . (b) The Fourier transforms illustrate how the three orientation

variants of 112-type domains can combine to form a 2D domain texture having  $\{100\}_p$  planes as boundary planes. The domain size is typically in the range 5–10 nm. Adapted from Ref. [54].

## 1.6 Hexagonal Perovskite and Derivatives

For a larger size of the A-site cation, the  $\text{ACoO}_{3-\delta}$  cobaltites do not exhibit a square or “pseudo-square lattice,” but form a series of compounds related to the perovskite and

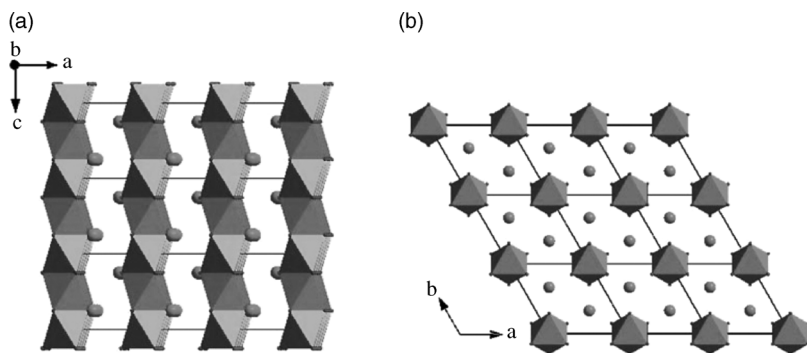


**Figure 1.9** The 2H structure of  $\text{BaCoO}_3$  polymorph and of  $\text{Sr}_{1-x}\text{Ba}_x\text{CoO}_{3-\delta}$  cobaltites: (a) perspective view of the  $[\text{CoO}_3]_\infty$  chains of  $\text{CoO}_6$  octahedra running along the  $c$ -direction of

the hexagonal cell ( $a \sim 5.6 \text{ \AA}$ ;  $c \sim 4.7 \text{ \AA}$ ); (b) triangular arrangement of the chains viewed along  $c$ . Spheres are the  $\text{Ba}^{2+}$  cation. Adapted from Ref. [133].

generally called “hexagonal perovskites.” This is the case of the  $\text{BaCoO}_{3-\delta}$  cobaltites for which three polytypes are actually known, namely, 2H, 5H, and 12H.

The 2H family has been synthesized for the stoichiometric oxide  $\text{BaCoO}_3$  [128–131] and for the mixed Sr-Ba nonstoichiometric cobaltites  $\text{Ba}_{1-x}\text{Sr}_x\text{CoO}_{3-\delta}$  with  $0 \leq x \leq 0.80$  [131, 132]. These compounds, which exhibit a hexagonal cell with a  $\sim 5.6 \text{ \AA}$  and  $c \sim 4.7 \text{ \AA}$ , crystallize in the  $P6_3/mmc$  space group or more rarely in the  $P6m2$  space group. Their structure (Figure 1.9) can be described as unidimensional, that is, it consists of infinite  $[\text{CoO}_3]_\infty$  chains of face-sharing  $\text{CoO}_6$  octahedra (Figure 1.9a). These octahedral chains are displayed in a triangular lattice (Figure 1.9b), where they are interconnected through  $\text{Ba}^{2+}$  cations (Figure 1.9b).

The 5H structure was observed for the cobaltites  $\text{BaCoO}_{2.74}$  [134] and  $\text{BaCoO}_{2.80}$  [135] and was also obtained for  $\text{BaCo}_{0.82}\text{Mn}_{0.18}\text{O}_{2.80}$  [136]. These compounds crystallize in the  $P3m1$  symmetry with cell parameters:  $a \sim 5.7 \text{ \AA}$  and  $c \sim 11.8 \text{ \AA}$ . Their structure (Figure 1.10) consists of trimeric units of face-sharing  $\text{CoO}_6$  octahedra, sharing six apices with single  $\text{CoO}_6$  octahedra (Figure 1.10a). In other words, two types of layers can be distinguished: triple octahedral layers of trimeric units (labeled A on Figure 1.10a) and double layers of corner-sharing octahedra (labeled B on Figure 1.10a). The projection of this structure along  $c$  (Figure 1.10b) shows that the hexagonal windows formed by the trimetric units are obstructed by the single  $\text{CoO}_6$  octahedra (labeled B).

The 12H cobaltites have been synthesized for  $\text{BaCoO}_{2.60}$  [137] and  $\text{BaCo}_{0.58}\text{Mn}_{0.42}\text{O}_{2.83}$  [138]. This structure was also obtained for  $\text{Ba}_{0.9}\text{CoO}_{2.60}$  [139]. This structural type crystallizes in the space group  $P6_3/mmc$ , with  $a \sim 5.6 \text{ \AA}$  and  $c \sim 28.4 \text{ \AA}$ . This structure (Figure 1.11) consists of tetrameric units of face-sharing octahedra running along  $c$ , forming layers (labeled A in Figure 1.11a) bordered by  $\text{CoO}_4$  tetrahedra. Between these layers  $\text{Ba}^{2+}$  cations are interleaved, which ensure the cohesion of the structure. The (001) projection of the structure (Figure 1.11b) shows the relationships with the 5H structure (Figure 1.10b): the  $\text{CoO}_4$  tetrahedra

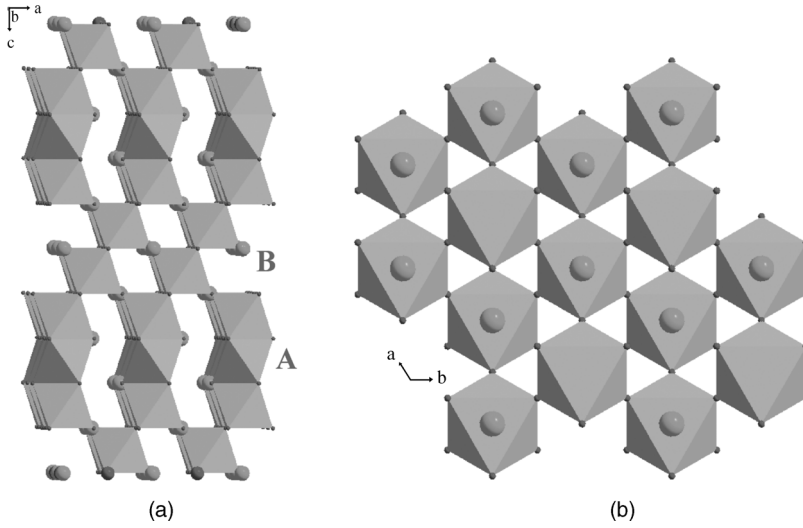


**Figure 1.10** The 5H structure of BaCoO<sub>2.74</sub>: (a) perspective view of the structure along  $\langle 110 \rangle$  showing the trimeric octahedral units of face-sharing octahedra running along  $\bar{c}$  (labeled A), interconnected through double layers of corner-sharing octahedra (labeled B). (b) Projection of the structure along  $\bar{c}$  showing hexagonal windows obstructed by CoO<sub>6</sub> octahedra. Adapted from Ref. [134].

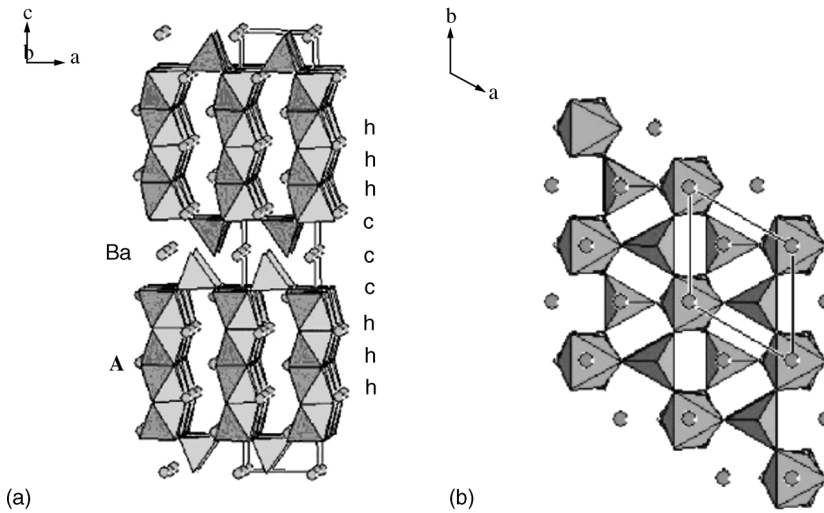


**Figure 1.11** The 12H structure of BaCoO<sub>2.60</sub> [137, 139]: (a) perspective view of the structure along  $\langle 110 \rangle$  showing tetrameric octahedral units of face-sharing octahedra, running along  $\bar{c}$ . The layers of octahedra are bordered by tetrahedra (labeled A). (b) Projection of the structure along  $\bar{c}$ , showing the interconnection of octahedral units through CoO<sub>4</sub> tetrahedra. Adapted from Refs [137, 139].

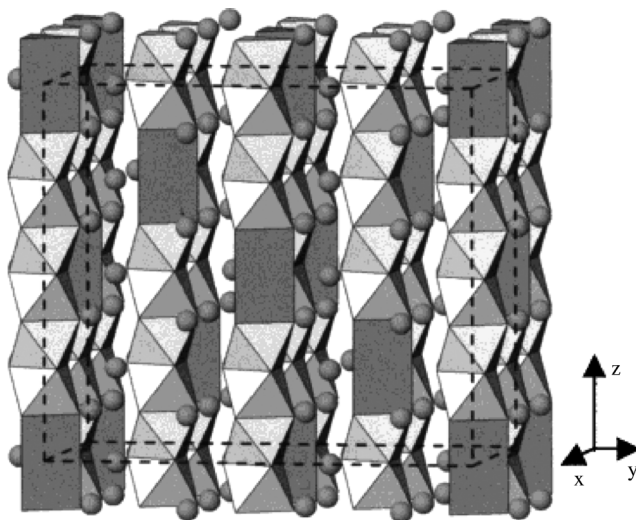


**Figure 1.12** Perspective view of the structure of  $\text{Ba}_8\text{Co}_7\text{O}_{21}$ . Adapted from Ref. [140].

share their corners with the  $\text{CoO}_6$  octahedra of the tetrametric units, ensuring their cohesion, together with the  $\text{Ba}^{2+}$  cations located between those units.

Barium-rich cobaltites characterized by a Ba/Co ratio larger than 1 have been synthesized. This is the case of  $\text{Ba}_8\text{Co}_7\text{O}_{21}$  and  $\text{Ba}_{12}\text{Co}_{11}\text{O}_{33}$ , involving the simultaneous presence of  $\text{Co}^{3+}$  and  $\text{Co}^{4+}$ , with a possible charge ordering [140]. The former crystallizes in the orthorhombic  $Fd\bar{2}d$  symmetry with  $a \sim 11.48 \text{ \AA}$ ,  $b \sim 19.89 \text{ \AA}$ ,  $c \sim 17.46 \text{ \AA}$ , and the second one is monoclinic  $C2/c$  with  $a \sim 11.41 \text{ \AA}$ ,  $b \sim 19.76 \text{ \AA}$ ,  $c \sim 27.19 \text{ \AA}$ , and  $\beta \sim 90^\circ$ . These cobaltites exhibit an incommensurate structure closely related to that of the “hexagonal perovskites.” They consist of limited links of several face-sharing octahedra, as exemplified from the structure of  $\text{Ba}_8\text{Co}_7\text{O}_{21}$  (Figure 1.12). One can indeed describe the structure of the latter phase as made of units of six face-sharing octahedra interconnected through  $\text{Ba}^{2+}$  cations.

## 1.7

### The RP-Type Cobaltites: Intergrowths of Perovskite and Rock Salt Layers and Derivatives

Like cuprates, manganites and ferrites, cobaltites exhibit a great ability to form Ruddlesden and Popper (RP) type phases. These oxides of generic formulation  $A_{n+1}\text{Co}_n\text{O}_{3n+1}$  correspond to the intergrowth of  $[\text{ACoO}_3]_\infty$  perovskite layers with rock salt-type AO layers, where  $A = \text{Ln, Sr, Ca, and Ba}$ . Thus, these cobaltites can be formulated  $(\text{AO})[\text{ACoO}_3]_n$ , with  $n$  ranging from  $n = 1$  to  $n = \infty$ , the latter member corresponding to the perovskite already described above. Besides these RP cobaltites, there exist very closely related structures, which correspond to a larger thickness of the rock salt layers and can be formulated  $(\text{AO})_m(\text{ACoO}_3)_n$ . Thus, all the RP members and derivatives exhibit a two-dimensional character of the cobalt–oxygen framework,

which means that the magnetic and transport properties of these oxides are very anisotropic, compared to the 3D perovskite cobaltites.

### 1.7.1

#### Single-Layered RP Phases $\text{Ln}_{2-x}\text{A}_x\text{CoO}_4$ ( $n = 1$ ), with $\text{A} = \text{Ca}, \text{Sr}$

The  $n = 1$  members of the RP series have been extensively studied for the series  $\text{Ln}_{2-x}\text{Sr}_x\text{CoO}_4$ . These cobaltites exhibit a quasi-two-dimensional structure (Figure 1.13) that crystallizes with the  $\text{K}_2\text{NiF}_4$ -type structure ( $a \sim 3.8 \text{ \AA}$ ;  $c \sim 12.4 \text{ \AA}$ ) with the space group  $I4/mmm$ , where the cobalt ions are in a tetragonally distorted octahedral environment, two axial  $\text{Co}^{n+}-\text{O}$  bonds being elongated relative to the four equatorial bonds. The  $\text{Co}-\text{O}-\text{Co}$  angles are of  $180^\circ$  and the  $\text{Ln}/\text{Sr}-\text{O}$  layers are slightly buckled. The  $\text{Ln}^{3+}$  and  $\text{Sr}^{2+}$  ions are in ninefold coordination with four oxygen sites in the equatorial plane, one oxygen site in the apical position, and four oxygen sites directed to the opposite hemisphere (Figure 1.13). With the exception of  $\text{Ln}_{2-x}\text{Sr}_x\text{CoO}_4$  compounds, other rare-earth cobaltites have received relatively little attention.

The end member  $\text{Sr}_2\text{CoO}_4$  ( $x = 1$ ), which contains formally  $\text{Co}^{4+}$  was synthesized [141, 142] in the polycrystalline form under high-pressure, high-temperature conditions.

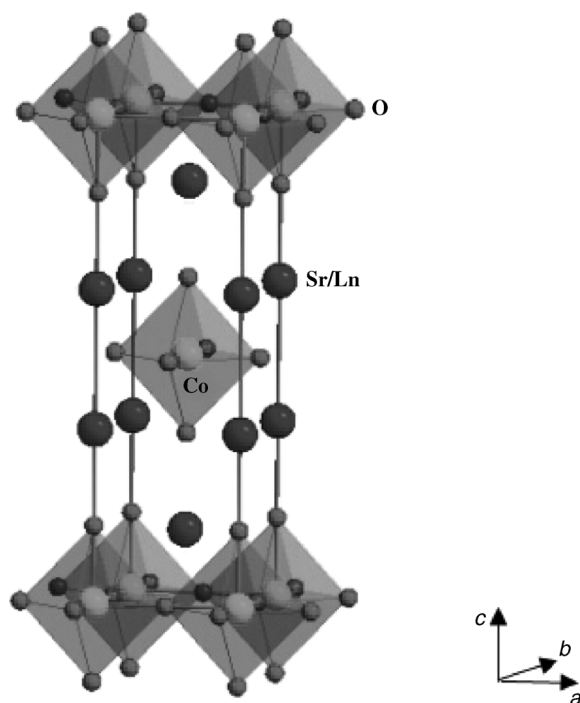


**Figure 1.13** Schematic representation of the  $\text{K}_2\text{NiF}_4$  structure displayed by the  $\text{La}_2\text{CoO}_4$  compounds. Adapted from Ref. [145].

The polycrystalline  $\text{Sr}_2\text{CoO}_4$  was found to be of the  $\text{K}_2\text{NiF}_4$  type with space group  $I4/mmm$ . Nevertheless, the crystal structure of thin films of  $\text{Sr}_2\text{CoO}_4$  exhibits a slight orthorhombic distortion [143].

The other end member obtained for  $\text{Ln} = \text{La}$ ,  $\text{La}_2\text{CoO}_4$  ( $x = 0$ ), with the formal cobalt valence of +2, crystallizes also with the tetragonal symmetry ( $I4/mmm$ ), but at high temperature, and transforms to an orthorhombic form ( $Cmca$ ) below about 410 K [144]. The phase transition is characterized by a tilt of the  $\text{CoO}_6$  octahedra in the low-temperature orthorhombic (LTO) phase [146].

The  $\text{Ln}_{2-x}\text{Sr}_x\text{CoO}_4$  cobaltites have been studied for a wide range of  $x$ -values with different Ln sizes. Most of the data are available in the range  $0 \leq x \leq 1.4$ , compared to the samples with higher  $x$ -values. These cobaltites mainly crystallize in the tetragonal structure with the space group  $I4/mmm$  [147–151].

The range of solid solution in these cobaltites is sensitive to the A-site cation radius. In  $\text{Ln}_{2-x}\text{Sr}_x\text{CoO}_4$ , an upper boundary to the solid solution was found at  $x = 1.4$  for  $\text{Ln} = \text{La}$ ,  $x = 1.3$ , for  $\text{Ln} = \text{Nd}$ , and  $x = 1.2$  for  $\text{Ln} = \text{Gd}$  [148]. It has been observed that the solid solution range converges for the compositions based on smaller rare-earth ions in  $\text{Ln}_{2-x}\text{Sr}_x\text{CoO}_4$ . The lower solid solution limit increases as the ionic radius of the rare-earth ion becomes smaller and a single phase can be formed under atmospheric conditions for  $\text{Dy}_{0.80}\text{Sr}_{1.20}\text{CoO}_{4+\delta}$  [152].

An important characteristic of the  $\text{Ln}_{2-x}\text{Sr}_x\text{CoO}_4$  phases is their ability to exhibit structural transition versus temperature. As also pointed out above for  $\text{La}_2\text{CoO}_4$ , a similar transition to the orthorhombic low-temperature form ( $Cmca$ ) has been observed for  $\text{La}_{1.7}\text{Sr}_{0.3}\text{CoO}_4$  at  $T = 227$  K, from a single-crystal neutron diffraction study [153]. Another first-order phase transition to a new tetragonal phase ( $P4_2/mcm$ ) was observed at 135 K, which was attributed to the spin rotation or flips in the  $\text{CoO}_2$  plane. [146]. In the same way,  $\text{La}_{1.5}\text{Sr}_{0.5}\text{CoO}_4$  that crystallizes in the tetragonal symmetry at room temperature exhibits superstructure peaks in X-ray diffraction at low temperature, which were indexed with the space group  $F4/mmm$  [50]. The role of the size of the  $\text{Ln}^{3+}$  cation upon the structural properties of these cobaltites has been systematically studied for the  $\text{SrLnCoO}_4$  series ( $\text{Ln} = \text{La}, \text{Ce}, \text{Pr}, \text{Nd}, \text{Eu}, \text{Gd}, \text{and Tb}$ ). All these oxides have a tetragonal structure at room temperature with the space group  $I4/mmm$  and exhibit a gradual decrease in their lattice parameters, as the size of the  $\text{Ln}^{3+}$  ion decreases [154]. In a distorted octahedral site, within the perovskite blocks, there are two different Co–O bond lengths: a longer Co–O(1) along the  $c$ -axis and a shorter Co–O(2) in the  $ab$  plane. Both Co–O(1) and Co–O(2) distances monotonically decrease as the size of the rare-earth ion  $r_{\text{Ln}}^{3+}$  gets smaller. The extent of the distortion of the  $\text{CoO}_6$  octahedra can be estimated from the difference ( $\Delta d$ ) between Co–O(1) and Co–O(2) bond lengths. The value of the distortion parameter  $\Delta d$  increases with decreasing A-site rare-earth ionic radius  $r_{\text{Ln}}^{3+}$ . One can also define the distortion of the  $\text{CoO}_6$  octahedron by the ratio of the Co–O(1) bond length  $d_{\text{Co}-\text{O}(1)}$  to  $d_{\text{Co}-\text{O}(2)}$ , the Co–O(2) one [154]. These distortions from the ideal structure appear from the adjustment to the bond length mismatch that exists across the interface between the perovskite blocks and the rock salt (Ln/Sr–O) layers along the  $c$ -axis. This can be estimated by the tolerance factor  $t = (\text{Ln}/\text{Sr}-\text{O})/\sqrt{2}(\text{Co}-\text{O})$ . Note that the tolerance factor in these  $\text{K}_2\text{NiF}_4$ -type Co-based materials lies in the

range  $0.946 < t < 1$ , for which the tetragonal distortion is favored [155]. Again, it is worth noting that the presence and extent of this tetragonal distortion could greatly affect the spin state of the cobalt ions, and even stabilize unusual spin state configurations, such as the intermediate spin state. Such a structural distortion has a strong influence on the magnetic and electrical transport properties of these materials, as it is well known to occur in the corresponding 3D perovskites  $\text{LaCoO}_3$ .

The structural evolution of these oxides versus the Sr content  $x$  has been particularly studied for  $\text{La}_{2-x}\text{Sr}_x\text{CoO}_4$  and  $\text{Pr}_{2-x}\text{Sr}_x\text{CoO}_4$ . For the cobaltites  $\text{La}_{2-x}\text{Sr}_x\text{CoO}_4$ , the evolution of the lattice parameters is very complex [147, 156]. The same trend in the lattice parameters is reported for similar systems though the absolute values differ depending on the synthetic route [148, 157].

In  $\text{La}_{2-x}\text{Sr}_x\text{CoO}_4$ , one observes that the tetragonal distortion,  $d_{\text{Co-O}(1)}/d_{\text{Co-O}(2)}$ , only slightly decreases from 1.08 at  $x=1$  to 1.06 at  $x=1.5$ . This merely gradual decrease in  $d_{\text{Co-O}(1)}/d_{\text{Co-O}(2)}$  implies that the doped holes are mainly accommodated in the  $t_{2g}$  orbital states with less Jahn–Teller distortion, while keeping the IS configuration [156]. The variation in the bond length ratio from  $\text{LaSrCoO}_4$  (1.069) to  $\text{TbSrCoO}_4$  (1.074) indicates that the  $e_g$  states of the IS configuration are not only fully occupied for  $3d_{z^2}$  orbitals but are also partially occupied for  $3d_{x^2-y^2}$  states [154].

### 1.7.2

#### Double-Layered RP Cobaltites: $\text{Sr}_{3-x}\text{Ln}_x\text{Co}_2\text{O}_{7-\delta}$ type

The  $n=2$  members of the RP cobaltites are much more difficult to stabilize. The pure ideal member  $\text{Sr}_3\text{Co}_2\text{O}_7$  has never been synthesized. In contrast, a cobaltite with a closely related structure, which exhibits a large deviation from the oxygen stoichiometry, that is,  $\text{Sr}_3\text{Co}_2\text{O}_{7-x}$ ,  $0.94 < x \leq 1.27$ , was synthesized [158–161]. According to these authors, the samples with  $x \leq 1$  adopt the ideal RP-type tetragonal structure with the classical  $I4/mmm$  space group and the cell parameters  $a \sim 3.8 \text{ \AA}$  and  $c \sim 20 \text{ \AA}$ , whereas for larger  $x$ -values a reduction of the symmetry to orthorhombic  $Immm$  is observed, with  $a \sim 3.8 \text{ \AA}$  and  $b \sim 11.4 \text{ \AA}$ .

In the tetragonal form of  $\text{Sr}_3\text{Co}_2\text{O}_{6.12}$ , the apical oxygen sites of the double perovskite layers located within those layers are at 87% empty (Figure 1.14a). The O(3) site is found to be less occupied and the predominant cobalt geometry will be pyramidal. However, the presence of some octahedra cannot be ruled out. The coordination around cobalt may be tetrahedral if the O(4) site is unoccupied [161]. So, this structure can better be described as derived from that of  $\text{La}_2\text{SrCu}_2\text{O}_6$  [162], that is, it consists of double layers of corner-shared  $\text{CoO}_5$  pyramids intergrown with single rock salt SrO layers (Figure 1.14b), the anionic vacancies between the pyramidal layers being filled at 13% only by oxygen.

In fact, this tetragonal structure, made of double pyramidal cobalt layers intergrown with rock salt layers (Figure 1.14b), has been synthesized for  $\text{Sr}_2\text{Y}_{0.8}\text{Ca}_{0.2}\text{Co}_2\text{O}_6$  [160]. In this  $I4/mmm$  tetragonal cell, with  $a \sim 3.82 \text{ \AA}$  and  $c \sim 19.58 \text{ \AA}$ , an ordering of the  $\text{Sr}^{2+}$  cations and of the  $\text{Y}^{3+}/\text{Ca}^{2+}$  cations takes place in the form of alternate layers stacked along  $c$  (Figure 1.14b). It is this smaller size of  $\text{Y}^{3+}$  and  $\text{Ca}^{2+}$  cations that favors the formation of such double pyramidal cobalt layers [163].

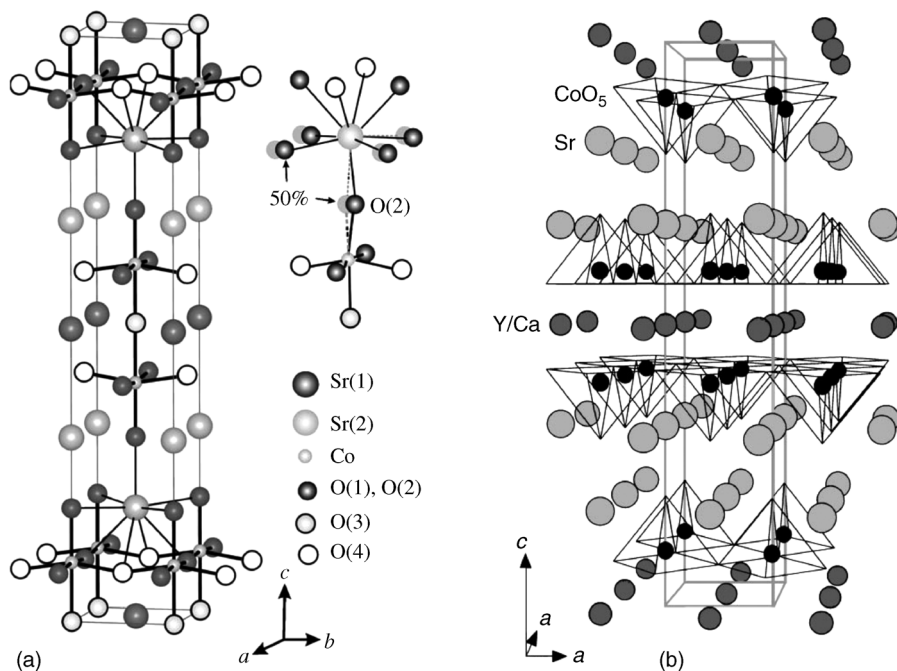


**Figure 1.14** Structure of (a)  $\text{Sr}_3\text{Co}_2\text{O}_{6.12}$  and (b)  $\text{Sr}_2\text{Y}_{0.8}\text{Ca}_{0.2}\text{Co}_2\text{O}_6$  both tetragonal  $I4/mmm$ . The first one is nonstoichiometric and exhibits 87% oxygen vacancies on the apical oxygen sites

of the double layers ( $\square$ ), whereas the second one exhibits double pyramidal cobalt layers, similar to  $\text{La}_2\text{SrCu}_2\text{O}_6$ . Adapted from Ref. [160, 161].

The neutron powder diffraction study of this phase versus temperature reveals that it is orthorhombic at 20 K ( $Immm$ ;  $a \sim b \sim 3.8 \text{ \AA}$ ;  $c \sim 19.5 \text{ \AA}$ ) and becomes tetragonal ( $I4/mmm$ ) on heating above 270 K. This structural transition onset at 270 K is accompanied by a long-range antiferromagnetic ordering [164]. In fact, the above authors observe a rather large homogeneity range for  $\text{Sr}_2\text{Y}_{1-x}\text{Ca}_x\text{Co}_2\text{O}_{6-\delta}$ :  $0.20 \leq x \leq 0.50$  and  $0 \leq \delta \leq 0.24$ , with the same  $I4/mmm$  space group, showing that the cobalt valence ranges from +2.36 to +2.75. Curiously, an  $I4/mmm$  similar structure, with  $a \sim 3.76 \text{ \AA}$  and  $c \sim 20 \text{ \AA}$ , was reported for the composition  $\text{Sr}_2\text{Y}_{0.5}\text{Ca}_{0.5}\text{Co}_2\text{O}_7$  [165], but no detailed chemical analysis about the oxygen stoichiometry of this phase was given.

The stoichiometric “O<sub>7</sub>”  $n = 2$  intergrowth can, in fact, be synthesized by introducing a much larger amount of lanthanide in the structure. This is the case of  $\text{Sm}_2\text{SrCo}_2\text{O}_7$ , which contains only trivalent cobalt and was reported to be tetragonal [166, 167], whereas  $\text{Sm}_2\text{BaCo}_2\text{O}_7$  exhibits an orthorhombic symmetry with  $a \sim b \sim 3.8 \text{ \AA}$  and  $c \sim 19.5 \text{ \AA}$  [163, 166]. The room-temperature structure of  $\text{Gd}_2\text{SrCo}_2\text{O}_7$  is tetragonal and displays small tilts of the oxygen sublattice that are described in the  $P4_2/mnm$  symmetry instead of the idealized  $I4/mmm$  structure. A structural transition at  $T \approx 580 \text{ K}$  is characterized by a reduction of the symmetry and a marked axial elongation of the  $\text{CoO}_6$  octahedra [168].

A small substitution of strontium by cerium favors the stabilization of the oxygen-deficient phase  $\text{Sr}_{2.75}\text{Ce}_{0.25}\text{Co}_2\text{O}_{7-\delta}$ . The main effect of such a substitution on the structure concerns the pseudo-tetragonal symmetry of the unit cell instead of the marked orthorhombic symmetry reported for the oxygen-deficient analogues  $\text{Sr}_3\text{Co}_2\text{O}_{6-\delta}$ . Such a tetragonal  $I4/mmm$  space group was also reported in the  $n=2$  RP phases  $\text{Sr}_2\text{Y}_{1-x}\text{Ca}_x\text{Co}_2\text{O}_6$  [160, 165], for which the  $\text{Y}_{1-x}\text{Ca}_x$  central layer of the perovskite block favors the formation of a double row of tetragonal square pyramids. The electron diffraction patterns of  $\text{Sr}_{2.75}\text{Ce}_{0.25}\text{Co}_2\text{O}_{5.9}$  are consistent with the  $I$ -type symmetry ( $a = 3.8 \text{ \AA}$  and  $c = 20 \text{ \AA}$ ) but they show extra diffuse lines parallel to the  $c^*$ -axis, and the corresponding [100] HREM image shows the presence of diffuse lines that can be ascribed to a disorder between oxygen and vacancy sites at the level of the perovskite block [169].

In these cobaltites, the distribution of oxygen vacancies is a difficult problem, which has led to a lot of controversy among various authors. This is especially the case for the orthorhombic cobaltite  $\text{Sr}_3\text{Co}_2\text{O}_{7-\delta}$  which adopts the  $Immm$  orthorhombic symmetry due to its different ordering of oxygen vacancies, leading to a tripling of the  $b$ -parameter, as soon as  $\delta > 1$ . These subtle changes of oxygen stoichiometry and vacancy ordering may have a profound effect on the physical properties of these cobaltites.

Though the XRD studies do not reveal any oxygen ordering in  $\text{Sr}_3\text{Co}_2\text{O}_{7-\delta}$  for ( $1.09 \leq \delta \leq 1.62$ ), such a behavior was observed in electron diffraction studies [161]. A superstructure due to oxygen ordering was also observed from NPD data [159]. The samples with  $\delta > 1$  adopt the orthorhombic structure with ordered oxygen vacancies along one axis in the  $\text{CoO}_2$  plane. However, for  $\delta > 1$  the oxygen vacancies are found in both the in-plane site and the apical linking site, whereas for  $\delta < 1$  the oxygen vacancies were found only in the linking site. The crystal structure is a simple mixture of  $\text{Co}^{3+}$  square pyramids and  $\text{Co}^{4+}$  octahedra [170].  $\text{Sr}_3\text{Co}_2\text{O}_{7-\delta}$  ( $0.94 \leq \delta \leq 1.22$ ) undergoes a reduction in symmetry from  $I4/mmm$  for  $\text{Sr}_3\text{Co}_2\text{O}_{6.06}$  to  $Immm$  for an oxygen content of 5.94 per formula unit. Thus, the orthorhombic unit cell arises due to the ordering of the oxygen vacancies that leads to a tripling of the  $b$ -parameter. In both cases, the square-pyramidal coordination is observed for the  $\text{Co}^{3+}$  species, with the vacancies located in the apical positions of the perovskite blocks [163]. Figure 1.15 gives an example of the orthorhombic  $Immm$  structure of  $\text{Sr}_3\text{Co}_2\text{O}_{5.78}$  [159]. It can be described as ribbons made of three polyhedral units, one octahedron being sandwiched between two pyramids, forming oxygen-deficient ordered perovskite slabs parallel to (001) and intergrown with rock salt SrO layers.

Figure 1.16 illustrates the oxygen vacancy distribution of  $\text{Sr}_3\text{Co}_2\text{O}_{5.64}$  and  $\text{Sr}_{2.75}\text{Ce}_{0.25}\text{Co}_2\text{O}_{5.9}$ . The structure of  $\text{Sr}_{2.75}\text{Ce}_{0.25}\text{Co}_2\text{O}_{5.9}$  is tetragonal with the space group  $I4/mmm$  in contrast to the marked orthorhombic symmetry of the oxygen-deficient  $\text{Sr}_3\text{Co}_2\text{O}_{5.64}$ . In the orthorhombic  $\text{Sr}_3\text{Co}_2\text{O}_{5.64}$ , the oxygen vacancies order along one axis in the  $\text{CoO}_2$  plane [159]. For the substitution of cerium for strontium, oxygen vacancies also tend to be located in the double perovskite block but on two distinct sites: at the level of the square  $\text{CoO}_2$  planes (O(1) site here, Figure 1.16b) and at the level of the common apical oxygen O(3) site of the two perovskite blocks. Such a distinct distribution of the oxygen vacancies in these doped and undoped

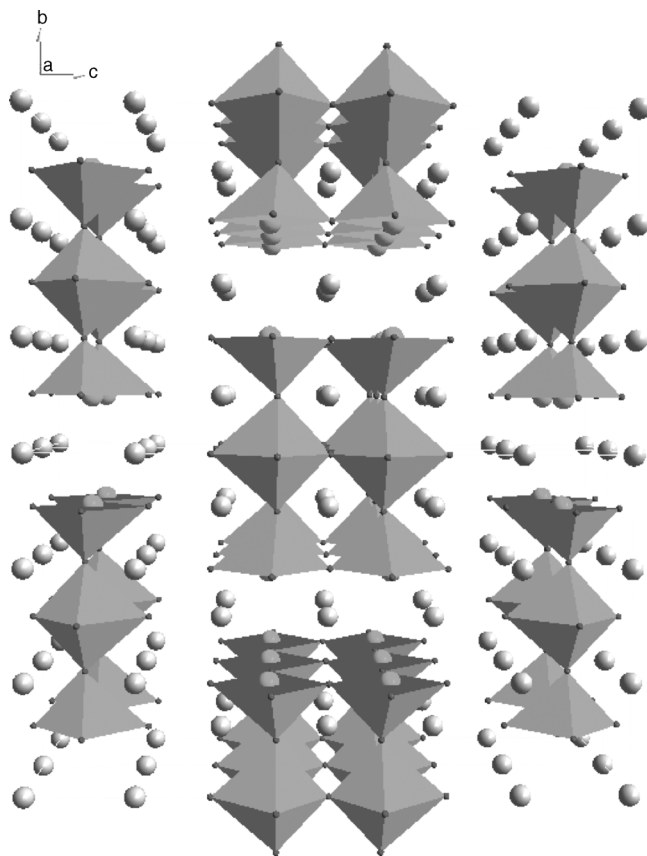


**Figure 1.15** Perspective view of the orthorhombic structure of  $\text{Sr}_3\text{Co}_2\text{O}_{5.82}$ . Adapted from Ref. [159].

oxygen-deficient systems highlights the role played by the cerium cation in stabilizing a different symmetry linked to a different distribution of the oxygen vacancies. In the almost fully oxygenated cerium-doped samples,  $\sim 6\%$  vacancy resides in the cobalt plane.

Finally, the  $n=2$  RP phase can be stabilized by substituting partly titanium or niobium for cobalt, leading to hydrated oxohydroxides. This is the case of the compounds  $\text{Sr}_3\text{Co}_{1.7}\text{Ti}_{0.3}\text{O}_5(\text{OH})_2 \cdot x\text{H}_2\text{O}$  and  $(\text{Sr}_{3-\delta}\text{Co}_{1.9}\text{Nb}_{0.1}\text{O}_{4.86-\delta}(\text{OH})_{3.04} \cdot 0.4\text{H}_2\text{O})$  of the RP phase that were reported to have different magnetic properties from the pure cobaltites, leading, for instance, to cluster and spin glass behavior [171–173]. The most common oxidized form of  $\text{Sr}_3\text{CoO}_{7-\delta}$  ( $\delta \sim 1$ ) is very sensitive to moisture that originates from the unstable  $\text{CoO}_x$  polyhedra, throwing challenge to stabilize more oxidized phases such as  $\delta \ll 1$ . Samples with oxygen content larger than “ $\text{O}_6$ ” have been observed to react quickly with air to form an oxyhydroxide  $\text{Sr}_3\text{Co}_2\text{O}_5(\text{OH})_2 \cdot \gamma\text{H}_2\text{O}$  [171]. The niobium-doped sample crystallizes in the tetragonal  $I4/mmm$  space group, whereas  $\text{Sr}_3\text{Co}_{1.7}\text{Ti}_{0.3}\text{O}_5(\text{OH})_2 \cdot x\text{H}_2\text{O}$  crystallizes in the monoclinic space group  $I12/m1$ . However, the anhydrous form

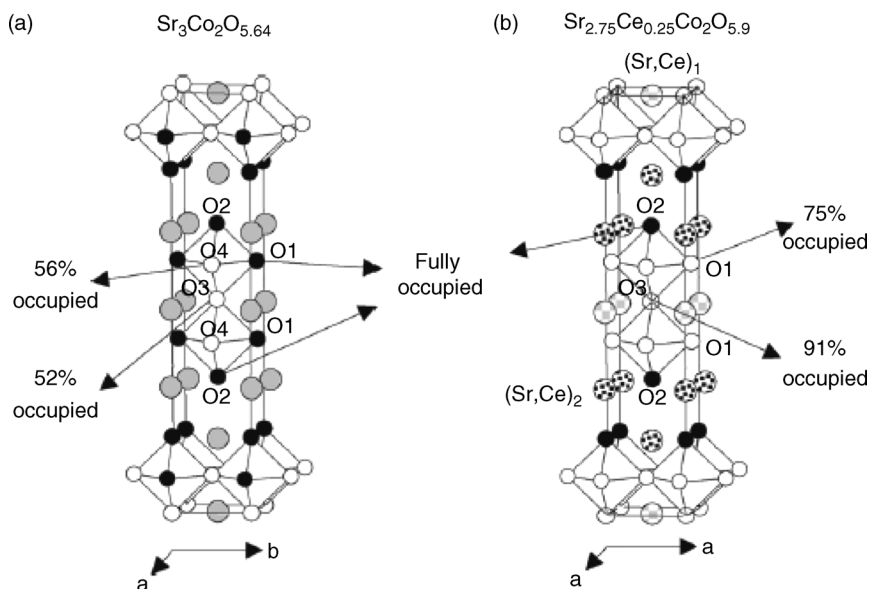


**Figure 1.16** Structural model of oxygen-deficient  $n = 2$  RP phase (a)  $\text{Sr}_3\text{Co}_2\text{O}_{5.64}$  (Ref. [170]) and (b)  $\text{Sr}_{2.75}\text{Ce}_{0.25}\text{Co}_2\text{O}_{5.9}$  phases. Oxygen sites are labeled with black filled and checkerboard circles depending on full and partial filling, respectively. Adapted from Ref. [169].

$\text{Sr}_3\text{Co}_{1.7}\text{Ti}_{0.3}\text{O}_5(\text{OH})_2$ , which is obtained by warming the hydrated oxyhydroxides, crystallizes with a tetragonal unit cell ( $P4/mmm$  space group).

### 1.7.3

#### RP Derivatives with Double and Triple Rock Salt Layers

“TiO” or “BiO” layers can be introduced into the rock salt layers of the RP structures, forming double or triple rock salt-type layers instead of single rock salt layers, similar to high  $T_c$  superconducting cuprates [174]. This is the case of the 1201 cobaltites  $\text{TlSr}_2\text{CoO}_5$  [175],  $\text{Sr}_{2.6}\text{Tl}_{0.4}\text{CoO}_{5-\delta}$  [176], and  $\text{Bi}_{0.4}\text{Co}_{0.1}\text{Sr}_{2.5}\text{CoO}_{4.9}$  [177]. The ideal structure of these phases represented by  $\text{TlSr}_2\text{CoO}_5$  (Figure 1.17a) consists of single perovskite layers of  $\text{CoO}_6$  octahedra intergrown with double rock salt layers  $[\text{SrTiO}_2]_\infty$ , showing a tetragonal cell,  $a \sim 3.76 \text{ \AA}$  and  $c \sim 8.79 \text{ \AA}$ , with the space group  $P4/mmm$ . It is worth pointing out that this structure is very flexible, so that an excess of strontium can be introduced in the rock salt layer, without changing the space group, leading to an expansion of the  $c$ -parameter, as shown for the Sr-rich 1201 phase ( $\text{Sr}_{0.6}\text{Tl}_{0.4}$ ) $\text{Sr}_2\text{CoO}_{5-\delta}$  ( $a \sim 3.76 \text{ \AA}$  and  $c \sim 9.02 \text{ \AA}$ ). Note also that an oxygen deficiency may appear in the structure with respect to the “ $\text{O}_5$ ” composition.

The introduction of  $\text{Bi}^{3+}$  also stabilizes the 1201 structure, for the oxide ( $\text{Bi}_{0.4}\text{Sr}_{0.5}\text{Co}_{0.1}$ ) $\text{Sr}_2\text{CoO}_{4.9}$  [177], but with a different symmetry  $I4/mmm$  ( $a \sim 5.30 \text{ \AA}$  and  $c \sim 18.03 \text{ \AA}$ ), due to different distortions of the polyhedra and different distributions of the cations in the rock salt layers (Figure 1.17b).

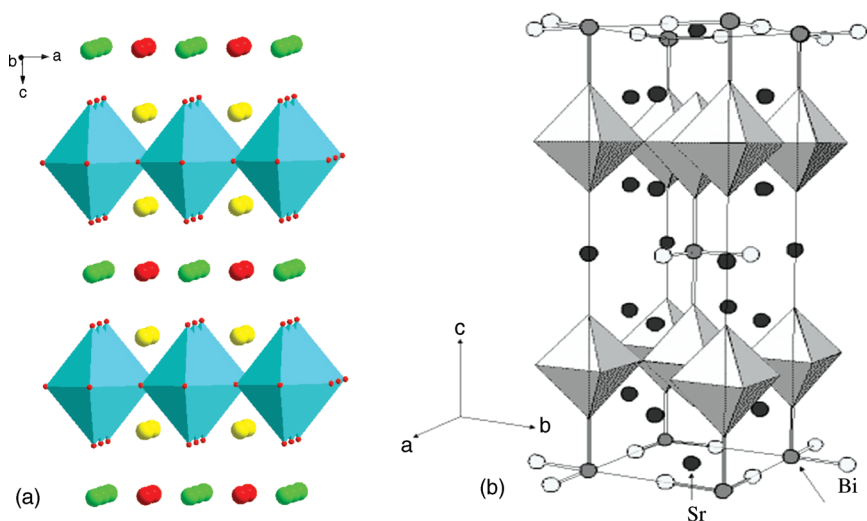


**Figure 1.17** Perspective view of the 1201 structure of (a)  $\text{TlSr}_2\text{CoO}_5$  made of  $[\text{SrO}]_\infty$ ,  $[\text{TlO}]_\infty$ , and  $[\text{CoO}_2]_\infty$  layers forming double rock salt layers  $[\text{SrTlO}_2]_\infty$  and single perovskite layers of  $\text{CoO}_6$  octahedra and (b)  $\text{Bi}_{0.4}\text{Co}_{0.1}\text{Sr}_{2.5}\text{CoO}_{4.9}$

with similar perovskite layers, and more complex double rock salt layers  $[\text{Bi}_{0.4}\text{Co}_{0.1}\text{Sr}_{1.5}\text{O}_2]$  involving a doubling of the  $c$ -parameter. Adapted from Ref. [176, 177].

Double intergrowths, which consist of the stacking of two types of rock salt layers with single perovskite layers in the same structure were also observed. It is the case of the Tl 1222 cobaltite,  $\text{Tl}_{0.9}\text{Sr}_3\text{LaCo}_2\text{O}_{8.6}$  [178], which structure (Figure 1.18) can be described as the intergrowth of single perovskite layers of  $\text{CoO}_6$  octahedra with double rock salt  $[\text{SrTlO}_2]_\infty$  layers and single  $[\text{SrO}]_\infty$  layers according to the sequence: “ $\text{CoO}_2\text{--SrO--TlO--SrO--CoO}_2\text{--SrO--SrO--CoO}_2$ .” Note that this oxide, which crystallizes in the space group  $I4/mmm$  with  $a \sim 3.78 \text{ \AA}$  and  $c \sim 30.30 \text{ \AA}$ , exhibits a possibility of nonstoichiometry on both sites, Tl and O.

The 2201 structure of  $\text{BiSr}_3\text{CoO}_{5.8}$  [179] represents the second type of intergrowths (Figure 1.19a), where triple rock salt layers  $[\text{BiSr}_2\text{O}_3]_\infty$  are stacked with single perovskite layers according to the sequence  $\text{CoO}_2\text{--SrO--(Bi,Sr)}_1\text{O--(Bi,Sr)}_1\text{O--SrO--CoO}_2$ . In these cobaltites, which exhibit the space group  $P12_1$  with  $a \sim 5.27 \text{ \AA}$ ,  $b \sim 5.30 \text{ \AA}$ , and  $c \sim 23.5 \text{ \AA}$ ,  $\gamma = 90^\circ$ , numerous distortions are observed, especially about the  $\text{CoO}_6$  octahedra that are strongly elongated along  $\vec{c}$ , so that they can better be described as  $\text{CoO}_5$  pyramids, whose apical corners are directed along two opposite directions along  $\vec{c}$  alternately (Figure 1.19b).

Changing the Bi/Sr ratio can also change the ordering of both these  $\text{CoO}_5$  pyramids and their waving in the 2201-type structure. This has been observed in the cobaltite  $\text{Bi}_2\text{Sr}_2\text{CoO}_{6+\delta}$  ( $\text{Bi}_8\text{Sr}_8\text{Co}_4\text{O}_{25}$ ) [180]. In this structure (Figure 1.20), double “BiO” layers are sandwiched between SrO layers and wave in the structure, whereas the “single” perovskite layers consist of quadruple ribbons of  $\text{CoO}_5$  pyramids whose apical corners are directed in opposite directions. This leads to a superstructure along  $\vec{a}$ , with the  $I2mb$  symmetry with  $a \sim 21.83 \text{ \AA}$ ,  $b \sim 5.46 \text{ \AA}$ , and

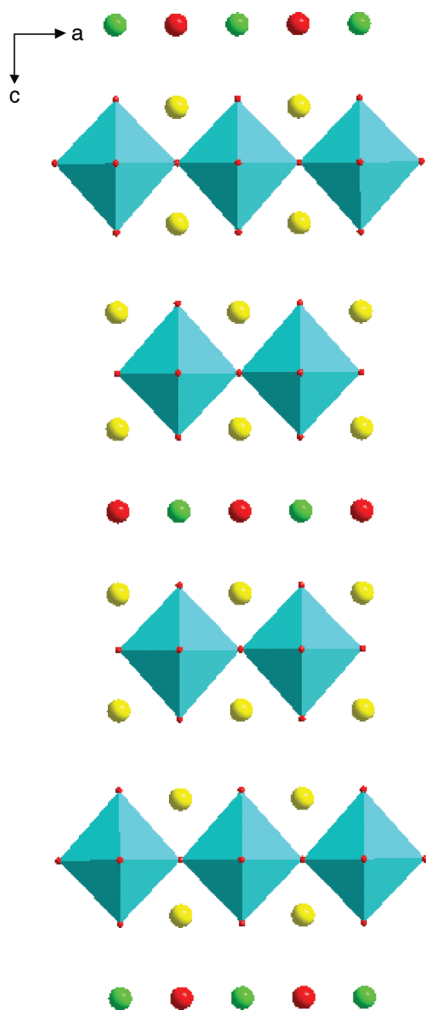


**Figure 1.18** Perspective view of the TI-1222 structure of  $\text{Tl}_{0.9}\text{Sr}_3\text{LaCo}_2\text{O}_{8.6}$ . Adapted from Ref. [178].

$c \sim 23.45 \text{ \AA}$ . In fact, the  $\text{Bi}_2\text{Sr}_2\text{CoO}_{6+\delta}$  phases exhibit both commensurate and incommensurate structures due to the presence of the  $6s^2$  lone pair of  $\text{Bi}^{3+}$  and to oxygen excess.

Moreover, the incommensurability can be modified by substituting partly lead for bismuth. For instance, in  $\text{Bi}_2\text{Sr}_2\text{CoO}_{6+\delta}$  an incommensurate structural modulation with the modulation vector  $q^* = 0.24b^* + c^*$  is observed [181, 182]. The polar group refinement leads to the superspace group  $F2mm (0\beta 1)00s$  for  $\text{Bi}_2\text{Sr}_2\text{CoO}_{6+\delta}$  [181].

The [BiO] layers got special attention due the modulated character of their structure and as potential charge reservoirs. The appearance of double BiO layers is usual for layered bismuth oxides and is a characteristic of 2201 and 2212 cuprates or ferrites. The modulation of these structures is mainly related to the configurations in

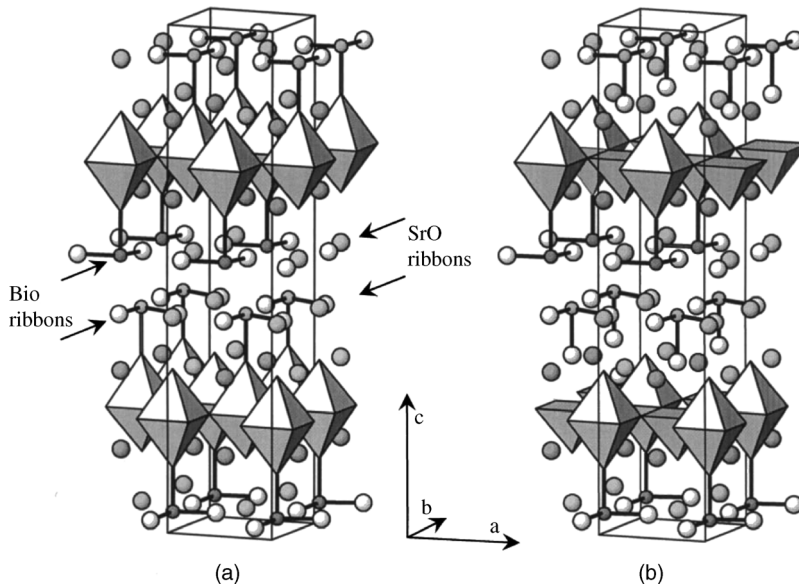


**Figure 1.19** Perspective view of the 2201 structure of  $\text{Bi}_{1-x}\text{Sr}_{3+x}\text{CoO}_{6-d}$  ( $\text{BiSr}_3\text{CoO}_{5.8}$ ). In (a) the cobalt environment is considered as octahedral, whereas in (b) it is assumed half-octahedral and half-square pyramidal due to the very long  $\text{Co}(2)\text{-O}$  distance. Adapted from Ref. [179].

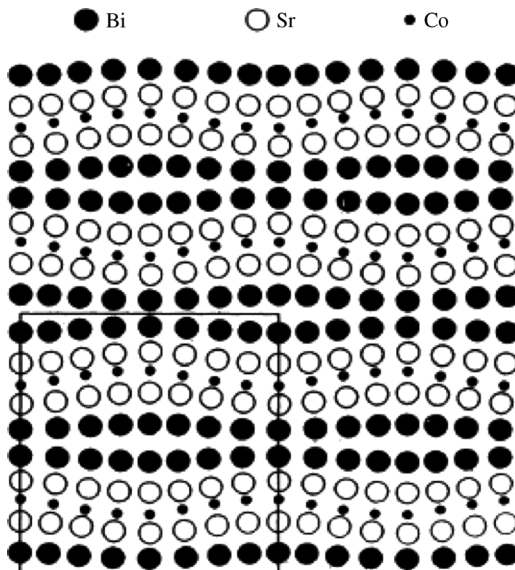


**Figure 1.20** Perspective view of the 2201-derivative structure of  $\text{Bi}_8\text{Sr}_8\text{Co}_4\text{O}_{25}$  ( $\text{Bi}_2\text{Sr}_2\text{CoO}_{6+d}$ ). Adapted from Ref. [180].

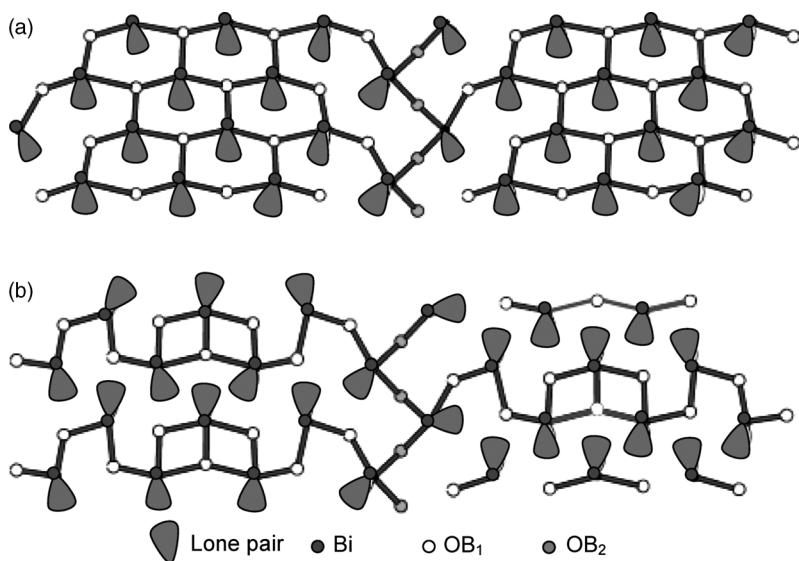


**Figure 1.21** (a) The honeycomb configuration of the BiO layer. Only OB<sub>1a</sub> sites are occupied and (b) the double-chain configuration of the BiO layer. OB<sub>1a</sub> and OB<sub>1b</sub> sites are alternately occupied. BiO interatomic distances < 2.6 Å are represented by solid lines. Adapted from Ref. [181].

the Bi and O arrangement. There are two regions, modulated (M zone) and nonmodulated (I zone) in the BiO layers. The origin of the modulation phenomenon lies in the interactions within and between [BiO] layers. The oxygen disorder observed in the M region leads to different possible configurations for the [BiO] layers. Of the two possible honeycomb and double-chain configurations of the Bi and O atoms (see Figure 1.21), the latter is the preferred configuration [181].

The substitution of Bi by Pb in Bi<sub>2-x</sub>Pb<sub>x</sub>Sr<sub>2</sub>CoO<sub>6</sub> leads to significant change in the structure [183]. Though for  $x=0.16$  one observes structural modulations with the modulation vector  $q^* = 0.245b^* + c^*$  and space group  $F2mm (0\beta 1)00s$ , the highly Pb-doped compound ( $x=0.8$ ) is no longer modulated. The modulation is now replaced by a new disordered atomic sequence that can be described as the simultaneous presence of two different structural configurations compatible with a single symmetry group  $Pnan$  [183]. The nonmodulated structure is the average structure of the modulated compound ( $F2mm (0\beta 1)00s$  symmetry). Interestingly, the honeycomb arrangement of the BiO layer is observed in the doped phase that was a possible hypothesis in the pure phase [181].

#### 1.7.4

##### Tubular Cobaltites

The 2201-type structure can be limited to one direction, forming infinite ribbons that are four CoO<sub>6</sub> octahedra (or CoO<sub>5</sub> pyramids) wide. This would generate a family of structures called “tubular structures,” with the generic formula

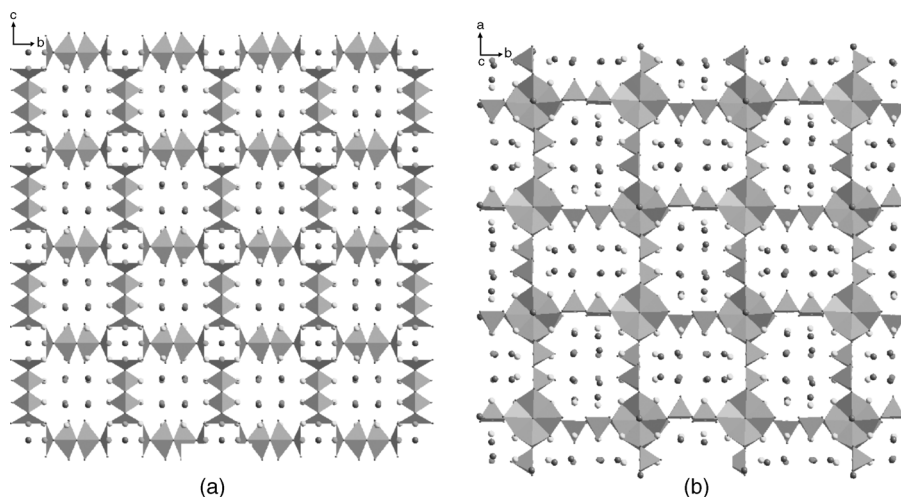


**Figure 1.22** The tubular structure of  $\text{Bi}_{4-x}\text{Sr}_{12-2x}\text{Co}_8\text{O}_{30-\delta}$  represented (a) as ribbons of  $\text{CoO}_6$  octahedra [184] or (b) as ribbons of  $\text{CoO}_5$  pyramids and  $\text{CoO}_6$  octahedra. Adapted from Ref. [185].

$(\text{Bi}_2\text{Sr}_2\text{CoO}_6)_n\text{Sr}_8\text{Co}_6\text{O}_{16-\delta}$ , whose  $n=2$  members, were described for  $\text{Bi}_{4-x}\text{Sr}_{12-2x}\text{Co}_8\text{O}_{30-\delta}$  with different space groups and parameters, that is,  $Fmmm$  with  $a \sim 5.52 \text{ \AA}$ ,  $b \sim 23.46 \text{ \AA}$ , and  $c \sim 23.46 \text{ \AA}$  or  $C222$   $a \sim 23.47 \text{ \AA}$ ,  $b \sim 23.48 \text{ \AA}$ , and  $c \sim 5.52 \text{ \AA}$  [184, 185]. In fact, in this structure the  $\text{CoO}_n$  polyhedra form perovskite ribbons that are four octahedra wide (Figure 1.22a) or two octahedra + two pyramids wide (Figure 1.22b). These polyhedra form square “tubes” bordered by  $\text{Sr}^{2+}$  cations, where double  $[\text{BiO}]_\infty$  ribbons are inserted.

## 1.8

### Cobaltites with a Triangular Lattice

#### 1.8.1

##### Spinel Cobaltites

The prototype of the cobalt spinels is the oxide  $\text{Co}_3\text{O}_4$  that exhibits the cubic normal spinel structure,  $Fd\bar{3}m$  space group, with  $a \sim 8.08 \text{ \AA}$  at room temperature [186]. The  $u$ -parameter of the 32 oxygen atoms of this cubic structure,  $u = 0.39$ , is close to the ideal value ( $u = 0.375$ ) of a perfect cubic close packing of the anionic framework of this structure (Figure 1.23a). In this normal spinel structure, the  $\text{Co}^{2+}$  cations sit in the 8a sites with tetrahedral coordination, whereas the  $\text{Co}^{3+}$  cations are located in the 16d sites, with octahedral coordination, according to the formula  $[\text{Co}^{2+}]_{8a}[\text{Co}^{3+}]_{16d}\text{O}_4$ . Thus, in terms of cobalt polyhedra the spinel structure of  $\text{Co}_3\text{O}_4$  can be described as the stacking of two sorts of polyhedral layers along the  $\langle 111 \rangle_c$  direction of the cubic cell: the kagomé layers (labeled K in Figure 1.23b) and the mixed layers of octahedra and tetrahedra (labeled M in Figure 1.23b). The well-known kagomé layers

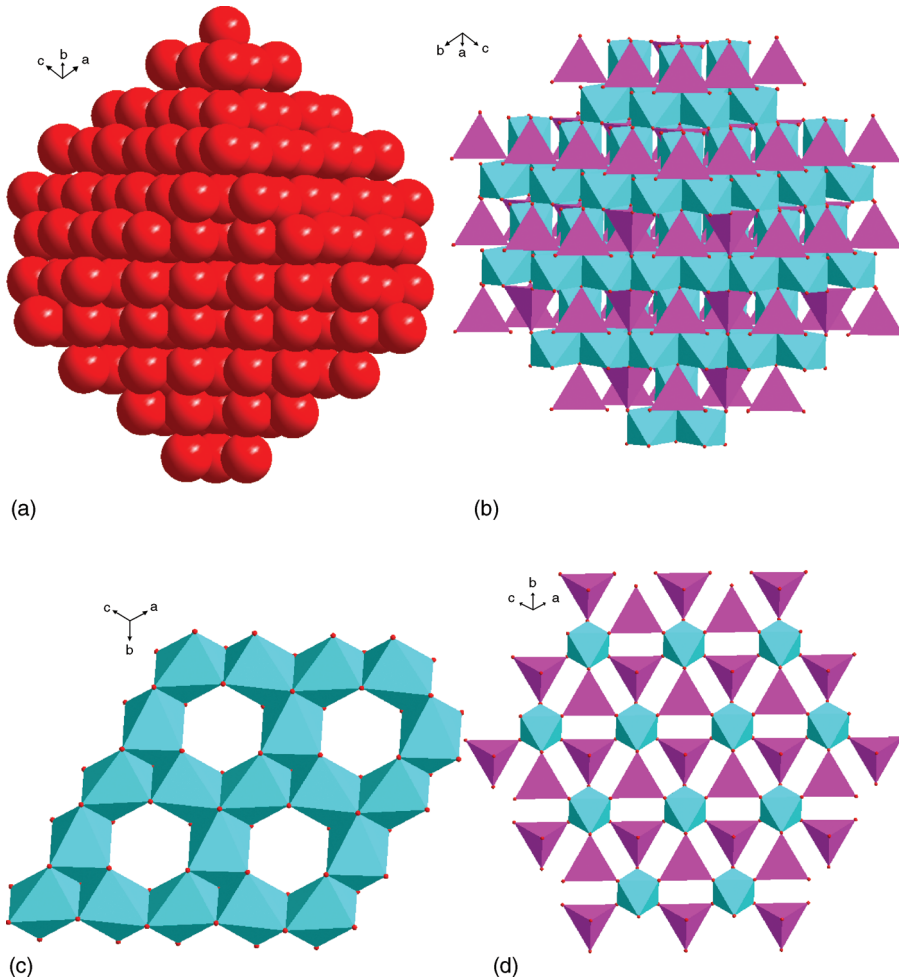


**Figure 1.23** Structure of the normal spinel oxide  $\text{Co}_3\text{O}_4$ : (a) 3D view of the structure showing the anionic close packing; (b) view along  $\langle 110 \rangle$  showing the stacking along  $\langle 111 \rangle$  of the kagomé layers (K) and the mixed layers (M); (c) view of one kagomé layer along

$\langle 111 \rangle$  showing the edge-sharing  $\text{Co}^{\text{III}}\text{O}_6$  octahedra; (d) view of one mixed layer along  $\langle 111 \rangle$  showing the corner-sharing  $\text{Co}^{\text{II}}\text{O}_4$  octahedra and  $\text{Co}^{\text{III}}\text{O}_6$  octahedra. Adapted from Ref. [186, 188].

(Figure 1.23c) consist of edge-sharing  $\text{CoO}_6$  octahedra forming hexagonal windows that are obstructed by the polyhedra of the mixed M layers. In the mixed layers (Figure 1.23d), the  $\text{Co}^{\text{II}}\text{O}_4$  tetrahedra and the  $\text{Co}^{\text{III}}\text{O}_6$  octahedra share their apices, each tetrahedron being linked to three octohedra of the same layer. Note that the  $\text{CoO}_4$  tetrahedra have their apical apex directed along the two opposite  $\langle 111 \rangle_c$  directions alternately.

It is worth noting that the anionic close packing of  $\text{Co}_3\text{O}_4$  is the same as that of the rock salt structure of  $\text{CoO}$  [187], so that it can be considered as a cation-deficient rock

salt structure, characterized by an ordering of the cobalt cations and the cationic vacancies, and charge ordering between  $\text{Co}^{2+}$  and  $\text{Co}^{3+}$  species. It is also remarkable that in this spinel structure, the  $[\text{Co}]_{\infty}$  sublattice forms a 3D tetrahedral framework, like the  $[\text{Ln}]_{\infty}$  lattice in the  $\text{Ln}_2\text{M}_2\text{O}_7$  pyrochlores. Moreover, the  $\text{Co}^{2+}$  cations at the 8a sites form a diamond lattice that consists of two displaced face-centered sublattices, being thus tetrahedrally surrounded by four nearest  $\text{Co}^{2+}$  neighbors.

Because of the variety of its magnetic properties – superparamagnetism, spin glass, and magnetic short-range order –  $\text{Co}_3\text{O}_4$  has also been studied as a nanocrystalline material [189–194]. Nanocrystalline  $\text{Co}_3\text{O}_4$  has indeed been synthesized by a number of ways, for example, sol–gel precipitation, oxidation of metallic cobalt foils, hydrothermal processes, polyol reduction, and electrospinning, in different forms such as one-dimensional (1D)  $\text{Co}_3\text{O}_4$ , colloidal forms, nanostructured mesoporous, thin films, nanowires, and nanorods [194].

There are a large number of cobalt-containing spinels formed by substitution of metal ions either at octahedral or at tetrahedral sites. These mixed spinel oxides can be considered as strategic material due to their tunable fascinating physical properties, such as electronic, magnetic, optical, and catalytic activity. The degree of substitution of cobalt by other metals retaining the structure of the parent  $\text{Co}_3\text{O}_4$  depends on the substituted metal. The site preference of the substituted metal also depends on the nature of the metal ion. Thus, the other relatives of the cobalt spinels can be represented as  $\text{M}_x\text{Co}_{3-x}\text{O}_4$ , where  $\text{M} = \text{Li}, \text{Al}, \text{Zn}, \text{Mg}, \text{Cu}, \text{Cr}, \text{Mn}, \text{Fe}, \text{Ni}$ , and so on. However, the preparation of spinel cobaltite by solid-state reaction puts a restriction. The cobalt spinels  $\text{M}_x\text{Co}_{3-x}\text{O}_4$  ( $0 < x < 1$  with  $\text{M} = \text{Ni}, \text{Cu}, \text{Zn}$ , and  $\text{Mg}$ ) are stable in a limited temperature interval. At temperatures in the range 1100–1200 K, the spinel structure of cobaltites is no longer stable, and a transformation to a rock salt structure takes place [195]. Again, depending on the nature of the divalent cation and the values of  $x$ , cobalt spinels decompose even at lower temperatures, evolving oxygen, MO, and a spinel phase with higher cobalt content [196, 197]. Cobaltites of Zn, Ni, and Cu were synthesized for the first time by Holgersson *et al.* [198] with cell parameters in the range 8.04–8.11 Å. The spinel  $\text{ZnCo}_2\text{O}_4$  has cell parameter  $a = 8.088$  Å with oxygen parameter  $u = 0.395$  and the zinc occupies the tetrahedral position [186]. In  $\text{Cu}_x\text{Co}_{3-x}\text{O}_4$  for  $x < 0.30$ , the spinels are normal and Cu was found only on tetrahedral positions. For  $x > 0.30$ , the spinels were found partly inverse [199]. It was also reported that for  $x > 0.2$  a transition from a normal to an inverse spinel occurred in  $\text{Cu}_x\text{Co}_{3-x}\text{O}_4$  [200]. By doping of  $\text{Co}_3\text{O}_4$  with nickel, the  $\text{Ni}^{3+}$  ions are stabilized, and they substitute for  $\text{Co}^{3+}$  in the octahedral sites, that is,  $[\text{Co}^{2+}]_{8a}[\text{Co}^{3+}_{2-x}\text{Ni}^{3+x}]_{16d}\text{O}_4^{2-}$  [201]. Note also that the Zn cobaltite possesses the highest thermal stability, followed by nickel cobaltite, whereas the copper cobaltite is of considerably lower thermal stability, compared to other binary cobaltites. That is why some attempts to synthesize these cobaltites have proved unsuccessful by heating at higher temperature, as shown for the copper cobaltite that decomposes into a mixture of two phases, CuO and a spinel with a lattice constant corresponding to  $\text{Co}_3\text{O}_4$  [196].

In the solid solution  $\text{Li}_x\text{Co}_{3-x}\text{O}_4$ , the lithium charge is compensated for  $\text{Co}^{4+}$  in the octahedral site. The lithium cation can be distributed on the tetrahedral and

octahedral sites depending on the synthesis temperature [202]. The spinel  $\text{CoAl}_2\text{O}_4$ , the so-called Thenard blue, has been known for a long time and has been extensively studied ( $a = 8.095 \text{ \AA}$ ) [203]. It may be considered as derived from  $\text{Co}_3\text{O}_4$  by replacing all the  $\text{Co}^{3+}$  with Al. However, for  $\text{AlCo}_2\text{O}_4$  ( $a = 8.086 \text{ \AA}$ ,  $u = 0.264$ ), 27% of Al is in tetrahedral positions [204]. The continuous substitution can be done for a wide range of concentrations. It has been observed that in  $\text{Co}[\text{Co}_{1-x}\text{Al}_x]_2\text{O}_4$  with increasing Al concentration, the lattice constant is found to increase and it follows Vegard's law. All the compositions crystallize in the cubic spinel structure with the space group  $Fd-3m$  [205]. In the spinel ferrimagnet,  $\text{CoCr}_2\text{O}_4$ , the  $\text{Co}^{2+}$  ions occupy the A-sites and  $\text{Cr}^{3+}$  the B-sites of the spinel structure. The space group of this cubic spinel structure is  $Fd-3m$  with the lattice parameter  $a = 8.3351 \text{ \AA}$  and oxygen parameter  $u = 0.264$  determined by the NPD data [206].  $\text{Co}_{3-x}\text{Mn}_x\text{O}_4$  ( $x = 0-1.2$ ) is a normal cubic spinel at room temperature and the charge distribution is represented by  $[\text{Co}^{2+}]_{8a}[\text{Co}^{3+}_{2-x}\text{Mn}^{3+x}]_{16d}\text{O}^{2-}_4$  [207]. The normal cubic spinel structure retains up to  $x = 1.0$  with increase in Mn substitution [208]. The substitution of  $\text{Co}^{3+}$  by  $\text{Mn}^{3+}$  leads to an increase in the lattice parameter,  $a$ , due to the large ionic radius of  $\text{Mn}^{3+}$  in comparison to that of  $\text{Co}^{3+}$  occupying the octahedral sites.

### 1.8.2

#### $\text{Na}_x\text{CoO}_2$ -Type Lamellar Oxides

First discovered in the 1970s [209, 210], the cobaltites  $\text{Na}_x\text{CoO}_2$  oxides exhibit various types of polymorphs with a lamellar structure built up of  $\text{CoO}_6$  octahedra forming  $[\text{CoO}_2]_\infty$  layers of  $\text{CdI}_2$ -type of edge-sharing octahedra, interleaved with  $\text{Na}^+$  cations (Figure 1.24). This structure was also observed for  $\text{Ca}_x\text{CoO}_2$  oxides [211].

The various structures of these bronzes, which exhibit the mixed valence  $\text{Co}^{3+}/\text{Co}^{4+}$ , differ from each other by the relative positions of the  $[\text{CoO}_2]_\infty$  layers,

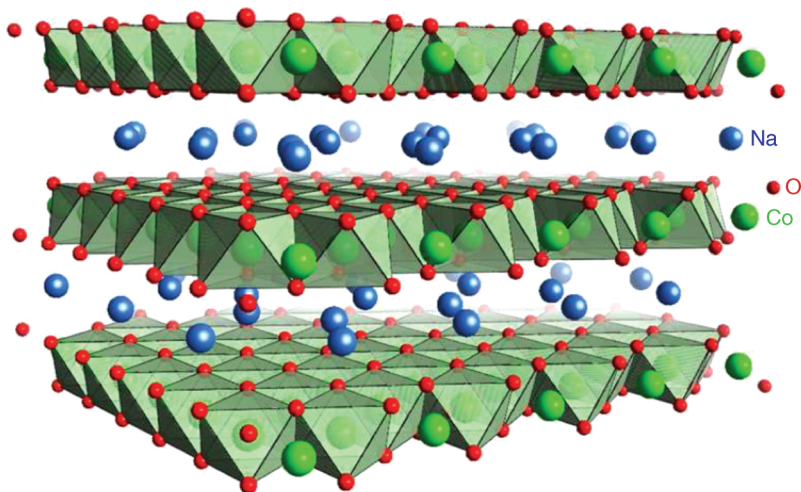
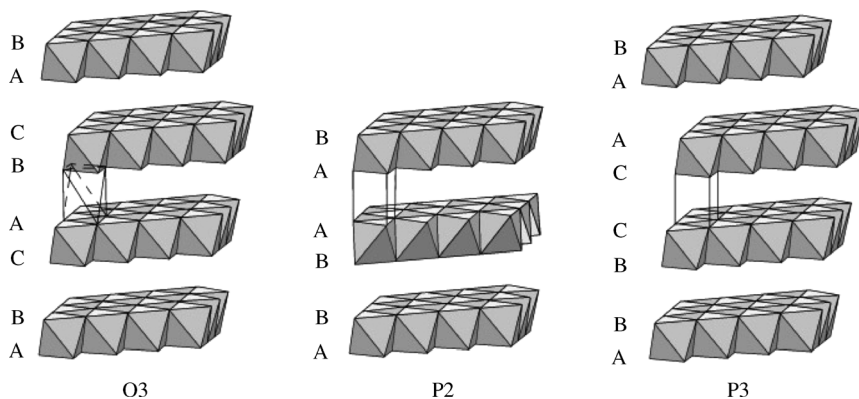


Figure 1.24 Perspective view of the crystal structure of  $\text{Na}_x\text{CoO}_2$ .



**Figure 1.25** The  $O3$  ( $\alpha$ -phase),  $P2$  ( $\gamma$ -phase), and  $P3$  ( $\beta$ -phase) structures ( $O$ , octahedral coordination of the A cation;  $P$ , trigonal prismatic coordination of the A cation; 2, 3 are the number of layers in the repeat).

depending on the sodium content  $0.30 \leq x \leq 1$ . For high sodium content,  $x = 1$ , a rhombohedral,  $R\bar{3}m$  structure is observed with  $a \sim 2.88 \text{ \AA}$  and  $c \sim 15.6 \text{ \AA}$  [211], where sodium adopts the octahedral coordination between the  $[\text{CoO}_2]_\infty$  layers (Figure 1.24). In fact, the  $\text{NaCoO}_2$  structure (labeled  $O3$ ) exhibits a cubic anionic close packing (ABCABC) of the rock salt type, where  $\text{Na}^+$  and  $\text{Co}^{2+}/\text{Co}^{3+}$  are distributed in an ordered way in the octahedral sites. As the sodium content decreases, a number of structural variations can occur, including the  $P3$  and  $P2$  structures with ABBCA and ABBA oxygen packing sequences, respectively ( $P$  is the trigonal prismatic coordination of alkali metal; prime ( $'$ ) denotes a monoclinic distortion of the unit cell) (Figure 1.25). The familiar way to look at the structure of  $\text{Na}_x\text{CoO}_2$  is as follows. The structure of  $\text{Na}_x\text{CoO}_2$  consists of  $\text{CdI}_2$ -type  $\text{CoO}_2$  layers intercalated with  $\text{Na}^+$  ions with a trigonal prismatic ( $P$ ) or octahedral ( $O$ ) environment. There are four unique structural forms of  $\text{Na}_x\text{CoO}_2$ ,  $\alpha$ -,  $\alpha'$ -,  $\beta$ -, and  $\gamma$ -phases; they differ in the stacking sequence of the close-packed oxygen layers that are perpendicular to the  $c$ -axis [210–213].

Thus, the symmetry of these four different phases is governed by the sodium content:

- The  $\alpha$ -form that exhibits the hexagonal symmetry  $P6_3/mmc$ , with  $a \sim 2.88 \text{ \AA}$  and  $c \sim 15.56 \text{ \AA}$ , is obtained for  $0.9 \leq x \leq 1$ . It is often called the  $O3$  structure ( $O$  indicates the octahedral coordination of  $\text{Na}^+$  and 3 is the number of layers in repeat).
- The  $\alpha'$ -form is synthesized for  $x = 0.75$ . Called the  $O'3$  structure, it can be described as a monoclinic distortion of the  $O3$  structure, with  $a \sim 4.89 \text{ \AA}$ ,  $b \sim 2.87 \text{ \AA}$ ,  $c \sim 5.77 \text{ \AA}$ , and  $\beta \sim 111^\circ 28'$  [210].
- The  $\beta$ -phase exists for  $0.55 \leq x \leq 0.60$  and corresponds to the  $P3$  structure ( $P$  indicates the prismatic coordination of  $\text{Na}^+$ , and 3 is the number of layers in repeat) [214]. It adopts the  $C2/m$  space group with lattice parameters  $a \sim 4.9 \text{ \AA}$ ,  $b \sim 2.83 \text{ \AA}$ ,  $c \sim 5.72 \text{ \AA}$ , and  $\beta \sim 105.97^\circ$ .

- The  $\gamma$ -phase is observed for  $0.55 < x < 0.74$ . This  $P2$  structure (prismatic coordination of  $\text{Na}^+$ , and 2 is the number of layers in repeat) exhibits the hexagonal symmetry, with the space group  $P6_3/mmc$  and lattice constants of  $a \sim 2.84 \text{ \AA}$  and  $c \sim 10.81 \text{ \AA}$  [211].

In  $\beta\text{-Na}_x\text{CoO}_2$ , all the  $\text{Na}^+$  ions occupy a single type of prismatic site that on the one side shares a face and on the other side shares edges with surrounding  $\text{CoO}_6$  octahedra. This situation is very different from that of  $\gamma\text{-Na}_x\text{CoO}_2$ , where two distinct prismatic sites are found: one shares only faces, whereas the second shares only edges with  $\text{CoO}_6$  octahedra. The  $\gamma$ -phase ( $P2$  type) is characterized by a stacking sequence of close-packed oxygen atoms . . . ABBAABBA . . . , with the oxygen atoms on each side of the Na layers being identical. In this structure,  $\text{Na}^+$  exhibits two different prismatic coordinations within a given plane and are represented as Na(1) and Na(2) cations. Basically, the Na(1) and Na(2) species form two interpenetrating triangular lattices. The prism of each Na(1) site shares two triangular faces with Co octahedra, one Co lying vertically above the Na (along  $c$ ) and the other vertically below; the Na(2) site shares only edges with the Co octahedra. The Na(1) site is energetically less favorable than Na(2), owing to electrostatic repulsions with the two cobalt ions in adjacent layers. It is generally assumed that  $\text{Na}^+$  cannot occupy adjacent Na(1) and Na(2) sites since their separation is too small ( $\sim 1.63 \text{ \AA}$ ) [215]. However, quite large displacements of both Na(1) and Na(2) occur, which could increase this distance locally to  $\sim 2.0 \text{ \AA}$  or more, and make such an occupancy a possible event, especially at elevated temperatures. The complexity of Na vacancy ordering in this system arises in part from this competition between the Na(1)-Na(2) sites energy difference and from the  $\text{Na}^+ - \text{Na}^+$  electrostatic repulsion.

Figure 1.26 shows the stacking of  $\text{NaO}_6$  prisms and  $\text{CoO}_6$  octahedra in  $\beta\text{-Na}_{0.67}\text{CoO}_2$  and  $\gamma\text{-Na}_{0.70}\text{CoO}_2$ . In  $\beta\text{-Na}_{0.67}\text{CoO}_2$ , the upper oxygen atoms of the

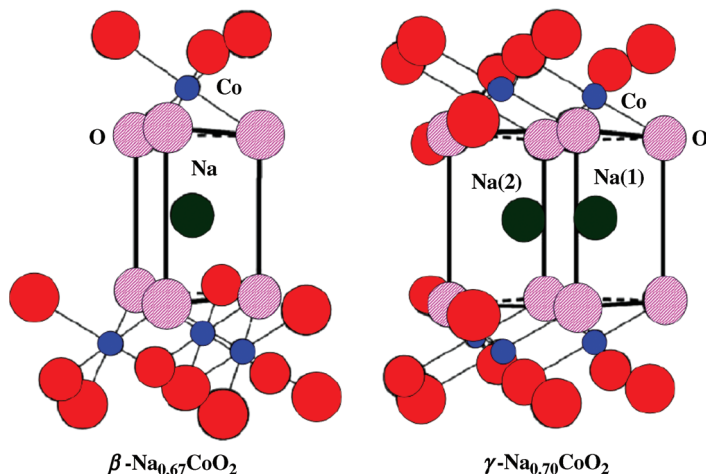


**Figure 1.26** Stacking of  $\text{NaO}_6$  prisms and  $\text{CoO}_6$  octahedra in  $\beta\text{-Na}_{0.67}\text{CoO}_2$  and  $\gamma\text{-Na}_{0.70}\text{CoO}_2$ . Hatched circles represent the oxygen atoms forming  $\text{NaO}_6$  prisms with  $\text{Na}^+$  sites at their centers. Adapted from Ref. [214].

prism are shared with a  $\text{CoO}_6$  octahedron, but lower oxygen atoms are shared with three  $\text{CoO}_6$  octahedra. In  $\gamma\text{-Na}_{0.70}\text{CoO}_2$ , there are two kinds of prisms, namely,  $\text{Na}(1)\text{O}_6$  and  $\text{Na}(2)\text{O}_6$  [216]. The  $\text{Na}(1)\text{O}_6$  prism shares two sets of three oxygen atoms with one upper and one lower  $\text{CoO}_6$  octahedra, respectively. On the other hand, the  $\text{Na}(2)\text{O}_6$  prism shares two sets of three oxygen atoms with upper and lower three  $\text{CoO}_6$  octahedra, respectively.

From the above discussion, it is clear that the structure contains two different environments for sodium:  $\text{Na}(1)$  that lies between adjacent cobalt ions and  $\text{Na}(2)$  that sits on a lower energy site at the center of a cobalt trigonal prism. Therefore,  $\text{Na}^+$  ions will normally prefer to occupy the  $\text{Na}(2)$  sites. The nature of sodium ordering over the available sites is important because it is expected that at a certain composition, the confinement of stable sodium ordered superstructures is likely to influence the properties. The precise Na arrangement will be governed by the opposing demands of entropy and enthalpy. At low Na concentrations, entropic effects appear dominant and the Na layer is highly disordered. However, at higher levels, the  $\text{Na}^+$  ions tend to organize themselves to minimize the ionic repulsion between them at any given layer. For this reason, occupancy of both sites is preferred. In this way, the Na rich compositions present a variety of Na arrangements that reflect the competition between these two factors. At low Na concentration, the stable phase only with  $\text{Na}(2)$  sites' occupation is observed at  $x = 1/3$ .

However, it is observed experimentally that at  $x = 1/2$  an equal occupation of  $\text{Na}(1)$  and  $\text{Na}(2)$  sites takes place [217, 218]. As the sodium content increases, from  $x = 0.5$  to  $x = 0.75$ , the added sodium fills the  $\text{Na}(2)$  sites only [219]. The long-range superstructure of sodium whose pattern is well accounted for by electrostatic interactions and the amount of sodium vacancies in the lattice has been reported in the literature. The long-range Coulomb interactions then allow these vacancy clusters to order over a long range, leading to observable superstructure peaks. However, the proper characterization of the Na ordering pattern faces several difficulties, especially in the highly doped region. The Na and vacancy ordering depends on the exact sodium content, which is difficult to control due to Na diffusion and aggregation.

Whether the  $\text{Na}^+$  cations are ordered or randomly distributed within their planar sublattice is a permanent issue and that is widely debated. For example, remarkable differences exist in the ground-state structures of  $\text{Na}_{0.75}\text{CoO}_2$  and at high concentrations of  $\text{Na}^+$  cations [220–222]. Extensive experimental and computational investigations have been carried out to find out the stable sodium vacancy orderings at various sodium concentrations [220–224]. However, a few experimental evidences of long-range ordering, either commensurate or incommensurate, have been given using neutron or electron diffraction and most of the reported works are devoted to theoretical considerations using various methods of calculation [221–223]. A detailed electron diffraction study on powder samples revealed several new structures [220]. For instance, the  $x = 0.5$  composition shows commensurate superstructure reflections for relatively low exposure time to electron beam with the vector  $q$  along the  $[110]$  direction. However, the commensurate superlattice at  $x = 0.5$  evolves continuously to an incommensurate superlattice with small changes in sodium content induced

during electron beam irradiation. This indicates that a continuously varying structural modulation that is a function of sodium content has locked into a commensurate modulation at  $x=0.5$ . The commensurate superstructure can also be described with a three-dimensional unit cell, which is orthorhombic in nature. All the compositions with  $x=0.15, 0.30, 0.35, 0.5, 0.64,$  and  $0.75,$  except  $x=0.55,$  are shown to exhibit superstructure reflections [220]. The unit cell of the superstructure is determined by the width of the repeat of the lines of vacancies and Na. The choice of occupying the Na(1) or Na(2) position in the Na chain and the stacking of the ordering in the Na planes will determine the space group and the intensities of the superstructure reflections. Both the variation in the intensities of the superstructure reflections for various values of  $x$  and differences in the systematic absences for one value of  $x$  all indicate that the ordering along the  $c$ -axis is variable.

The various structures proposed based on electron diffraction investigations were also confirmed by an *ab initio* study using the local density approximation (LDA) to density functional theory (DFT) method [222, 223, 225]. New ground states were proposed for  $x=0.60, 0.80,$  and  $0.83,$  within the limitation that the patterns could fit in small unit cells [222]. Figure 1.27 shows the possible ordered structures of  $\text{Na}_x\text{CoO}_2$ . Single-crystal neutron diffraction showed that at large Na concentrations, the Na vacancy organizational principle is the stabilization of droplets of Na(1) occupation that are long-range ordered at some simple fractional fillings, such as  $0.75$  and  $0.80$  [221]. An ordering of multivacancy clusters within the sodium layer for  $x > 0.7$  was proposed, that is,  $\text{Na}^+$  ions shift from the preferred Na(2) site to the unfavorable Na(1) site that is directly on top of the cobalt ions to further reduce the stabilization energy. Unusual long-range ordering pattern of tri-Na(1) droplet was proposed for  $x > 0.75$  concentration [221].

The  $c$  lattice parameter is a good measure of the sodium concentration: it increases as the sodium concentration decreases. Thus, only simple diffraction data may be used as a method to estimate the Na composition. The  $c$  lattice parameter depends almost linearly on  $x$  with a weak deflection near  $x=0.55$ . This behavior may suggest two regimes that follow the empirical Vegard's rule for substitutional impurities [226]. The Na(1)/Na(2) ratio is another important structural parameter. Compared to the  $c$  lattice parameter that varies smoothly with Na concentration, the Na(1)/Na(2) ratio varies in an irregular manner. However, errors in the Na(1) and Na(2) site energy difference show up in the Na(1)/Na(2) ratio but not necessarily in the  $c$  lattice parameter [227, 228].

The cobaltite  $\text{Na}_{0.5}\text{CoO}_2$  that goes from an insulating behavior at low temperature to a metallic behavior above  $51\text{ K}$  is an example of the charge ordering that appears in this oxide below  $T_{\text{Co}} = 51\text{ K}$ . The holes are ordered in the  $\text{CoO}_2$  layers together with the  $\text{Na}^+$  ions. Characterization of  $\text{Na}_{0.5}\text{CoO}_2$  by electron diffraction revealed the presence of an orthorhombic supercell, which was attributed to Na ordering and to an associated charge ordering of the underlying cobalt layer [217]. The ordering of  $\text{Na}^+$  ions at  $x=0.5$  is distinct from the commonly observed spatially ordered state of sodium for certain values of  $x$ . In the case of  $\text{Na}_{0.5}\text{CoO}_2$ , electron and neutron diffraction measurements have suggested that  $\text{Na}^+$  ions form zigzag chains [217, 218, 220]. This results in the presence of two structurally inequivalent

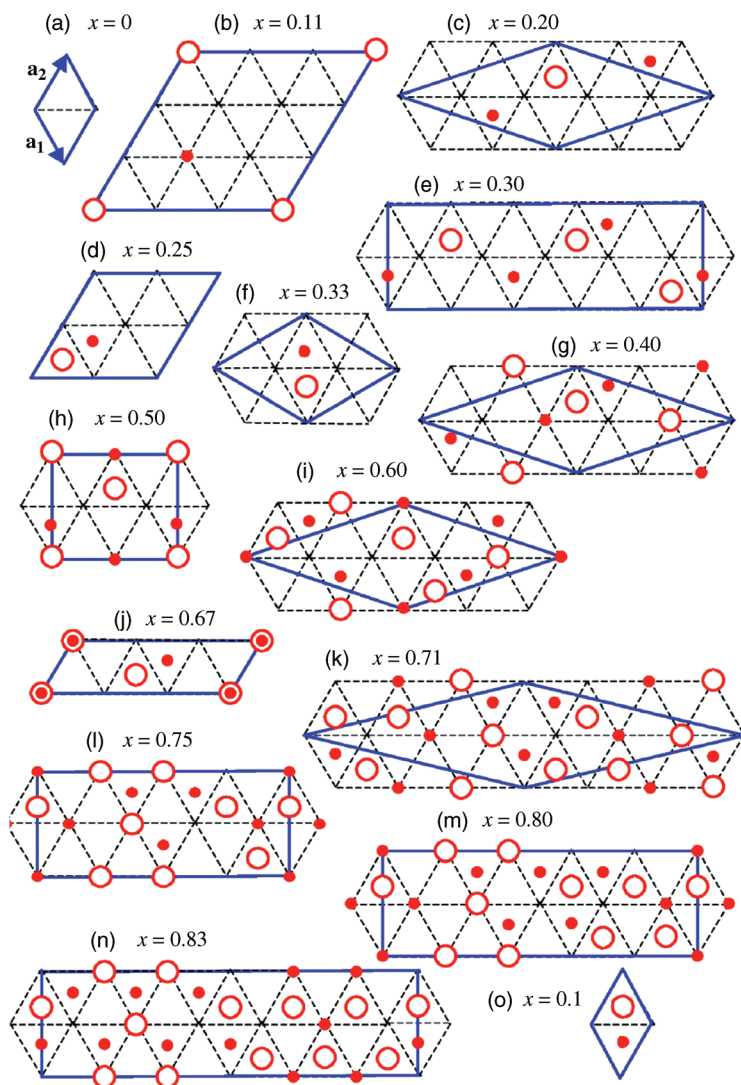


**Figure 1.27** Relevant ordered structures of  $\text{Na}_x\text{CoO}_2$ . The dashed lines represent the projected triangular lattice of Co atoms. Large red open circles and small red dots represent projected Na positions in different planes, at

$z = 0$  and  $z = 0.5c$ , respectively. The Na(1) sites fall on top of the triangular lattice sites and Na(2) sites fall in the center of the triangles. Blue lines indicate the minimum unit cell in each case. Adapted from Ref. [222].

Co sites, each forming a chain arrangement. One of the nearest-neighbor sites of Co(1) is occupied by a  $\text{Na}^+$  cation, while Co(2) has no  $\text{Na}^+$  cation in the nearest-neighbor sites [217]. Since the Coulomb potential from  $\text{Na}^+$  zigzag chains attracts electrons, the valence of Co(1) sites,  $\text{Co}^{+3.5-\delta}$ , is smaller than that of the Co(2) sites,  $\text{Co}^{+3.5+\delta}$ . The average valence of cobalt in  $\text{Na}_{0.5}\text{CoO}_2$  is +3.5 [229]. Thus, the

distinct behavior of Co(1) and Co(2) sites is directly linked to the periodic Coulomb potential arising from  $\text{Na}^+$  chains, the charges on cobalt sites becoming mobile above  $T_{\text{CO}}$  in the metallic state. Charge ordering within the cobalt layers has also been claimed for the compositions  $x = 0.70$  [230], 0.75 [231], and 0.82 [232].

The discovery of superconductivity in  $\text{Na}_x\text{CoO}_2 \cdot \gamma\text{H}_2\text{O}$ , with  $T_c \sim 5$  K [212] has attracted a lot of attention. This phase exhibits a crystal structure similar to that of  $\text{Na}_{0.7}\text{CoO}_3$ , with similar space group  $P6_3/mmc$  and cell parameters ( $a \sim 2.8$  Å and  $c \sim 19.6$  Å) but with a different sodium content,  $x \sim 0.35$ . The structure of the  $\text{CoO}_2$  sheets of  $\text{Na}_{0.35}\text{CoO}_2 \cdot 1.3\text{H}_2\text{O}$  is very similar to that of the parent compound  $\text{Na}_{0.7}\text{CoO}_2$ , the in-plane  $a$  lattice parameter being slightly contracted, owing to the lower Na content that results in the partial oxidation of the  $\text{Co}^{3+}$  ions to smaller  $\text{Co}^{4+}$  ions. On the other hand, the  $c$ -parameter increases dramatically from 10.96 to 19.62 Å due to the water intercalation that changes the relative orientation of the successive  $\text{CoO}_2$  layers (Figure 1.28).

Thus, besides the mixed valence  $\text{Co}^{3+}/\text{Co}^{4+}$ , the ordering of  $\text{Na}^+$  and vacancies that governs the charge ordering on cobalt sites has a great impact upon the physical properties of these lamellar oxides, as will be discussed in section 6.

Besides the  $\text{Na}_x\text{CoO}_2$  bronzes that have been extensively studied, some other alkaline cobaltites exhibit the same type of structure. It is the case of the  $\text{K}_x\text{CoO}_2$  phases, with  $x = 0.50$  and 0.69, which are hexagonal  $P6_3/mcm$  with  $a \sim 2.84$  Å and

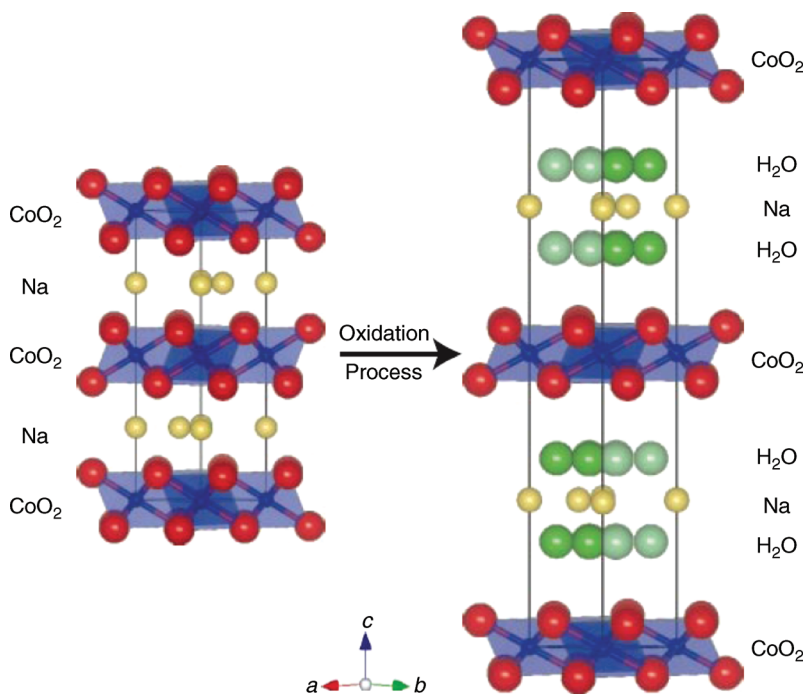


**Figure 1.28** Two-dimensional  $\text{CoO}_2$  layers separated by a thick insulating layer of  $\text{Na}^+$  ions and  $\text{H}_2\text{O}$  molecules in superconducting  $\text{Na}_x\text{CoO}_2 \cdot \gamma\text{H}_2\text{O}$ . Adapted from Ref. [212].

$c \sim 13.35 \text{ \AA}$  [209, 233], and of  $\text{K}_4\text{Co}_7\text{O}_{14}$  [234], which exhibits a different space group  $P6_3/m$  and different cell parameters,  $a \sim 7.51 \text{ \AA}$  and  $c \sim 12.37 \text{ \AA}$ , due to ordering of the  $\text{K}^+$  cations.

The lithium cobaltites  $\text{Li}_x\text{CoO}_2$  were also shown to exhibit a similar type of lamellar structure for  $x$  ranging from 0.35 to 1, with the  $R\bar{3}m$  symmetry and lattice parameters  $a \sim 2.8\text{--}2.9 \text{ \AA}$  and  $c \sim 13.7\text{--}14.2 \text{ \AA}$  [233, 235–245].

Note that in these oxides, the size of  $\text{Li}^+$ , close to that of  $\text{Co}^{3+}/\text{Co}^{4+}$ , makes the structure close to that of an ordered rock salt cobaltite, where layers of  $\text{CoO}_6$  octahedra alternate with layers of  $\text{LiO}_6$  octahedra as shown for  $\text{LiCoO}_2$  (Figure 1.29). Other forms of  $\text{Li}_x\text{CoO}_2$  oxides with a closely related structure are obtained by using different methods of synthesis. This is the case for  $\text{Li}_{0.5}\text{CoO}_2$  [246] whose monoclinic  $P2_1/m$  structure with  $a \sim 4.86 \text{ \AA}$ ,  $b \sim 2.80 \text{ \AA}$ ,  $c \sim 5.06 \text{ \AA}$ , and  $\beta \sim 108.7^\circ$  consists of the same  $[\text{CoO}_2]_\infty$  layers, interleaved with ordered lithium-deficient layers of  $\text{LiO}_6$  octahedra. In the latter, one row of lithium cations alternates with one row of cationic vacancies. Another different form was also synthesized for  $\text{Li}_{0.56}\text{CoO}_2$  [247], which crystallizes in the  $Cmca$  symmetry with  $a \sim 2.80$ ,  $b \sim 4.84$ , and  $c \sim 9.95 \text{ \AA}$ . Again, in this structure, the  $[\text{CoO}_2]_\infty$  layers of  $\text{CoO}_6$  octahedra are similar to those described above, that is, of the  $\text{CdI}_2$  type, but the interleaved lithium cations exhibit a different distorted tetrahedral coordination. A metastable form of oxygen-deficient lamellar cobaltite,  $\text{Li}_{1.03}\text{Co}_{0.97}\text{O}_{1.88}$ , has been synthesized [249], which is also made of  $[\text{CoO}_2]_\infty$  layers of the  $\text{CdI}_2$  type. In this structure, which crystallizes with the  $P6_3mc$  symmetry, with  $a \sim 2.80$  and  $c \sim 9.53 \text{ \AA}$ , the interleaved  $\text{Li}^+$  cations adopt two different distorted,  $6 + 1$  and fourfold, coordination. Note that the lithium cobaltites, different from the sodium cobaltites, are studied more especially for application of their electrochemical properties in lithium ion batteries.

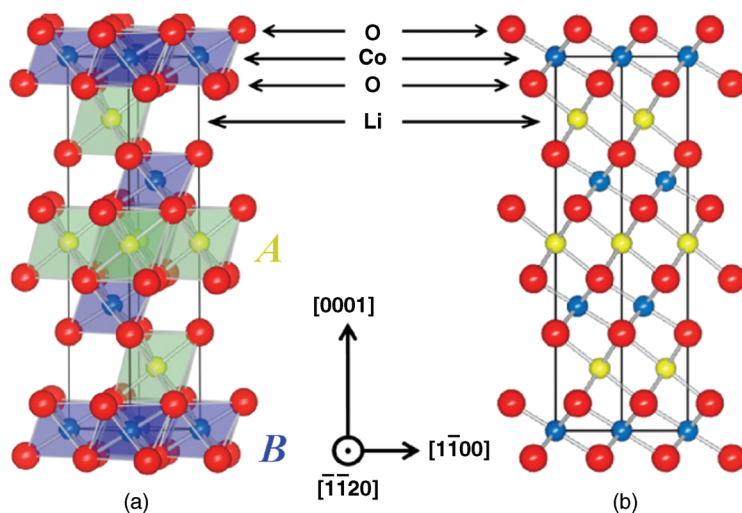


**Figure 1.29** (a) Perspective view of the structure of rhombohedral  $\text{LiCoO}_2$  showing layers of  $\text{LiO}_6$  octahedra (labeled A) alternately stacked with layers of  $\text{CoO}_6$  octahedra (labeled B) and (b) the atomic configuration projected along the  $[-1-120]$  direction. Adapted from Ref. [248].

## 1.8.3

**The Misfit Cobaltites**

The misfit cobaltites are, like the  $\text{Na}_x\text{CoO}_2$  cobaltites, very attractive materials for their thermoelectric properties and for this reason are investigated by many groups from the physics viewpoint and for applications. The misfit structure in oxides and especially in cobaltites was discovered for the first time in 1998 with the synthesis of “Tl-Sr-Co” oxides [250, 251] and then in the “Bi-Sr-Co” oxides [252]. The misfit cobaltites are, in fact, composite structures consisting of two distinct layers with different crystal lattices. The first crystal lattice (labeled 1) forms a square or pseudo-square lattice: it consists of multiple  $(\text{AO})_n$  layers, with  $A = \text{Tl, Ba, Sr, Ca, Bi, and Co}$ , which exhibit a rock salt-type structure, like in the RP phase and derivatives. The second crystal lattice (labeled 2) is triangular, that is, pseudo-hexagonal and corresponds to the cobalt–oxygen lattice: it consists of  $[\text{CoO}_2]_\infty$  layers of the  $\text{CdI}_2$  type similar to those observed in the hexagonal  $\text{Na}_x\text{CoO}_2$  cobaltites. Thus, most of the misfit compounds crystallize in the monoclinic  $C2/m$  space group where both the RS and the  $\text{CdI}_2$ -type lattices have a monoclinic symmetry with identical  $a$ ,  $c$ , and  $\beta$  parameters but different  $b$  parameters. The typical cell parameters are  $a \sim 4.8 \text{ \AA}$ ,  $c \sim 10.8 \text{ \AA}$ , and  $\beta \sim 98^\circ$ , whereas  $b_1 \sim 4.5 \text{ \AA}$  for the rock salt lattice and  $b_2 \sim 2.8 \text{ \AA}$  for the  $[\text{CoO}_2]_\infty$  lattice.

The stacking of the triangular lattice with a square lattice results in significant distortions at the interface since the  $b$ -axis dimensions in each layer are very different, and for these reasons, these oxides are called misfits. The general formula of those misfit cobaltites can be expressed as  $[\text{AO}]_n^{\text{RS}}[\text{CoO}_2]_p$ , with  $A = \text{Tl, Ba, Sr, Ca, Co, and Bi}$ , where  $n$  is the number of AO layers in the rock salt block and  $p$  is the ratio between the two different cell parameters ( $p = b_1/b_2$ ), the subscripts 1 and 2 referring to rock salt and  $\text{CdI}_2$  sublattices, respectively. These misfit structures can be described as well by the generic formula  $[(A'_{1-x}\text{Co}_y)_{n-2}\text{A}_{2+x-y}\text{O}_n]^{\text{RS}}[\text{CoO}_2]_p$  in which  $n$  is the number of RS-type layers ( $n = 3$  or  $4$  and  $A' = \text{Co, Bi, Tl, Pb, \dots}$  and  $A = \text{Ca, Sr}$ ) [253–257] and  $p$  represents the incommensurate ratio  $b_{\text{RS}}/b_{\text{CoO}_2}$  of the  $b$ -parameters of the two subsystems. Again, since almost all the misfit cobalt oxides discovered so far contain alkali-earth elements and other metallic elements in the RS-type subsystem, the compounds can also be described as  $[\text{A}_2\text{M}_x\text{O}_{2+x}]_q\text{CoO}_2$ , where  $A$  and  $M$  stand for alkali-earth and metallic atoms [258]. However, in such a notation  $q$  is defined as the ratio  $b_{\text{CoO}_2}/b_{\text{RS}}$ .

Depending on the thickness of the rock salt-type layers, one can distinguish two sorts of misfits: those containing three rock salt layers (built up of  $n = 3$  AO layers) and those containing four rock salt layers (built up of  $n = 4$  AO layers). Note also that additional complexity in these structures is introduced by the presence of ordered oxygen defects. One of the most extensively studied systems is the calcium cobaltite that was expressed in different ways by various authors as  $\text{Ca}_3\text{Co}_4\text{O}_9$  [259–261],  $\text{Ca}_9\text{Co}_{12}\text{O}_{28}$  [262], and  $\text{Ca}_2\text{Co}_2\text{O}_5$  [263]. In fact, this cobaltite corresponds to the formulation  $[\text{Ca}_2\text{CoO}_3][\text{CoO}_2]_{1.62}$ . Its structure has been described by several groups successively [259, 264–267]. The structure of the simplest form (Figure 1.30) consists of two interpenetrating monoclinic subsystems. The two subsystems are single  $\text{CoO}_2$  sheets of the  $\text{CdI}_2$  type (first subsystem) and triple  $\text{Ca}_2\text{CoO}_3$  layers ( $n = 3$ ) of the rock

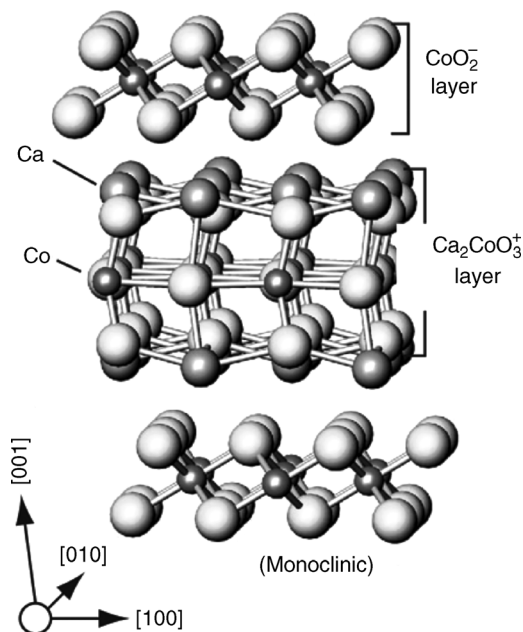


**Figure 1.30** Schematic structure of the misfit cobaltites “ $\text{Ca}_3\text{Co}_4\text{O}_9$ ,  $(\text{Ca}_2\text{CoO}_3)(\text{CoO}_2)_{1.62}$ ,” made of  $\text{CdI}_2$ -type “ $\text{CoO}_2$ ” layers and rock salt-type “ $\text{Ca}_2\text{CoO}_3$ ” layers.

salt type (second subsystem). Basically, the rock salt layer is formed from  $[\text{CaO}][\text{CoO}][\text{CaO}]$  layers. There is an incommensurate spatial modulation along one of the two in-layer crystal axes, that is, the  $b$ -axis caused by a misfit between the two subsystems. The  $\text{CoO}_2$  sheets, which form a triangular 2D network of edge-sharing  $\text{CoO}_6$  octahedra, are believed to be a conduction plane. From the structural point of view,  $\text{Ca}_3\text{Co}_4\text{O}_9$  is formed with the rock salt-type  $[\text{Ca}_2\text{CoO}_3]$  layer replacing the Na layer in the  $\text{Na}_x\text{CoO}_2$  system, with the typical space group  $C2/m$  and cell parameters  $a \sim 4.8 \text{ \AA}$ ,  $c \sim 10.83 \text{ \AA}$ ,  $\beta \sim 98^\circ$ ,  $b_1 \sim 4.55 \text{ \AA}$ , and  $b_2 \sim 2.82 \text{ \AA}$ . [259]. Two other forms, one of them corresponding to a tripling of the  $c$ -parameters have also been reported [264].

The central structural feature of these materials is the split-site disorder at the rock salt Co and O positions and modulation of the Co and O positions in both layers [265]. A significant displacive modulation on Ca and O atoms of the RS layers in the interlayer bonding scheme was considered, which leads to a noticeable distortion in the  $\text{CoO}_6$  octahedra of the  $[\text{CoO}_2]$  layers [264]. A systematic positional disorder was also noticed inside the  $[\text{CoO}]$  layer.

The X-ray diffraction measurements reveal that the split-site disorder O position in the rock salt layer exhibits oxygen vacancies. The oxygen vacancies responsible for the observed nonstoichiometry have been reported to reside in the central layer of the RS subsystem. As a result, this layer is expected to be responsible for all the flexibility of this compound, whereas the  $\text{CoO}_2$  subsystem is very rigid and responsible for maintaining its structural integrity [268]. X-ray and neutron diffraction studies

suggest a strong *modulation* of the oxygen sites in the  $\text{CoO}_2$  layers and a strong displacive modulation of both cobalt and oxygen sites in the rock salt subsystem [266, 269].

Local structural measurements provide insight into the disorder about Co in the two distinct sites in this system. Co *K*-edge X-ray absorption spectroscopy (XAFS), in combination with DFT calculations, has been carried out to elucidate the local structure of  $\text{Ca}_3\text{Co}_4\text{O}_9$  [270]. This measurement showed that a large static structural distortion and a low cobalt coordination exist in the RS layer compared to the smaller distortion and relatively higher cobalt coordination in the  $\text{CoO}_2$  layer. Cobalt is expected to have a sixfold coordination on both sites. The low cobalt coordination in RS layer comes probably from the oxygen deficiency at the O site for the air-synthesized samples. Atomic resolution Z-contrast image of  $\text{Ca}_3\text{Co}_4\text{O}_9$  showed that the compressed  $\text{CoO}_2$  layers do not exhibit substantial modulations of either the cobalt or the oxygen atomic positions but that the triple RS layers [ $\text{Ca}_2\text{CoO}_3$ ] show a strong buckling of the CoO layers along the *b*-axis [271].

Detailed HREM studies of  $\text{Ca}_3\text{Co}_4\text{O}_9$  [259, 272] have allowed the layered structure of  $\text{Ca}_3\text{Co}_4\text{O}_9$  to be clearly established, identifying the different types of layers.

Though the structure of these incommensurate layered systems with a large unit cell is very complex, detailed atomic-resolution studies have recently been performed. Atomic resolution Z-contrast imaging in conjunction with electron energy loss spectroscopy in an aberration-corrected scanning transmission electron microscope (STEM) have shown the clear local atomic structure in this layered cobaltite [271].

The second class of misfit cobaltites is mainly represented by the bismuth strontium oxide  $[\text{Bi}_{1.7}\text{Sr}_2\text{O}_4][\text{CoO}_2]_{1.82}$ , [252, 254]. The structure of this phase (Figure 1.31), characterized by the symmetry and the lattice constants  $a \sim 4.9 \text{ \AA}$ ,  $b_1 \sim 5.1 \text{ \AA}$ ,  $b_2 \sim 2.8 \text{ \AA}$ ,  $c \sim 29.8 \text{ \AA}$ , and  $\beta \sim 93.45^\circ$ , is also made of single  $[\text{CoO}_2]_\infty$  layers, like other misfit cobaltites. However, between these octahedral layers, the inserted distorted rock salt layers are quadruple, so that these cobaltites are described as the  $n = 4$  misfits. These rock salt layers consist of double “bismuth-oxygen” layers sandwiched between two single SrO layers, replacing the triple  $[\text{Ca}_2\text{CoO}_3]_\infty$  layers in  $\text{Ca}_3\text{Co}_4\text{O}_9$  ( $n = 3$ ) by  $[\text{Bi}_{1.7}\square_{0.3}\text{Sr}_2\text{O}_4]_\infty$  layers ( $n = 4$ ) in this new structural type.

Note that the composition of the RS block modifies the number of free carriers in the  $\text{CoO}_2$  planes and consequently the nominal ratio of  $\text{Co}^{3+}$  to  $\text{Co}^{4+}$  ions. Each octahedron is tilted and compressed with respect to the *c*-axis. The cobaltite  $[\text{Bi}_{1.74}\text{Sr}_2\text{O}_{4-\delta}]^{\text{RS}}[\text{CoO}_2]_{1.82}$  is characterized by two aperiodicities, the first one related to the irrational misfit ratio of the unit cell parameter mismatch between the two sublattices and the second one related to a displacive longitudinal modulation in the BiO layers.

There are numerous possibilities of chemical substitution both in the rock salt layers and in the  $\text{CdI}_2$ -type  $\text{CoO}_2$  layers. Consequently, a large number of homologous series of compounds were investigated both to explore the structural properties and to improve the thermoelectric behavior. The difficulty with substitution in misfit cobaltites is that two different Co sites can be substituted, either in the RS layers or in the  $\text{CoO}_2$  layers. Various substitutions at the level of RS layers have been reported in such types of oxides. In particular, the strontium substitution for calcium in

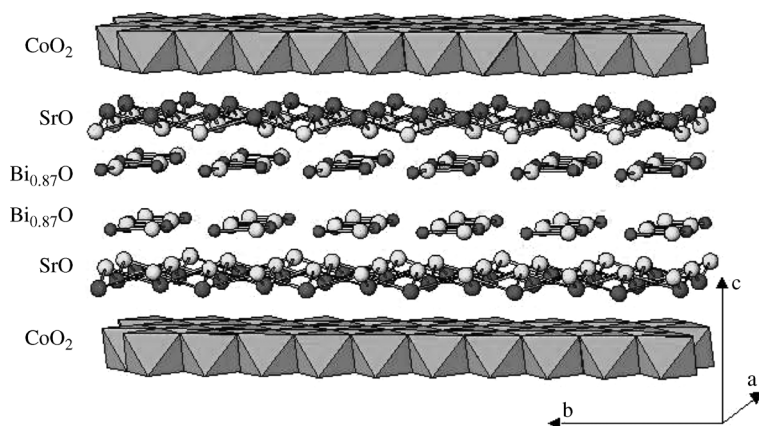


**Figure 1.31** Structure of the misfit cobaltite  $[\text{Bi}_{1.7}\text{Sr}_2\text{O}_4][\text{CoO}_2]_{1.82}$  made of “ $\text{CoO}_2$ ” layers and rock salt-type “ $\text{Bi}_{1.74}\text{Sr}_2\text{O}_4$ ” layers.

$\text{Ca}_3\text{Co}_4\text{O}_9$ , namely,  $[\text{CoCa}_2\text{O}_3]^{\text{RS}}[\text{CoO}_2]_{1.62}$ , has been made [273, 274] and the possibility to introduce partially lead [275, 276], mercury [276, 277], or lanthanides [278] instead of cobalt in the rock salt-type layers has been demonstrated. By this way, a significant enhancement of the room-temperature thermopower has been reported in  $[\text{Pb}_{0.4}\text{Co}_{0.6}\text{Ca}_2\text{O}_3]^{\text{RS}}[\text{CoO}_2]_{1.61}$  with the highest value of  $165 \mu\text{V/K}$  [275].

As already emphasized, the ability of  $\text{Tl}^{3+}$  cations to sit in the rock salt layers of the  $n = 3$  member was demonstrated with the phases of the system  $\text{Tl-Sr-Co-O}$  [250]. The structure consists of the first subsystem, that is, the strontium-deficient rock salt layers  $[(\text{Sr}_{0.9}\square_{0.1})\text{O}]_{\infty}$ , and the second subsystem corresponds to the octahedral  $[\text{CoO}_2]_{\infty}$  layers that exhibit the  $\text{CdI}_2$  structure. The thallium atoms are located between the two kinds of layers, with a distorted tetrahedral coordination, ensuring the cohesion of the structure. The combined electron and X-ray diffraction studies give the lattice constants of the system  $a \sim 4.9 \text{ \AA}$ ,  $b_1 \sim 5.0 \text{ \AA}$ ,  $b_2 \sim 2.8 \text{ \AA}$ ,  $c \sim 11.6 \text{ \AA}$ , and  $\beta \sim 97.7^\circ$ .

Similar to the misfit structure of  $\text{Ca}_3\text{Co}_4\text{O}_9$ , the perfectly homogeneous  $n = 3$  misfit cobaltites,  $[\text{Pb}_{0.7}\text{Sr}_{1.9}\text{Co}_{0.4}\text{O}_3][\text{CoO}_2]_{1.8}$  and  $[\text{Pb}_{0.7}\text{Hg}_{0.2}\text{Sr}_{1.9}\text{Co}_{0.2}\text{O}_3][\text{CoO}_2]_{1.8}$ , consisting of regular stacking of  $\text{CdI}_2$ -type  $[\text{CoO}_2]$  layers stacked with triple rock salt-type layers have been synthesized and identified by HREM [276]. This study shows the great flexibility of the rock salt layer in the misfit cobaltites, which is able to accommodate various cations such as mercury, lead, cobalt, and strontium distributed at random. The substitution can be made in either sublattice, modifying the lattice parameters and consequently the aperiodic ratio  $p$  [274, 279]. There is also a large number of  $n = 4$  misfit cobaltites, corresponding to the substitution of various cations such as Ba, Ca, Cu, and Pb for strontium in the RS layers of the matrix of  $[\text{Bi}_{1.7}\text{Sr}_2\text{O}_4]_{1.82}\text{CoO}_2$  as exemplified for  $(\text{Bi}_2, \text{Ba}_{1.8}, \text{Co}_{0.2}\text{O}_4)(\text{CoO}_2)$  [255]. Note that the Pb for Bi substitution has a strong impact on the structural properties as it completely suppresses the BiO modulation [280]. However, this misfit ratio may be different from 1.82 depending on the oxygen content, as it has been observed in  $[\text{Ca}_2\text{CoO}_3][\text{CoO}_2]_{1.62}$  [281, 282].

**Table 1.1** List of misfit layered cobaltites with three or four interleaved rock salt layers.

Compositions	$p = b_{RS}/b_{CoO_2}$	$n$ (no of rock salt layers)	References
$[Ca_2Co_{0.6}Pb_{0.4}O_3]^{RS}[CoO_2]_p$	1.61	3	[275]
$[Ca_2CoO_3]^{RS}[CoO_2]_p$	1.62	3	[259]
$[Ca_{1.7}Nd_{0.3}CoO_3]^{RS}[CoO_2]_p$	1.62	3	[268]
$[Sr_2CoO_3]^{RS}[CoO_2]_p$	1.8	3	[283]
$[Ti_{0.8}Co_{0.2}Sr_2O_3]^{RS}[CoO_2]_p$	1.8	3	[256, 277]
$[Pb_{0.7}Co_{0.3}Sr_2O_3]^{RS}[CoO_2]_p$	1.8	3	[276, 277]
$[Hg_{1-x}Co_xSr_2O_3]^{RS}[CoO_2]_p$	1.8	3	[276, 277]
$[Ca_2(Co_{0.65}Cu_{0.35})_2O_4]^{RS}[CoO_2]_p$	1.60	4	[284]
$[Bi_{1.7}Co_{0.3}Ca_2O_4]^{RS}[CoO_2]_p$	1.67	4	[285]
$[Bi_{1.74}Sr_2O_4]^{RS}[CoO_2]_p$	1.82	4	[286]
$[Bi_2Ba_{1.8}Co_{0.2}O_4]^{RS}[CoO_2]_p$	2.0	4	[255]

All these compounds are reported to exhibit interesting physical properties [254, 255, 280, 285]. Table 1.1 contains the composition of a few compounds with different interleaved RS layers ( $n$ ). The composition  $[Ca_2(Co_{0.65}Cu_{0.35})_2O_4][CoO_2]_{1.60}$  with  $n = 4$  exhibits a distinctive feature: it presents two intermediate sheets containing transition metal, sandwiched in between two  $[CaO]_{\infty}$  sheets [284].

Substitutions in the rock salt layer do not modify the structure of the  $[CaO]$  or the  $[CoO_2]$  layers, only the versatile  $[CoO]$  layer is slightly modified to accept the new type of atom [269]. For the substitution of  $Nd^{3+}$  for  $Ca^{2+}$  in  $Ca_3Co_4O_9$ , it has been observed that the RS layer is more affected than the hexagonal layer and the oxygen vacancies are located mainly in the RS layer [268]. For the doubly substituted  $Ca_{3-x-y}Gd_xY_yCo_4O_{9+d}$ , all the lattice parameters of the samples are slightly decreased, while  $\beta$  does not change significantly [287]. The 4S-type doubly substituted compounds  $[Ca_{2-y}Ln_yCu_{0.7+y}Co_{1.3-y}O_4]^{RS}[CoO_2]_p$  ( $Ln = Pr$  and  $Y$ ) show double modulations, one of which is the misfit between the two subsystems and the other is intrinsic to the rock salt layer, as determined by the ED and HERM studies [288].

The substitutions with transition elements are more difficult to investigate due to the fact that the transition element has the possibility to sit also in the  $CoO_2$  layers. Two  $n = 3$  and 4 misfit compounds,  $[Ti_{0.4}Co_{0.6}Ca_2O_3][CoO_2]_{1.62}$  [289] and  $[Ca_2(Co_{0.65}Cu_{0.35})_2O_4][CoO_2]_{1.60}$  [290], were synthesized with all copper and titanium sitting in the RS-type layer. Substitutions with transition metal elements in the  $Ca_3Co_4O_9$ -type structure have also been carried out for Ti, Mn, and Fe [268, 291, 292]. It has been proposed that the substitution occurs either in the  $CoO_2$  subsystem based on consideration of ionic radii [293] or in the RS subsystem based on changes in magnetic and transport properties [294]. Transmission electron microscopy and X-ray powder diffraction studies reveal that the substitution of Rh for Co takes place at the two cobalt sites of the structure but for low enough Rh contents, this substitution is made preferentially at the level of the  $CdI_2$ -like layer [295]. The stacking of the layers along the  $c$ -axis in the misfit layered oxides strongly depends both on the cationic composition and on the thermal process due to the possible mixed valence of the transition cations [250–253].

## 1.8.4

Intergrowth of Hexagonal Perovskite and  $\text{CdI}_2$ -Type Layers

The topology of the “hexagonal perovskite”  $\text{BaCoO}_{3-x}$  structure described in Section 1.6 is closely related to that of the  $\text{CoO}_2$  layers of the  $\text{Na}_x\text{CoO}_2$  structure. Both structures exhibit a similar hexagonal lattice with  $a \sim 5.6 \text{ \AA}$  for the  $\text{BaCoO}_{3-x}$  and  $a \sim 2.8 \text{ \AA}$  for  $\text{Na}_x\text{CoO}_2$ . As a consequence, these two structures can form intergrowths, where the octahedral units of face sharing octahedra of the hexagonal perovskites ensure the connection between the  $[\text{CoO}_2]_\infty$  layers of the  $\text{Na}_x\text{CoO}_2$ -type structure. This mechanism appears in the cobalt-rich barium cobaltites, as exemplified by the oxide  $\text{Ba}_2\text{Co}_9\text{O}_{14}$ , which is rhombohedral  $R\bar{3}m$  with  $a \sim 5.7 \text{ \AA}$  and  $c \sim 28.9 \text{ \AA}$ , and  $\text{Ba}_3\text{Co}_{10}\text{O}_{17}$  that is also rhombohedral but with different lattice constants  $a \sim 5.7 \text{ \AA}$  and  $c \sim 35.9 \text{ \AA}$  [296]. The structure of these hexagonal perovskite  $\text{CdI}_2$ -type intergrowths can be represented as  $\text{Ba}_{n+1}\text{Co}_n\text{O}_{3n+3}\text{Co}_8\text{O}_8$ , where the  $n = 1$  and 2 numbers correspond to the former and latter compositions, respectively. Figure 1.32 shows the structure of  $\text{Ba}_2\text{Co}_9\text{O}_{14}$  and  $\text{Ba}_3\text{Co}_{10}\text{O}_{17}$ . The structure of  $\text{Ba}_2\text{Co}_9\text{O}_{14}$  (Figure 1.32) consists indeed of hexagonal  $[\text{CoO}_2]_\infty$  layers similar to those of  $\text{Na}_x\text{CoO}_2$ , that is, made of edge-sharing  $\text{CoO}_6$  octahedra with the  $\text{CdI}_2$ -type arrangement. These  $[\text{CoO}_2]_\infty$  layers are interconnected through trimeric units of

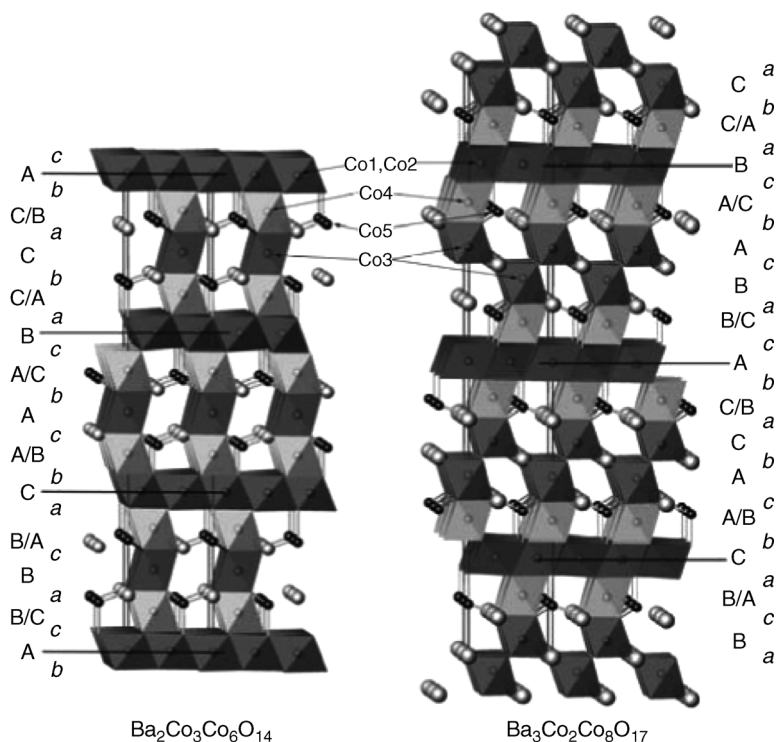
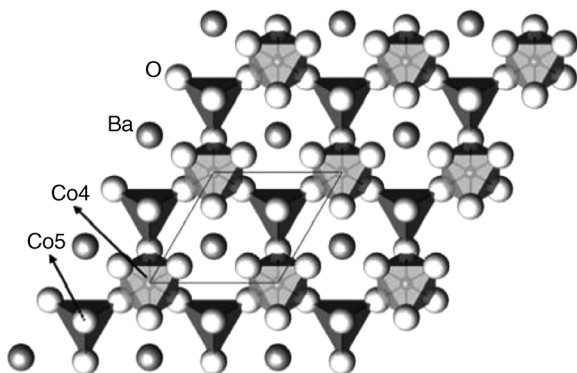


Figure 1.32 The crystal structure of  $\text{Ba}_2\text{Co}_9\text{O}_{14}$  and  $\text{Ba}_3\text{Co}_{10}\text{O}_{17}$ . Adapted from Ref. [296].



**Figure 1.33** Interface layer in both  $\text{Ba}_2\text{Co}_9\text{O}_{14}$  and  $\text{Ba}_3\text{Co}_{10}\text{O}_{17}$  consisting of close packed  $[\text{BaO}_3]$  and  $[\text{O}_4]$  oxygen layers. The octahedral and tetrahedral sites are occupied by cobalt ions, which are shown as polyhedra; barium and oxygen atoms are expressed as dark and light balls.

face-sharing  $\text{CoO}_6$  octahedra that have the same arrangement as in the hexagonal perovskites. In other words, hexagonal-type perovskite layers are stacked with  $[\text{CoO}_2]_\infty$  layers. Nevertheless, it must be emphasized that additional  $\text{CoO}_4$  tetrahedra are located in the hexagonal perovskite layers at the border with the  $[\text{CoO}_2]_\infty$  layers. The structure of  $\text{Ba}_3\text{Co}_{10}\text{O}_{17}$  (Figure 1.32) shows a more complicated stacking where the  $[\text{CoO}_2]_\infty$  layers are intergrown with double hexagonal perovskite layers made of units of two face-sharing octahedra as in the 2H structure, but containing  $\text{CoO}_4$  tetrahedra at the border with the  $\text{CoO}_2$  layers. Thus, in these structures, there are two types of polyhedral sites, that is, octahedral and tetrahedral sites, occupied by cobalt ions. The structures can also be regarded as close packed layers, either  $[\text{BaO}_3]$  or  $[\text{O}_4]$  with cobalt occupying octahedral interstitial sites. The interface layer contains a close packed oxygen layer and a  $[\text{BaO}_3]$  layer as shown in Figure 1.33. The close packed layers  $[\text{BaO}_3]$  lead to  $n$  perovskite layers, whereas the  $[\text{O}_4]$  layers lead to the  $\text{CdI}_2$  structure. The structures are complicated with additional cobalt occupying the tetrahedral sites at the interface between these two structure types.

From these investigations, it appears that many other members should be generated by varying the Ba:Co:O ratio in this system and that other closely related cobaltites should be generated in the future, by introducing besides barium smaller cations like  $\text{Sr}^{2+}$ ,  $\text{Ca}^{2+}$ , or  $\text{Ln}^{3+}$ .

### 1.8.5

#### Kagomé “114” Cobaltites: $\text{LnBaCo}_4\text{O}_{7+\delta}$ and $\text{CaBaCo}_4\text{O}_{7+\delta}$

Discovered by Mueller-Buschbaum for the oxide  $\text{LnBaZn}_3\text{AlO}_7$  [297], the “114” hexagonal structure has been reported for a series of cobaltites  $\text{LnBaCo}_4\text{O}_7$  with  $\text{Ln} = \text{Tb}, \text{Dy}, \text{Ho}, \text{Er}, \text{Tm}, \text{Yb}, \text{Lu}, \text{and Y}$  [298–303]. These cobaltites belong to a class of geometrically frustrated magnets that are also studied by many authors for their magnetic, electronic, and thermoelectric properties.

These oxides exhibit a structural transition at a  $T_s$  temperature ranging from 160 to  $\sim 360$  K, as the size of  $\text{Ln}^{3+}$  increases from  $\text{Lu}^{3+}$  to  $\text{Ho}^{3+}$ . The high-temperature (HT) form is hexagonal, whereas the low-temperature form (LT) exhibits an orthorhombic distortion of the latter. Note that the yttrium phase is found to be orthorhombic at room temperature by some authors [304], with  $T_s \sim 350$  K, whereas other authors find it hexagonal [298]. This divergence may be due to problem of oxygen nonstoichiometry that will be discussed further.

At room temperature, most of the  $\text{LnBaCo}_4\text{O}_7$  cobaltites, exhibit an hexagonal lattice with  $a \sim 6.3$  Å and  $c \sim 10.25$  Å. There is still an ambiguity about the space group of this phase that can be either hexagonal  $P6_3mc$  [305] or trigonal  $P31c$  [306]. But this divergence does not affect significantly the description of the structure even if it is important for the study of the physical properties. This structure (Figure 1.34) can be described as a close packed “ $\text{BaO}_7$ ” framework, with a 4H (abac) stacking of the Ba and O atoms (Figure 1.34a–b): one-eighth oxygen atom is replaced by Ba so that this framework consists of a close packing of “ $\text{BaO}_3$ ” and “ $\text{O}_4$ ” layers. In this hexagonal close packing, the tetrahedral cavities are occupied by cobalt ions. As a result, this structure can also be described as a pure tetrahedral framework (Figure 1.34c–d) in which the  $\text{CoO}_4$  tetrahedra form two sorts of layers, triangular layers (T) (Figure 1.34f) and kagomé layers (K) (Figure 1.34e), stacked along  $\vec{c}$  alternately, whereas the  $\text{Ln}^{3+}$  cations sit in the octahedral sites. In the  $P6_3mc$  lattice [307], there are two symmetry-independent  $\text{CoO}_4$  tetrahedra with a ratio of 1 : 3 present in this hexagonal structure (Figure 1.34). The Co1 and Co2 species are distributed between the two types of alternating layers of vertex-sharing  $\text{CoO}_4$  tetrahedra forming magnetically frustrated trigonal nets and kagomé nets. The Co2 sites form the kagomé sheets. The Co1 sites with trigonal nets are linked to the kagomé nets along the  $c$ -axis. The separation between these layers is about 2 Å. The two kinds of tetrahedra are distinguished by different sets of bond lengths and located in separate layers that alternate with each other [306, 308].

As stated above, there is some divergence about the exact symmetry of the HT form of the  $\text{LnBaCo}_4\text{O}_7$  family. This has been shown for  $\text{YbBaCo}_4\text{O}_7$  [298, 300, 304]. The high-resolution powder neutron and synchrotron X-ray diffraction studies have revealed that the space group of  $\text{YbBaCo}_4\text{O}_7$  is  $P31c$  rather than the  $P6_3mc$  at room temperature and it changes from  $P31c$  to  $Pbn2_1$  below 175 K. The transition occurs as a response to a strongly underbonded  $\text{Ba}^{2+}$  ion and no convincing evidence of charge ordering on the cobalt ions was expected using bond valence sums calculation. The severely underbonded barium cation, which exhibits a computed charge of 1.33 according to BVS calculations, defies the structural stability and argues against stabilizing this structure with smaller divalent cations on the  $\text{Ba}^{2+}$  site [306].

The LT form obtained by cooling the samples below room temperature reveals an orthorhombic symmetry, corresponding to the space group  $Pbn2_1$ , with  $a \sim a_H$   $\sim 6.30$  Å,  $b \sim a_H/\sqrt{3} \sim 10.90$  Å, and  $c \sim c_H \sim 10.23$  Å. The transition temperature  $T_s$  decreases practically linearly with the size of the  $\text{Ln}^{3+}$  cation from 313 K for  $\text{Ho}^{3+}$  to 170 K for  $\text{Lu}^{3+}$  [305].

The nature of this first-order phase transition has been studied in detail by neutron diffraction for the oxide  $\text{TmBaCo}_4\text{O}_7$  [309] showing that the symmetry lowering from

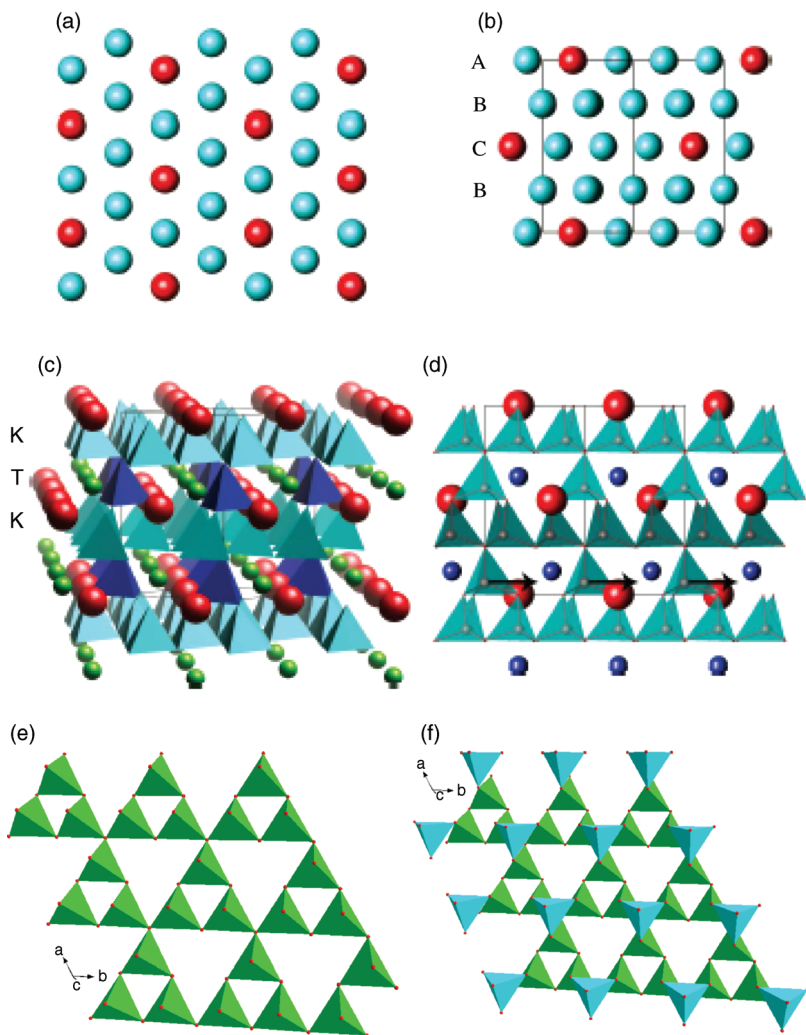


**Figure 1.34** Trigonal structure of  $\text{LnBaCo}_4\text{O}_7$  and  $\text{CaBaFe}_4\text{O}_7$ : (a) hexagonal close packed “ $\text{BaO}_3$ ” layer parallel to (001), (b) hexagonal “ABCB” (hchc) close packing of “ $\text{BaO}_3$ ” and “ $\text{O}_4$ ” layers, (c) perspective view for the trigonal structure nearly along  $\langle 1-10 \rangle_H$  showing the alternate stacking of the kagomé (K) and

triangular layers (T) of  $\text{CoO}_4$  (or  $\text{FeO}_4$ ) tetrahedra, (d) view of structure along  $\langle 1-10 \rangle_H$  showing large distorted tunnels running along this direction, (e) kagomé layer K, and (f) relative positions of the triangular layers T with respect to the K layers.

$P31$  to  $Pna2_1$  symmetry is due to a displacive phase transition, involving a complex tilting of  $\text{CoO}_4$  tetrahedra, which are not allowed to rotate as rigid polyhedra.

The discovery of the ferrimagnetic “114” cobaltite  $\text{CaBaCo}_4\text{O}_7$  [310, 311] sheds light on the nature of the orthorhombic form observed at low temperature for all the series  $\text{LnBaCo}_4\text{O}_7$ . This oxide crystallizes in the orthorhombic  $Pbn2_1$  symmetry but

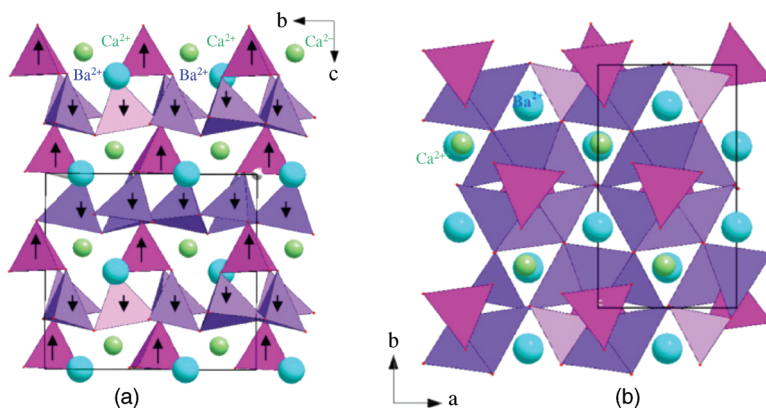


**Figure 1.35** Structure of  $\text{CaBaCo}_4\text{O}_7$ , showing the buckling of the kagomé layers: (a) view along  $a$ ; (b) view along  $c$ . Adapted from Ref. [310, 311].

with a much higher orthorhombic distortion, corresponding to the lattice constants  $a \sim 6.288 \text{ \AA}$ ,  $b \sim 11.007 \text{ \AA}$ , and  $c \sim 10.195 \text{ \AA}$ . Also, the orthorhombic symmetry of this phase is stable whatever the temperature, comprised between 4 and 400 K, that is, no transition to the hexagonal phase can be observed by increasing the temperature. Like, the hexagonal  $\text{LnBaCo}_4\text{O}_7$  cobaltites, the structure of  $\text{CaBaCo}_4\text{O}_7$  (Figure 1.35) consists of an ordered 1 : 1 stacking of  $[\text{BaO}_3]_\infty$  and  $[\text{O}_4]_\infty$  close packed layers, whose tetrahedral cavities are occupied by cobalt ions, whereas  $\text{Ca}^{2+}$  cations sit in the octahedral cavities. Thus, the  $[\text{Co}_4\text{O}_7]_\infty$  framework consists of a 1 : 1 stacking of kagome and triangular layers of  $\text{CoO}_4$  tetrahedra. Quite remarkably, the structure of  $\text{CaBaCo}_4\text{O}_7$  differs from the “114” hexagonal structure of cobaltites by a very strong buckling of the  $\text{CoO}_4$  tetrahedra of the kagome layers. In contrast, the  $\text{CoO}_4$  tetrahedra remain rather regular with  $\text{Co}-\text{O}$  distances ranging from 1.80 to 2.09  $\text{\AA}$ . The  $\text{CaO}_6$  octahedra are also regular with  $\text{Ca}-\text{O}$  distances comprised between 2.16 and 2.46  $\text{\AA}$  [310]. It will be shown in the next section that this distortion has a very important impact upon the appearance of ferrimagnetism in this phase. Importantly, the BVS calculations show that  $\text{CaBaCo}_4\text{O}_7$  exhibits charge ordering in the cobalt sites: the  $\text{Co}^{2+}$  cations sit on two sites, Co2 and Co3, belonging to the kagomé layers, whereas the mixed valent  $\text{Co}^{3+}/\text{Co}^{2+}$  species sit on two other sites, Co1 and Co4, belonging to the triangular and kagomé layers, respectively [311].

One important feature of the “114” cobaltites is their ability to accommodate oxygen excess, in spite of the close packed character of the structure, whatever its symmetry, hexagonal or orthorhombic. It was shown that  $\text{LnBaCo}_4\text{O}_{7+\delta}$  ( $\text{Ln} = \text{Tb}, \text{Dy}, \text{Ho}, \text{Er}, \text{Tm}, \text{Yb}, \text{and Y}$ ) cobaltites can absorb and desorb up to  $\delta = 1.50$  oxygen atom per formula [312, 313], in a very narrow range of temperature, 200–400  $^\circ\text{C}$ . The oxygen uptake or release process is highly reversible, being controlled by both temperature and oxygen partial pressure [312, 313]. The oxygen absorption and desorption are very sensitive to the rare-earth size (Figure 1.36) [312].

Note that the hump in the lower temperature region of 200–400  $^\circ\text{C}$  reflects the unique ability of the  $\text{LnBaCo}_4\text{O}_{7+\delta}$  compounds to absorb and then desorb large

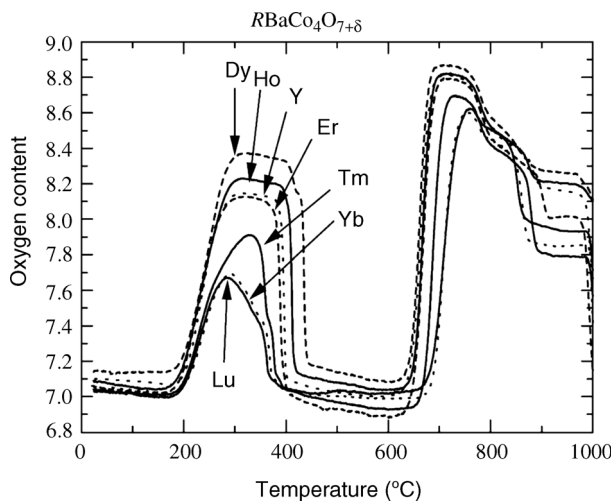


**Figure 1.36** TG curves for as-synthesized  $\text{LnBaCo}_4\text{O}_{7+\delta}$  samples ( $0.03 \leq \delta \leq 0.14$ ) recorded in  $\text{O}_2$  gas flow with a heating rate of  $1^\circ\text{C}/\text{min}$ . The two humps at about  $200\text{--}400^\circ\text{C}$  and above  $600^\circ\text{C}$  are due to oxygen absorption/desorption and phase decomposition, respectively. Adapted from Ref. [312].

amounts of oxygen in a narrow temperature range, whereas the one in the high-temperature region above  $600^\circ\text{C}$  is due to the phase decomposition of  $\text{LnBaCo}_4\text{O}_{7+\delta}$  to  $\text{BaCoO}_{3-\delta}$ . Upon decrease in the ionic radius  $r_{\text{Ln}^{3+}}$ , the oxygen release temperature  $T_{\text{R}}$  decreases, while the phase decomposition temperature  $T_{\text{D}}$  increases such that the safety window,  $T_{\text{R}}\text{--}T_{\text{D}}$ , widens. However, at the same time the maximum amount of excess oxygen chargeable into the  $\text{LnBaCo}_4\text{O}_{7+\delta}$  lattice in 1 atm  $\text{O}_2$  decreases as the size of  $\text{Ln}^{3+}$  becomes smaller. The oxygen storage characteristics for the  $\text{LnBaCo}_4\text{O}_{7+\delta}$  system may be optimized about  $\text{Ln} = \text{Tm}$ . Consequently, these oxides are found to exhibit a great chemical flexibility.

The crystallographic nature of the “oxygen hyperstoichiometric” samples is still a matter of debate. For instance, in  $\text{YBaCo}_4\text{O}_{7+\delta}$  cobaltite, the sample with  $\delta = 1.25$  was still found to be hexagonal  $P6_3mc$  [313] suggesting that the crystal structure was essentially the same as for “ $\text{O}_7$ ”, though the broadening of the XRPD peaks may indicate a possible change in the symmetry, but no real crystal determination was performed. The presence of an oxygen excess in the hexagonal compounds  $\text{LnBaCo}_4\text{O}_{7+\delta}$  was observed from chemical measurements by several authors, but the presence of this extra oxygen in the hexagonal  $P6_3mc$  structure could not be detected, even from neutron diffraction studies. Thus, the location of the extra oxygen in hyperstoichiometric samples, observed from chemical measurements in hexagonal  $P6_3mc$  or even orthorhombic  $Pbn2_1$  “114” cobaltites [306, 313–316] remains to date an open issue since nobody has been able to prove its presence in the structure. Bearing in mind that, the hexagonal  $P6_3mc$  structure is a close packed structure, the insertion of additional oxygen in this framework is not likely. In contrast, the close relationships between this “114” hexagonal structure and that of the cubic spinel

$\text{Fe}_3\text{O}_4$  suggest that a topotactic oxidation of these cobaltites could take place in a similar way to the oxidation of  $\text{Fe}_3\text{O}_4$  into the  $\gamma\text{-Fe}_2\text{O}_3$  cationic-deficient spinel. Such a model would explain, at least for low  $\delta$ -values ( $\delta \leq 0.1$ ), the different physical properties of the oxygen hyperstoichiometric  $\text{LnBaCo}_4\text{O}_{7+\delta}$  cobaltites, that is,  $(\text{LnBaCo}_4)_{7/7+\delta}\text{O}_7$ , with respect to the stoichiometric  $\text{LnBaCo}_4\text{O}_7$  oxides, though the structure is the same and cannot be differentiated even from neutron diffraction measurements.

In any case, the structure of the  $\text{LnBaCo}_4\text{O}_7$  oxides is flexible, and it can also be modified topotactically by a large oxygen excess, inducing significant distortions of the initial hexagonal framework, which can be detected from structure determination. This is the case of  $\text{YBaCo}_4\text{O}_{8.2}$  first observed with an erroneous space group [317] and which was then shown to exhibit an orthorhombic structure  $Pbc2_1$ , with  $a \sim 12.79 \text{ \AA}$ ,  $b \sim 10.84 \text{ \AA}$ , and  $c \sim 10.15 \text{ \AA}$  [318], closely related to that of  $\text{YBaCo}_4\text{O}_7$ .

Some possible models have been proposed to know where extra oxygen atoms might be accommodated [301, 318]. Valldor [298] recognized three possible positions where the extra oxygen atoms might be incorporated in the  $\text{YBaCo}_4\text{O}_7$  structure. One of these sites is just under the kagomé  $\text{Co}(2)$  triangles and the remaining two sites are at the center of the Ba anticuboctahedra's square faces. Based on the synchrotron X-ray and neutron powder diffraction studies with  $\delta \approx 1.1$  sample, Chmaissem *et al.* [318] have shown that the additional oxygen atoms are ordered in a doubled superstructure unit cell, where considerable displacements of several of the original oxygen atoms take place.  $\text{YBaCo}_4\text{O}_{8.2}$  forms a large orthorhombic superstructure with respect to its parent  $\text{YBaCo}_4\text{O}_7$  phase [318]. Figure 1.37 shows a [010] projection of the structure in which the increased lattice distortions clearly result in significantly corrugated layers. This figure and the alternating octahedral/tetrahedral zigzag patterns demonstrate the origin of the  $a$ -axis superlattice doubling. In the triangular lattice of  $\text{YBaCo}_4\text{O}_{8.2}$ , the extra oxygen atoms enter the structure to bond with half the triangular cobalt ions and form zigzag patterns of Co1 octahedra (Figure 1.38). The

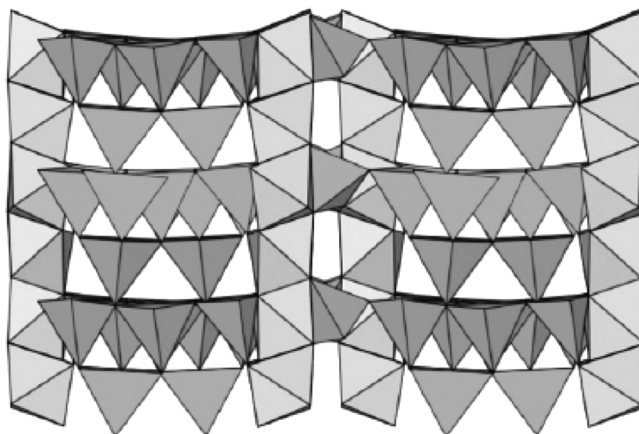


**Figure 1.37** Projection of the  $\text{YBaCo}_4\text{O}_8$  structure along the [010] direction showing the material's structural distortions and corrugated layers. Adapted from Ref. [318].

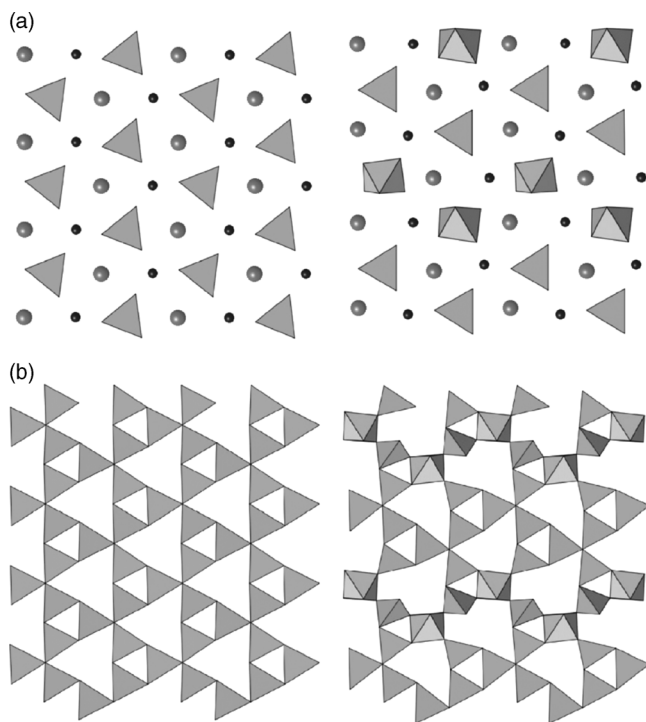


**Figure 1.38** Side-by-side views of the triangular (a) and Kagome (b) layers for YBaCo<sub>4</sub>O<sub>7</sub> (left) and YBaCo<sub>4</sub>O<sub>8</sub> (right). Large and small circles represent Ba and Y ions, respectively. Adapted from Ref. [318].

octahedra and remaining tetrahedra form alternating zigzag patterns that run parallel to each other along the *b*-axis. In the kagomé layer, Co2 octahedra form directly above and below the Co1-octahedra zigzag ribbons directed along the *c*-axis. The formation of such zigzag chains of edge-sharing octahedra is extremely rare in the metal oxides system.

Some of the tetrahedral Co<sup>3+</sup>–O bond lengths are found to be significantly short (1.75–1.78 Å) compared to their tetrahedral Co<sup>2+</sup>–O counterparts (1.87–2.02 Å). It is important to note here that the tetrahedral coordination for Co<sup>3+</sup> is rare, and when found, the Co<sup>3+</sup>–O bond lengths have been reported to be on the order of 1.78–1.79 Å. This instability of tetrahedral Co<sup>3+</sup> in the parent “O<sub>7</sub>” material may drive the strong affinity for oxygen uptake [318].

The excess oxygen atoms form several types of ordering, resulting in different structural modulations, probably with various excess oxygen contents, and leading to changes in unit cell size [319].

In contrast to the Na<sub>*x*</sub>CoO<sub>2</sub> oxides and misfit cobaltites, which are characterized by the mixed valence Co<sup>3+</sup>/Co<sup>4+</sup>, the “114” cobaltites exhibit the mixed valence Co<sup>2+</sup>/Co<sup>3+</sup>. The Co<sup>2+</sup>/Co<sup>3+</sup> ratios are very different in the LnBaCo<sub>3</sub><sup>2+</sup>Co<sup>3+</sup>O<sub>7</sub> and in the CaBaCo<sub>2</sub><sup>2+</sup>Co<sup>3+</sup>O<sub>7</sub> cobaltites. In the LnBaCo<sub>4</sub>O<sub>7</sub> series, there is a lot of

controversy regarding the charge ordering of cobalt. For example, the structural transition in  $\text{LnBaCo}_4\text{O}_7$  ( $\text{Ln} = \text{Lu}, \text{Yb}, \text{and Tm}$ ) was ascribed to the charge ordering of  $\text{Co}^{2+}$  and  $\text{Co}^{3+}$  at the kagomé and triangular sites, respectively [307]. On the other hand, there is no clear evidence of charge ordering either at room temperature or at low temperature [298]. Very similar results disagreeing with the charge ordering are also reported for the Yb phase [306]. A Mossbauer study suggested no signature of charge ordering in  $\text{YBaCo}_4\text{O}_{7+\delta}$  with  $\delta = 0.02$  and  $0.80$  [320]. In the Ni-doped  $\text{YBaCo}_4\text{O}_7$  system, it was observed that the structural transition point shifts to lower temperature with the substitution and that there is no evidence of charge ordering [321]. This is in contrast to  $\text{CaBaCo}_4\text{O}_7$ , for which charge ordering has clearly been seen whatever the temperature [311].

In the oxygen hyperstoichiometric cobaltites, the cobalt valence increases from  $+2.25$  in  $\text{LnBaCo}_4\text{O}_7$  to  $+2.75$  in  $\text{LnBaCo}_4\text{O}_8$ , reaching  $+3$  in  $\text{LnBaCo}_4\text{O}_{8.5}$ . The oxygen K-edge and cobalt L-edge XANES spectra of  $\text{YBaCo}_4\text{O}_7$  and  $\text{YBaCo}_4\text{O}_{8.2}$  [317] show that the local structure is more complex in  $\text{YBaCo}_4\text{O}_{8.2}$  than in  $\text{YBaCo}_4\text{O}_7$ , that is, the oxygen absorption increases the number of different crystallographic sites for O and Co atoms and the structure becomes more complicated in terms of Co–O coordination.

### 1.8.6

#### Unidimensional Cobaltite $\text{Ca}_3\text{Co}_2\text{O}_6$

In contrast to the bidimensional structures, which are easily synthesized for Sr-rich cobaltites, such as the RP family, or for  $\text{Na}_x\text{CoO}_2$  and for the misfit cobaltites, containing various cations such as  $\text{Ca}^{2+}$ ,  $\text{Sr}^{2+}$ ,  $\text{Ba}^{2+}$ ,  $\text{Tl}^{3+}$ ,  $\text{Bi}^{3+}$ , and  $\text{Pb}^{2+}$ , the stabilization of a cobaltite with an unidimensional structure is not trivial.  $\text{Ca}_3\text{Co}_2\text{O}_6$  is, to our knowledge, the only example of trivalent cobaltite that exhibits a quasi-unidimensional structure [322–324]. Such an oxide is of great interest due to its highly anisotropic and unique physical properties.

This oxide crystallizes in the space group  $R\bar{3}c$ , with the lattice parameters  $a \sim 9.08 \text{ \AA}$  and  $c \sim 10.38 \text{ \AA}$  at room temperature [323]. Its structure (Figure 1.39a) consists of linear chains  $[\text{CoO}_2]_\infty$  of face-sharing  $\text{CoO}_6$  octahedra (Co1) and  $\text{CoO}_6$  triangular prisms (Co2) running along  $\vec{c}$ . The first unique character of this 1D structure is that one  $\text{CoO}_6$  octahedron alternates with one  $\text{CoO}_6$  trigonal prism along  $\vec{c}$ , with an exceptionally short Co–Co distance of  $2.59 \text{ \AA}$  within the chain, due to the fact that the two successive polyhedra share one face. The  $\text{Ca}^{2+}$  cations are located between the  $[\text{Co}_2\text{O}_6]_\infty$  chains, with an eightfold coordination, ensuring the cohesion of this unidimensional structure. The second important character of this structure is that each chain is surrounded by six similar chains located at a distance of  $5.24 \text{ \AA}$  (Figure 1.39b), forming a triangular arrangement, so that the interchain Co–Co distance ( $5.2 \text{ \AA}$ ) is much higher than the intrachain Co–Co distance ( $2.59 \text{ \AA}$ ). This anisotropy is of capital importance for the magnetic properties of this compound, as will be further discussed in the section. From their different coordinations, the two kinds of cobalt ions manifest different Co–O distances: the Co–O distances of the Co1 octahedra are indeed significantly smaller than those of the Co2 prisms, that is,

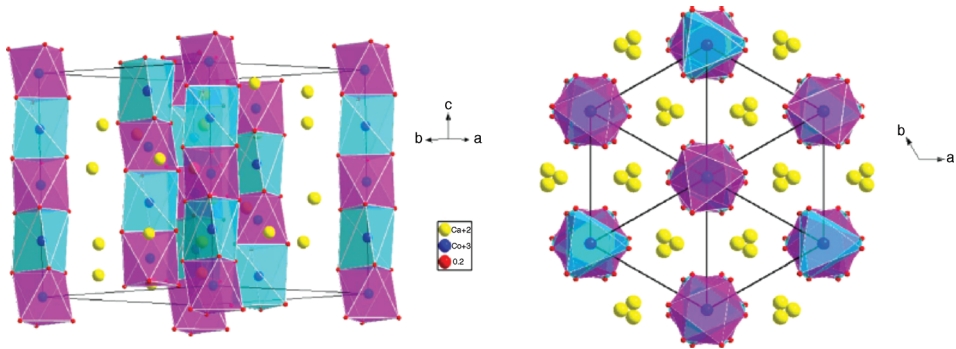


**Figure 1.39** Crystal structure of  $\text{Ca}_3\text{Co}_2\text{O}_6$ : a perspective view showing the chains of  $\text{CoO}_6$  trigonal prisms and  $\text{CoO}_6$  octahedra running along the hexagonal  $c$ -axis (left) and a

projection along the  $c$ -axis (right). The calcium cations are shown as small circles located between the chains. Adapted from Ref. [332].

of 1.91 and 2.06 Å, respectively. This size difference has suggested a possible charge disproportionation in  $\text{Ca}_3\text{Co}_2^{\text{III}}\text{O}_6$  of  $\text{Co}^{3+}$  into  $\text{Co}^{4+}$  and  $\text{Co}^{2+}$ . However, the X-ray absorption study of this phase at the  $L_{2,3}$  edge of cobalt has definitely shown that cobalt exhibits only the trivalent state [325]. Thus, the different size of Co1 and Co2 originates from a different spin configuration of cobalt as will be discussed in the section.

Finally, it must be emphasized that  $\text{Ca}^{2+}$  can be replaced by  $\text{Sr}^{2+}$  in the  $\text{Ca}_3\text{Co}_2\text{O}_6$ -type structure, but this requires a partial substitution of larger cations for cobalt. This has been observed for the 1D cobalt oxides  $\text{Sr}_3\text{CoPtO}_6$  [326] and  $\text{Sr}_3\text{CoIrO}_6$  [327]. In fact, in the case of strontium cobaltites, the 1D structure is in competition with the RP structure already described for  $\text{Sr}_3\text{Co}_2\text{O}_{6+\delta}$ , so that oxides such as  $\text{Sr}_3\text{ScCoO}_6$  [328],  $\text{Sr}_3\text{FeCoO}_7$  [329], and  $\text{Sr}_3\text{NiCoO}_6$  [330] crystallize in the RP structure. It was shown that the stability of the 1D structure of  $\text{A}_{n+2}\text{B}_{n+1}\text{O}_{3n+3}$  oxides depends on the  $r_A/r_B$  ratio and that the interchain distances should be decreased in order to improve the stability of that structure [331]. Consequently, in the present cobaltites, that is, for  $\text{A} = \text{Sr}, \text{Ca}$  and  $\text{B} = \text{Co}, \text{M}$  with  $n = 1$ , the  $r_A/r_B$  should be decreased in order to stabilize the 1D structure with respect to the RP structure.

## 1.9

### Some Other Original Cobaltites

Besides the above cobaltites that have been thoroughly studied for their attractive magnetic or transport properties, there exist several other cobalt oxides, whose structure is attractive and may be of interest for future physical investigations. We describe here the structures of the trivalent cobaltites  $\text{CaCo}_2\text{O}_4$ ,  $\text{Ba}_6\text{La}_2\text{Co}_4\text{O}_{15}$ , and  $\text{RbCoO}_2$  of the divalent cobaltites  $\text{BaCoO}_2$  and  $\text{BaLn}_2\text{CoO}_5$  and of the tetravalent cobaltites  $\text{Ba}_2\text{CoO}_4$ . The trivalent cobaltite  $\text{CaCo}_2\text{O}_4$  exhibits the classical calcium

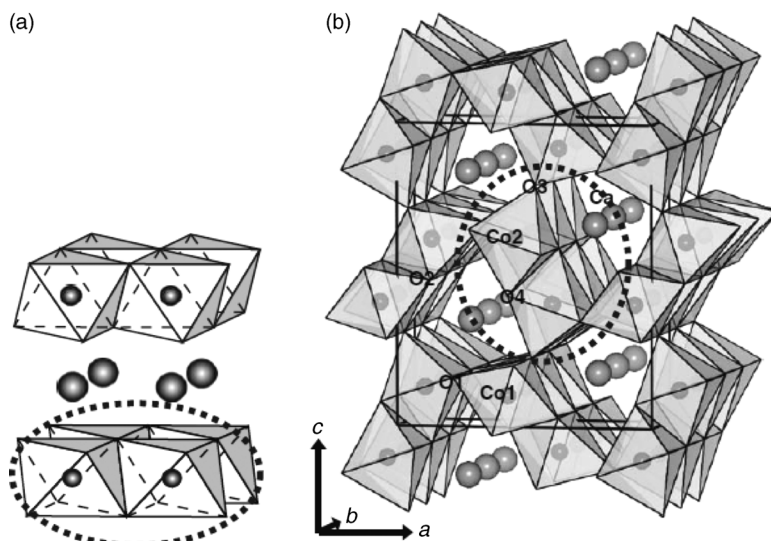


**Figure 1.40** Crystal structure of (a)  $\text{Na}_x\text{CoO}_2$  and (b)  $\text{CaCo}_2\text{O}_{4+\delta}$ . The dashed circles indicate the  $\text{CoO}_6$  octahedron network in the structure. Adapted from Ref. [335].

ferrite structure of  $\text{CaFe}_2\text{O}_4$  [333–335]. It crystallizes in the orthorhombic structure, space group  $Pnma$ , with lattice constants  $a \sim 8.79 \text{ \AA}$ ,  $b \sim 2.90 \text{ \AA}$ , and  $c \sim 10.28 \text{ \AA}$ . The three-dimensional octahedral framework of this oxide (Figure 1.40b) consists of double ribbons of edge-sharing octahedra running along  $b$ , and sharing their apices in order to form six-sided tunnels. In the double ribbons, the  $\text{CoO}_6$  octahedra are arranged in a manner similar to that in the  $[\text{CoO}_2]_\infty$  layers of  $\text{Na}_x\text{CoO}_2$  (Figure 1.40a), so that this structure can also be described as a very anisotropic structure with  $\text{Na}_x\text{CoO}_2$ -type ribbons, sharing their corners. In this framework, the six-sided tunnels are occupied by  $\text{Ca}^{2+}$  cations. It is quite remarkable that in this structure, the double ribbons of  $\text{CoO}_6$  octahedra exhibit short intrachain Co–Co distances, compared to the Co–Co distances between two adjacent ribbons. The Co–O bond lengths within the ribbons ( $\sim 1.943 \text{ \AA}$ ) are significantly shorter than the Co–O distances corresponding to the interconnection between the ribbons ( $\sim 1.973 \text{ \AA}$ ). This indicates that the cobalt atoms are situated close to the neighboring cobalt atoms in the same chain. Finally, bond valence sum calculations confirm that cobalt is trivalent, but suggest that there is a very slight tendency to cobalt disproportionation, with oxidation states of +3.17 and +2.94 for Co1 and Co2 sites, respectively.

The trivalent cobaltites  $\text{Ba}_6\text{Ln}_2\text{Co}_4\text{O}_{15}$ , with  $\text{Ln} = \text{La}, \text{Pr}$  exhibit an hexagonal symmetry,  $P6_3mc$  with cell parameters  $a \sim 11.8 \text{ \AA}$  and  $c \sim 7.0 \text{ \AA}$  [336, 337]. Their crystal structure (Figure 1.41) is of great interest: it consists of isolated units  $[\text{Co}_4\text{O}_{15}]^{18-}$  of four polyhedra sharing their apices, that is, one  $\text{CoO}_6$  octahedron linked to three  $\text{CoO}_4$  tetrahedra. The cohesion of the framework is ensured by the  $\text{Ln}^{3+}$  and  $\text{Ba}^{2+}$  cations that are sitting between these tetrameric units.

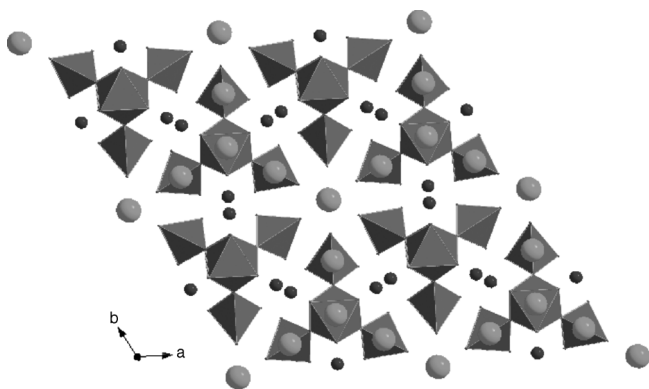


**Figure 1.41**  $\text{Ba}_6\text{La}_2\text{Co}_4\text{O}_{15}$ : projection of the structure along  $\bar{c}$ . Adapted from Ref. [336].

The  $\text{RbCoO}_2$  structure [338] is orthorhombic  $Pbca$  with  $a \sim 5.66 \text{ \AA}$ ,  $b \sim 11.35 \text{ \AA}$ , and  $c \sim 16.32 \text{ \AA}$  and cobalt is also trivalent. This phase exhibits a three-dimensional framework of corner-sharing  $\text{CoO}_4$  tetrahedra (Figure 1.42) forming six-sided tunnels, where the  $\text{Rb}^+$  cations are located. One observes two sorts of tunnels running along  $\bar{a}$  (Figure 1.42a) and a third sort of tunnels running along  $\bar{b}$  (Figure 1.42b). Consequently, it can be described as an intersecting tunnel structure.

The divalent cobaltite  $\text{BaCoO}_2$  exhibits a great similarity to  $\text{RbCoO}_2$ . The  $\text{BaCoO}_2$  structure [339] is trigonal,  $P3_12_1$  with lattice parameters  $a \sim 5.85 \text{ \AA}$  and  $c \sim 6.73 \text{ \AA}$ . Like  $\text{RbCoO}_2$ , it consists of a pure 3D framework of corner-sharing tetrahedra (Figure 1.43) forming two sorts of large six-sided tunnels running along  $\bar{c}$  (Figure 1.43a) and along  $\bar{a}$  (Figure 1.43b), respectively. The  $\text{Ba}^{2+}$  cations are located in the  $\langle 100 \rangle$  tunnels and at the border of the  $\langle 001 \rangle$  tunnels.

The divalent cobaltites  $\text{Ln}_2\text{BaCoO}_5$  exhibit two kinds of structures depending both on the size of the  $\text{Ln}^{3+}$  cation and on the synthesis conditions [107, 340–345].

The orthorhombic  $Immm$  structure is observed for larger and intermediate size cations,  $\text{Ln} = \text{Nd}, \text{Sm}, \text{Gd}, \text{Dy}, \text{and Er}$ , with cell parameters  $a \sim 3.7 \text{ \AA}$ ,  $\sim 5.8 \text{ \AA}$ , and  $c \sim 11.7 \text{ \AA}$ . This oxide is exceptional since it is to our knowledge the only divalent

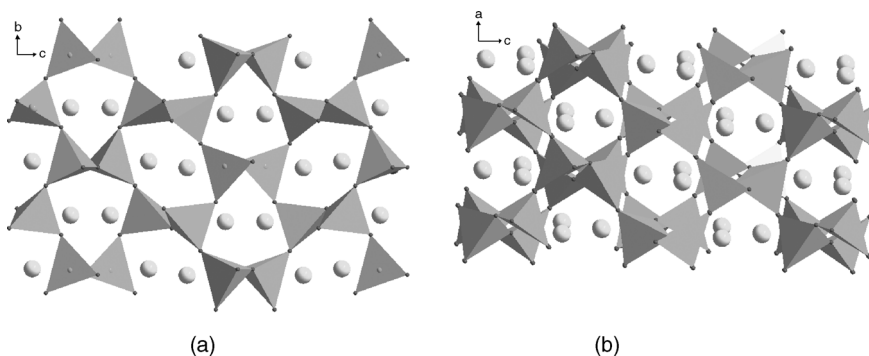


**Figure 1.42**  $\text{RbCoO}_2$ : view of the structure (a) along  $\bar{a}$  and (b) along  $\bar{b}$ . Adapted from Ref. [338].

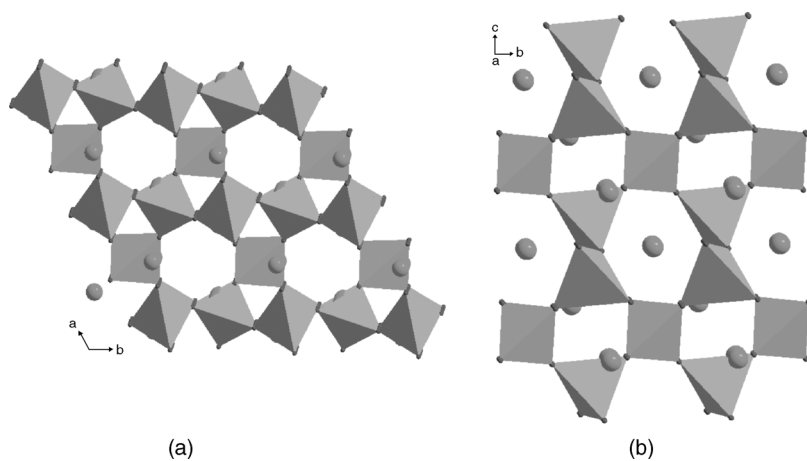


**Figure 1.43** BaCoO<sub>2</sub>: view of the structure (a) along  $\vec{c}$  and (b) along  $\vec{a}$ . Adapted from Ref. [339].

cobaltite that exhibits a unidimensional structure (Figure 1.44). It consists of octahedral perovskite-type chains of corner-sharing octahedra running along  $\vec{a}$ , the cohesion of the structure being ensured by the interchain Ba<sup>2+</sup> and Ln<sup>3+</sup> cations.

The orthorhombic *Pnma* structure is observed for Y and for Ln = Dy, Ho, Er, Tm, Yb, and Lu, with cell parameters  $a \sim 12.2 \text{ \AA}$ ,  $b \sim 5.7 \text{ \AA}$ , and  $c \sim 7.0 \text{ \AA}$ . In contrast to the latter, these oxides exhibit a pyramidal structure (Figure 1.45), which consists of rows of isolated CoO<sub>5</sub> pyramids running along  $\vec{b}$  interconnected through Ba<sup>2+</sup> and Ln<sup>3+</sup> cations.

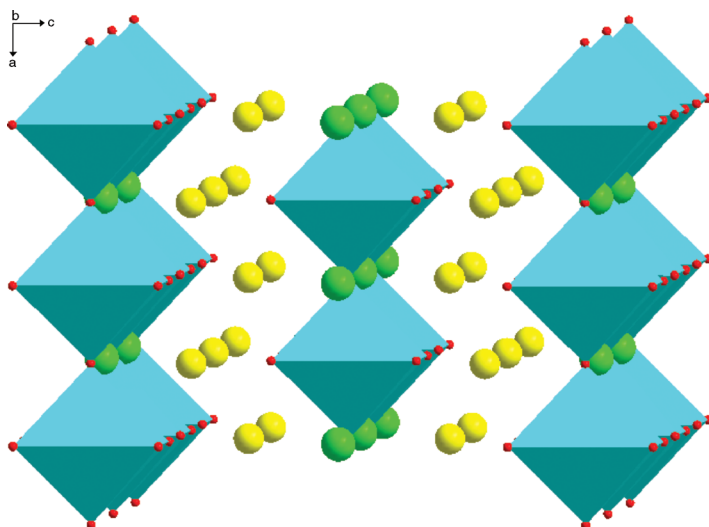


**Figure 1.44** Unidimensional structure of Ln<sub>2</sub>BaCoO<sub>5</sub> cobaltites, Ln = Nd, Sm, Eu, Gd, Dy, and Er. Adapted from Ref. [107].

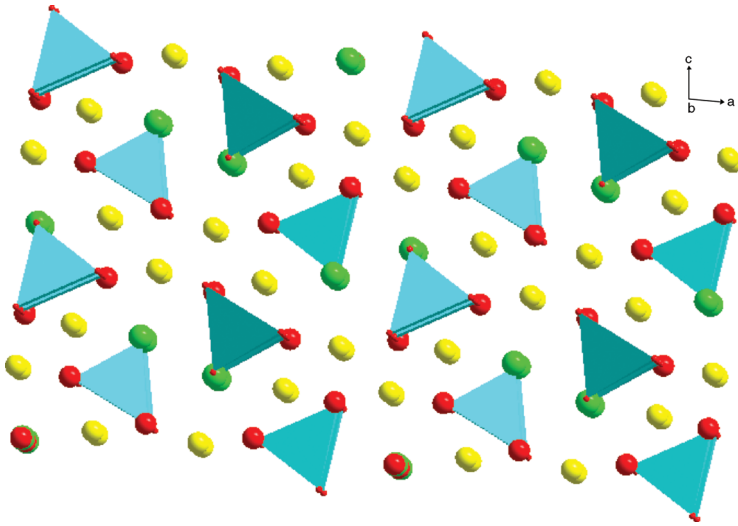


**Figure 1.45** Pyramidal structure of  $\text{Ln}_2\text{BaCoO}_5$  cobaltites  $\text{Ln} = \text{Dy, Ho, Er, Tm, Lu, and Y}$ . Adapted from Ref. [343].

The cobaltite  $\text{Ba}_2\text{CoO}_4$  exhibits two closely related structures, both made of isolated  $\text{CoO}_4$  tetrahedra interconnected through  $\text{Ba}^{2+}$  cations (Figure 1.46). The first form is orthorhombic  $Pnma$ , with  $a \sim 7.64 \text{ \AA}$ ,  $b \sim 5.85 \text{ \AA}$ , and  $c \sim 10.34 \text{ \AA}$  [346, 347], whereas the second form is monoclinic  $P2_1/n$ , with  $a \sim 5.89 \text{ \AA}$ ,  $b \sim 7.61 \text{ \AA}$ ,  $c \sim 10.39 \text{ \AA}$ , and

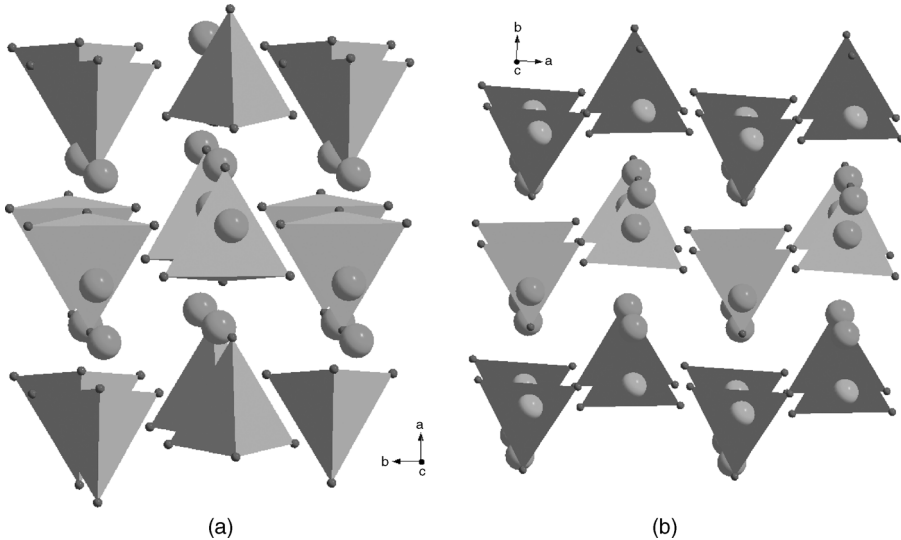


**Figure 1.46** Perspective view along  $\bar{c}$  of (a) the orthorhombic and (b) the monoclinic structure of  $\text{Ba}_2\text{CoO}_4$ . Adapted from Ref. [346, 348].

$\beta \sim 90^\circ.7$  [348]. In both structures, the  $\text{CoO}_4$  tetrahedra form rows running along  $\vec{c}$  and zigzag rows running along  $\vec{b}$  (Figure 1.46a) and  $\vec{a}$  (Figure 1.46b), respectively. In fact, the orthorhombic form (Figure 1.46a) differs from the monoclinic form (Figure 1.46b) by the fact that the apices of its tetrahedra are not all directed toward the same direction along  $\vec{c}$ . Note that the structure of the monoclinic form that exhibits one abnormally long Co–O bond in its tetrahedra ( $\sim 2.9 \text{ \AA}$ ) is still a matter of debate. It is also quite remarkable that  $\text{Ba}_2\text{CoO}_4$  is the only cobaltite, where tetravalent cobalt exhibits the tetrahedral coordination.

## References

- Demazeau, G. *et al.* (1974) *J. Solid State Chem.*, **9**, 202.
- Seikh, M.M. and Raveau, B. (2009) *Giant Magnetoresistance: New Research* (eds Adrian D. Torres and Daniel A. Perez), NOVA Publishers, pp. 107–156.
- Rao, C.N.R. *et al.* (2004) *Top. Curr. Chem.*, **234(II)**, 1–21.
- Ivanova, B.N. *et al.* (2009) *Physics-Uspokhi*, **52**, 789.
- Thornton, G. *et al.* (1986) *J. Solid State Chem.*, **61**, 301.
- Racah, P.M. and Goodenough, J.B. (1967) *Phys. Rev.*, **155**, 932.
- Kappatsch, A. *et al.* (1970) *J. Phys. France*, **31**, 369.
- Yakel, H.L. (1955) *Acta Crystallogr.*, **8**, 394.
- Wold, A. and Ward, R. (1954) *J. Amer. Chem. Soc.*, **76**, 1029.
- Tsubouchi, S. *et al.* (2004) *Phys. Rev. B*, **69**, 144406.
- Ghoshray, A. *et al.* (2004) *Phys. Rev. B*, **69**, 064424.
- Liu, X. *et al.* (1991) *J. Phys. Chem. Solids*, **52** (2), 441.
- Ivanova, B.N. *et al.* (2007) *Phys. Solid State*, **49**, 1498.
- Jirak, Z. *et al.* (2008) *Phys. Rev. B*, **78**, 014432.
- Muñoz, A. *et al.* (2006) *Phys. Rev. B*, **73**, 104442.
- Maris, G. *et al.* (2003) *Phys. Rev. B*, **67**, 224423.
- Haas, O. *et al.* (2004) *J. Solid State Chem.*, **177**, 1000.
- Zhou, J.-S. *et al.* (2005) *Phys. Rev. Lett.*, **94**, 065501.
- Zhou, J.-S. *et al.* (2005) *Phys. Rev. B*, **71**, 220103(R).
- Radaelli, P.G. *et al.* (2002) *Phys. Rev. B*, **66**, 094408.
- Knížek, K. *et al.* (2005) *Eur. Phys. J. B*, **47**, 213.
- Berggold, K. *et al.* (2008) *Phys. Rev. B*, **78**, 134402.
- Yan, J.-Q. *et al.* (2003) *Phys. Rev. B*, **68**, 104520.
- Sazonov, A.P. *et al.* (2006) *Cryst. Rep.*, **51**, 11.
- Mehta, A. *et al.* (1997) *J. Solid State Chem.*, **130**, 192.
- Knížek, K. *et al.* (2006) *Phys. Rev. B*, **73**, 214443.
- Mineshige, A. *et al.* (1996) *J. Solid State Chem.*, **121**, 423.
- Sunstrom, J.E. IV *et al.* (1998) *J. Solid State Chem.*, **139**, 388.
- James, M. *et al.* (2004) *J. Solid State Chem.*, **177**, 1886.
- Señaris-Rodriguez, M.A. *et al.* (1995) *J. Solid State Chem.*, **118**, 323.
- Mira, J. *et al.* (1999) *Phys. Rev. B*, **59**, 123.
- Caciuffo, R. *et al.* (1999) *Phys. Rev. B*, **59**, 1068.
- Iguchi, E. *et al.* (1998) *J. Phys. Condens. Matter*, **10**, 8999.
- Nam, D.N.H. *et al.* (1999) *Phys. Rev. B*, **59**, 4189.
- Wu, J. *et al.* (2003) *Phys. Rev. B*, **67**, 174408.
- Takami, T. *et al.* (2007) *Phys. Rev. B*, **76**, 144116.
- Raveau, B. *et al.* (2005) *J. Phys. Condens. Matter*, **17**, 7371.
- Bezdzicka, P. *et al.* (1993) *Z. Anorg. Allg. Chem.*, **619**, 7.
- Deng, Z.Q. *et al.* (2006) *J. Solid State Chem.*, **179**, 362.

- 40 Taguchi, H. *et al.* (1980) *Mater. Res. Bull.*, **15**, 165.
- 41 Efimova, E. *et al.* (2008) *J. Phys. Chem. Solids*, **69**, 2187.
- 42 Ang, R. *et al.* (2006) *Solid State Commun.*, **138**, 255.
- 43 Tong, W. *et al.* (2004) *J. Phys. Condens. Matter*, **16**, 103.
- 44 Ganguly, R. *et al.* (2002) *J. Phys. Condens. Matter*, **14**, 8595.
- 45 Stauffer, D.D. *et al.* (2004) *Phys. Rev. B*, **70**, 214414.
- 46 Mahendiran, R. *et al.* (2003) *Phys. Rev. B*, **68**, 024427.
- 47 Krimmel, A. *et al.* (2001) *Phys. Rev. B*, **64**, 224404.
- 48 Luo, W. *et al.* (2006) *J. Magn. Magn. Mater.*, **305**, 509.
- 49 Balamurugan, S. *et al.* (2006) *J. Solid State Chem.*, **179**, 2231.
- 50 Sathe, V.G. *et al.* (1996) *J. Phys. Condens. Matter*, **8**, 3889.
- 51 Kriener, M. *et al.* (2004) *Phys. Rev. B*, **69**, 094417.
- 52 Ganguly, R. *et al.* (2001) *J. Phys. Condens. Matter*, **13**, 10911.
- 53 Fauth, F. *et al.* (2001) *Phys. Rev. B*, **65**, 060401(R).
- 54 Rautama, E.L. *et al.* (2008) *Chem. Mater.*, **20**, 2742.
- 55 Kundu, A.K. *et al.* (2007) *Phys. Rev. B*, **76**, 184432.
- 56 Zock, Ch. *et al.* (1995) *J. Magn. Magn. Mater.*, **150**, 253.
- 57 Fita, I. *et al.* (2005) *Phys. Rev. B*, **71**, 214404.
- 58 Kundu, A.K. *et al.* (2004) *J. Phys. Condens. Matter*, **16**, 7955.
- 59 Phelan, D. *et al.* (2007) *Phys. Rev. B*, **76**, 104111.
- 60 Kundu, A.K. *et al.* (2004) *J. Phys. Condens. Matter*, **16**, 415.
- 61 Grenier, J.G. *et al.* (1979) *Mater. Res. Bull.*, **14**, 831.
- 62 Takeda, Y. *et al.* (1986) *Z. Anorg. Allg. Chem.*, **540**, 259.
- 63 Takeda, T. *et al.* (1972) *J. Phys. Soc. Jpn.*, **33**, 970.
- 64 Muñoz, A. *et al.* (2008) *Phys. Rev. B*, **78**, 054404.
- 65 Harrison, W.T.A. *et al.* (1995) *J. Chem. Soc. Chem. Commun.*, 1953.
- 66 de la Calle, C. *et al.* (2008) *Solid State Sci.*, **10**, 1924.
- 67 Nakatsuka, A. *et al.* (2004) *Acta Cryst. C*, **60**, i59-i60.
- 68 Takeda, T. *et al.* (1969) *J. Phys. Soc. Jpn.*, **26**, 1320.
- 69 Le Toquin, R. *et al.* (2006) *J. Am. Chem. Soc.*, **128**, 13161.
- 70 Jaya, S.M. *et al.* (1991) *Phys. Rev. B*, **43**, 13274.
- 71 Pardo, V. *et al.* (2008) *Physica B*, **403**, 1636.
- 72 Boulahya, K. *et al.* (2009) *Chem. Mater.*, **21**, 2045.
- 73 Yamaura, K. *et al.* (1999) *J. Solid State Chem.*, **146**, 96.
- 74 de la Calle, C. *et al.* (2009) *Dalton Trans.*, 4104.
- 75 Balamurugan, S. *et al.* (2005) *J. Solid State Chem.*, **178**, 3431.
- 76 Kim, M.G. *et al.* (1997) *Physica B*, **229**, 338.
- 77 Im, Y.S. *et al.* (1997) *J. Phys. Chem. Solids*, **58**, 2079.
- 78 Pei, J. *et al.* (2009) *Mater. Lett.* **63**, 1459.
- 79 Vidyasagar, K. *et al.* (1984) *Inorg. Chem.*, **23**, 1206.
- 80 Anderson, M.T. *et al.* (1993) *Chem. Mater.*, **5**, 151.
- 81 Sharma, N. *et al.* (2004) *Electrochim. Acta*, **49**, 1035.
- 82 Boullay, P. *et al.* (2009) *Phys. Rev. B*, **79**, 184108.
- 83 Withers, R.L. *et al.* (2003) *J. Solid State Chem.*, **174**, 198.
- 84 Maignan, A. *et al.* (2005) *J. Solid State Chem.*, **178**, 868.
- 85 Istomin, S.Y. *et al.* (2004) *Solid State Sci.*, **6**, 539.
- 86 Kolesnik, S. *et al.* (2006) *Phys. Rev. B*, **73**, 214440.
- 87 Baszczuk, A. *et al.* (2007) *Phys. Rev. B*, **76**, 134407.
- 88 Motohashi, T. *et al.* (2005) *Appl. Phys. Lett.*, **86**, 192504.
- 89 Istomin, Ya.S. *et al.* (2003) *Chem. Mater.*, **15**, 4012.
- 90 James, M. *et al.* (2007) *J. Solid State Chem.*, **180**, 2233.
- 91 James, M. *et al.* (2004) *Solid State Sci.*, **6**, 655.
- 92 Goossens, D.J. *et al.* (2004) *Phys. Rev. B*, **69**, 134411.

- 93 van Doorn, R.H.E. *et al.* (2000) *Solid State Ionics*, **128**, 65.
- 94 Streule, S. *et al.* (2006) *Phys. Rev. B*, **73**, 024423.
- 95 Streule, S. *et al.* (2004) *Physica B*, **350**, e281.
- 96 Pearson, D.H. *et al.* (1993) *Phys. Rev. B*, **47**, 8471.
- 97 Kurata, H. *et al.* (1993) *Phys. Rev. B*, **48**, 2102.
- 98 Wang, Z.L. *et al.* (1998) *Phil. Mag. B*, **77**, 49.
- 99 Barbey, L. *et al.* (1994) *J. Solid State Chem.*, **112**, 148.
- 100 Maignan, A. *et al.* (1999) *J. Solid State Chem.*, **142**, 247.
- 101 Burley, J.C. *et al.* (2003) *J. Solid State Chem.*, **170**, 339.
- 102 Vogt, T. *et al.* (2000) *Phys. Rev. Lett.*, **84**, 2969.
- 103 Fauth, F. *et al.* (2001) *Eur. Phys. J. B*, **21**, 163.
- 104 Barbey, L. *et al.* (1995) *J. Solid State Chem.*, **115**, 514.
- 105 Er-rakho, L. *et al.* (1988) *J. Solid State Chem.*, **73**, 531.
- 106 Millange, F. *et al.* (1998) *Chem. Mater.*, **10**, 1974.
- 107 Mevs, H. *et al.* (1989) *Z. Anorg. Allg. Chem.*, **574**, 172.
- 108 Frontera, C. *et al.* (2004) *Phys. Rev. B*, **70**, 184428.
- 109 Streule, S. *et al.* (2006) *Phys. Rev. B*, **73**, 094203.
- 110 Frontera, C. *et al.* (2002) *Phys. Rev. B*, **65**, 180405(R).
- 111 Kusuya, H. *et al.* (2001) *J. Phys. Soc. Jpn.*, **70**, 3577.
- 112 Podlesnyak, A. *et al.* (2006) *Physica B*, **378**, 537.
- 113 Plakhty, V.P. *et al.* (2005) *Phys. Rev. B*, **71**, 214407.
- 114 Barito, S.N. *et al.* (2008) *J. Cryst. Growth*, **310**, 1867.
- 115 Jorgensen, J.-E. *et al.* (2008) *Phys. Rev. B*, **77**, 024427.
- 116 Moritomo, Y. *et al.* (2000) *Phys. Rev. B*, **61**, R13325.
- 117 Khalyavin, D.D. *et al.* (2007) *Phys. Rev. B*, **75**, 134407.
- 118 Akahoshi, D. *et al.* (2001) *J. Solid State Chem.*, **156**, 355.
- 119 Fauth, F. *et al.* (2002) *Phys. Rev. B*, **66**, 184421.
- 120 Seikh, M.M. *et al.* (2008) *Chem. Mater.*, **20**, 231.
- 121 Taskin, A.A. *et al.* (2005) *Phys. Rev. B*, **71**, 134414.
- 122 Soda, M. *et al.* (2003) *J. Phys. Soc. Jpn.*, **72**, 1729.
- 123 Roy, S. *et al.* (2005) *Phys. Rev. B*, **71**, 024419.
- 124 Rautama, E.L. *et al.* (2009) *Chem. Mater.*, **21**, 102.
- 125 Caignaert, V. *et al.* (1999) *Chem. Mater.*, **11**, 930.
- 126 Nakajima, T. *et al.* (2005) *J. Phys. Soc. Jap.*, **74**, 1572.
- 127 Suard, E. *et al.* (2000) *Physica B*, **276–278**, 254.
- 128 Taguchi, H. *et al.* (1977) *Acta Cryst. B*, **33**, 1299.
- 129 Gushee, B.E. *et al.* (1977) *J. Am. Chem. Soc.*, **79**, 5601.
- 130 Felser, C. *et al.* (1999) *J. Solid State Chem.*, **146**, 411.
- 131 de la Calle, C. *et al.* (2008) *Z. Naturforsch. B. Anorg. Chem.*, **63**, 647.
- 132 Pardo, V. *et al.* (2006) *J. Magn. Magn. Mater.*, **300**, 48.
- 133 Hebert, S. *et al.* (2007) *J. Magn. Magn. Mater.*, **316**, 394.
- 134 Parras, M. *et al.* (1995) *J. Solid State Chem.*, **120**, 327.
- 135 Boulaya, K. *et al.* (2005) *Phys. Rev. B*, **71**, 144402.
- 136 Miranda, L. *et al.* (2008) *Chem. Mater.*, **20**, 2818.
- 137 Jakobson, A. *et al.* (1980) *J. Solid State Chem.*, **35**, 334.
- 138 Miranda, L. *et al.* (2007) *Chem. Mater.*, **19**, 1503.
- 139 Maignan, A. *et al.* (2006) *J. Solid State Chem.*, **179**, 1852.
- 140 Darriet, J. *et al.* (2002) *Chem. Mater.*, **14**, 3349.
- 141 Wang, X.L. *et al.* (2005) *Phys. Rev. B*, **72**, 064401.
- 142 Wang, X.L. *et al.* (2005) *J. Appl. Phys.*, **97**, 10M519.
- 143 Matsuno, J. *et al.* (2004) *Phys. Rev. Lett.*, **93**, 167202.
- 144 Kajitani, T. *et al.* (1990) *J. Phys. Soc. Jpn.*, **59**, 562.

- 145 Ang, R. *et al.* (2008) *J. Phys. D Appl. Phys.*, **41**, 215009.
- 146 Yamada, K. *et al.* (1989) *Phys. Rev. B*, **39**, 2336.
- 147 Chichev, A.V. *et al.* (2006) *Phys. Rev. B*, **74**, 134414.
- 148 Sanchez-Andujar, M. *et al.* (2004) *Solid State Sci.*, **6**, 21.
- 149 Moritomo, Y. *et al.* (1997) *Phys. Rev. B*, **55**, R14725.
- 150 Zaliznyak, I.A. *et al.* (2000) *Phys. Rev. Lett.*, **85**, 4353.
- 151 Matsuura, T. *et al.* (1988) *J. Phys. Chem. Solids*, **49**, 1403.
- 152 James, M. *et al.* (2006) *J. Alloys Compd.*, **419**, 201.
- 153 Cwik, M. *et al.* (2009) *Phys. Rev. Lett.*, **102**, 057201.
- 154 Ang, R. *et al.* (2008) *J. Phys. D Appl. Phys.*, **41**, 045404.
- 155 Ganguly, R. *et al.* (1984) *J. Solid State Chem.*, **53**, 193.
- 156 Shimada, Y. *et al.* (2006) *Phys. Rev. B*, **73**, 134424.
- 157 Castro-García, S. *et al.* (2001) *J. Alloys Compd.*, **323–324**, 710.
- 158 Dann, S.E. *et al.* (1992) *J. Solid State Chem.*, **97**, 179.
- 159 Dann, S.E. *et al.* (1995) *J. Solid State Chem.*, **115**, 499.
- 160 Yamaura, K. *et al.* (1999) *J. Solid State Chem.*, **146**, 277.
- 161 Viciu, L. *et al.* (2006) *J. Solid State Chem.*, **179**, 500.
- 162 Nguyen, N. *et al.* (1980) *Mater. Res. Bull.*, **15**, 891.
- 163 Gillie, L.J. *et al.* (2008) *Chem. Mater.*, **20**, 6231.
- 164 Yamaura, K. *et al.* (1999) *Phys. Rev. B*, **60**, 9623.
- 165 Yamaura, K. *et al.* (2001) *Phys. Rev. B*, **63**, 064401.
- 166 Siwen, L. *et al.* (1995) *J. Solid State Chem.*, **114**, 286.
- 167 Siwen, L. *et al.* (1994) *Mater. Res. Bull.*, **29**, 993.
- 168 Hickey, P.J. *et al.* (2007) *Phys. Rev. B*, **75**, 024113.
- 169 Demont, A. *et al.* (2008) *J. Solid State Chem.*, **181**, 1314.
- 170 Hill, J.M. *et al.* (2006) *Phys. Rev. B*, **74**, 174417.
- 171 Pelloquin, D. *et al.* (2005) *Solid State Sci.*, **7**, 853.
- 172 Pelloquin, D. *et al.* (2005) *Chem. Mater.*, **17**, 773.
- 173 Motohashi, T. *et al.* (2005) *Chem. Mater.*, **17**, 6256.
- 174 Raveau, B., Michel, C., Hervieu, M., Provost, J., and Studer, F. (1990) Earlier and recent aspects of superconductivity, in *Springer Series in Materials Sciences*, vol. 90 (eds J.G. Berdnorz and K.A. Müller), Springer, Berlin, pp. 66–95.
- 175 Doumerc, J.P. *et al.* (2001) *J. Mater. Chem.*, **11**, 78.
- 176 Maignan, A. *et al.* (2002) *J. Mater. Chem.*, **12**, 1009.
- 177 Masset, A.C. *et al.* (2000) *Int. J. Inorg. Mater.*, **2**, 687.
- 178 Courjault, S. *et al.* (2002) *Z. Anorg. Allgem. Chem.*, **628**, 2057.
- 179 Pelloquin, D. *et al.* (1999) *J. Solid State Chem.*, **148**, 108.
- 180 Tarascon, J.M. *et al.* (1989) *Phys. Rev. B*, **39**, 11587.
- 181 Jakubowicz, N. *et al.* (1999) *J. Phys. Condens. Matter*, **11**, 3997.
- 182 Tarascon, J.M. *et al.* (1990) *Physica C*, **167**, 20.
- 183 Jakubowicz, N. *et al.* (2000) *J. Phys. Condens. Matter*, **12**, 5371.
- 184 Pelloquin, D. *et al.* (1999) *Chem. Mater.*, **11**, 84.
- 185 Perez, O. *et al.* (2002) *Acta Cryst. B*, **58**, 191.
- 186 Smith, W.L. *et al.* (1973) *Acta Cryst. B*, **29**, 362.
- 187 Tombs, N.C. *et al.* (1950) *Nature (London)*, **165**, 442.
- 188 Roth, W.L. (1964) *J. Phys. Chem. Solids*, **25**, 1.
- 189 Zhu, H.T. *et al.* (2008) *Physica B*, **403**, 3141.
- 190 Mousavand, T. *et al.* (2009) *Phys. Rev. B*, **79**, 144411.
- 191 Casas-Cabanas, M. *et al.* (2009) *Chem. Mater.*, **21**, 1939.
- 192 Xu, R. *et al.* (2009) *J. Solid State Chem.*, **182**, 3177.
- 193 Shen, X.-P. *et al.* (2008) *Appl. Phys. A*, **91**, 47.
- 194 Keng, P.Y. *et al.* (2009) *ACS Nano*, **3**, 3143.
- 195 Driessens, F. *et al.* (1968) *J. Inorg. Nucl. Chem.*, **30**, 747.

- 196 Delorme, C. (1958) *Bull. Soc. Franc. Miner. Crist.*, **81**, 19.
- 197 Baussart, H. *et al.* (1977) *C. R. Acad. ScL Paris*, **284**, C– 735.
- 198 Holgersson, S. *et al.* (1929) *Z. Anorg. Allg. Chem.*, **183**, 384.
- 199 Klissurski, D. *et al.* (1994) *J. Mater. Sci. Lett.*, **29**, 285.
- 200 Angelov, S. *et al.* (1982) *Mater. Res. Bull.*, **17**, 235.
- 201 Mehandjiev, D. *et al.* (1981) *Thermochim. Acta.*, **51**, 343.
- 202 Zhecheva, E. *et al.* (1991) *Mater. Res. Bull.*, **26**, 1315.
- 203 Toriumi, K. *et al.* (1978) *Acta Cryst. B*, **34**, 1093.
- 204 Casado, P.G. *et al.* (1984) *J. Solid. State Chem.*, **52**, 187.
- 205 Tristan, N. *et al.* (2008) *Phys. Rev. B*, **77**, 094412.
- 206 Lawes, G. *et al.* (2006) *Phys. Rev. B*, **74**, 024413.
- 207 Wickham, D.G. *et al.* (1958) *J. Phys. Chem. Solids*, **7**, 351.
- 208 Meena, P.L. *et al.* (2009) *J. Appl. Phys.*, **106**, 024105.
- 209 Jansen, V.M. *et al.* (1974) *Z. Anorg. Allgem. Chem.*, **408**, 104.
- 210 Fouassier, C. *et al.* (1973) *J. Solid State Chem.*, **6**, 532.
- 211 Cushing, B. L. *et al.* (1998) *J. Solid State Chem.*, **141**, 385.
- 212 Takada, K. *et al.* (2003) *Nature (London)*, **422**, 53.
- 213 Zhou, T. *et al.* (2009) *J. Mater. Chem.*, **19**, 1123.
- 214 Ono, Y. *et al.* (2002) *J. Solid State Chem.*, **166**, 177.
- 215 Zhou, T. *et al.* (2008) *J. Mater. Chem.*, **18**, 1342.
- 216 Ono, Y. *et al.* (2001) *J. Phys. Soc. Jpn.*, **70** (Suppl. A), 235.
- 217 Huang, Q. *et al.* (2004) *J. Phys. Condens. Matter*, **16**, 5803.
- 218 Foo, M.L. *et al.* (2004) *Phys. Rev. Lett.*, **92**, 247001.
- 219 Huang, Q. *et al.* (2004) *Phys. Rev. B*, **70**, 184110.
- 220 Zandbergen, H.W. *et al.* (2004) *Phys. Rev. B*, **70**, 024101.
- 221 Roger, M. (2007) *et al. Nature (London)*, **445**, 631.
- 222 Zhang, P. *et al.* (2005) *Phys. Rev. B*, **71**, 153102.
- 223 Wang, Y. *et al.* (2007) *Phys. Rev. B*, **76**, 094101.
- 224 Geck, J. *et al.* (2006) *Phys. Rev. Lett.*, **97**, 106403.
- 225 Meng, Y.S. *et al.* (2005) *Phys. Rev. B*, **72**, 172103.
- 226 Lemmens, P. *et al.* (2006) *Phys. Rev. Lett.*, **96**, 167204.
- 227 Hinuma, Y. *et al.* (2008) *Phys. Rev. B*, **77**, 224111.
- 228 Meng, Y.S. *et al.* (2008) *J. Chem. Phys.*, **128**, 104708.
- 229 Ning, F.L. *et al.* (2008) *Phys. Rev. Lett.*, **100**, 086405.
- 230 Gavilano, J.L. *et al.* (2005) *Physica B*, **359–361**, 1237.
- 231 Gavilano, J.L. *et al.* (2004) *Phys. Rev. B*, **69**, 100404.
- 232 Bernhard, C. *et al.* (2004) *Phys. Rev. Lett.*, **93**, 167003.
- 233 Pollet, M. *et al.* (2009) *Inorg. Chem.*, **48**, 9671.
- 234 Blangero, M. *et al.* (2005) *Inorg. Chem.*, **44**, 9299.
- 235 Johnston, W.D. *et al.* (1958) *J. Phys. Chem. Solids*, **7**, 1.
- 236 Orman, H.J. *et al.* (1984) *Acta Cryst. C*, **40**, 12.
- 237 Akimoto, J. *et al.* (1998) *J. Solid State Chem.*, **141**, 298.
- 238 Holzapfel, M. *et al.* (2009) *J. Solid State Chem.*, **156**, 470.
- 239 Donakhala, N. *et al.* (2002) *J. Solid State Chem.*, **163**, 406.
- 240 Gummow, R.J. *et al.* (1993) *Mater. Res. Bull.*, **28**, 235; (1993) *Mater. Res. Bull.*, **28**, 1177.
- 241 Gummow, R.J. *et al.* (1992) *Mater. Res. Bull.*, **27**, 327.
- 242 Hertz, J.T. *et al.* (2008) *Phys. Rev. B*, **77**, 075119.
- 243 Laubach, S. *et al.* (2009) *Phys. Chem. Chem. Phys.*, **11**, 3278.
- 244 Takahashi, Y. *et al.* (2007) *J. Solid State Chem.*, **180**, 313.
- 245 Wang, X. *et al.* (2005) *Phys. Rev. B*, **72**, 224102.
- 246 Takahashi, Y. *et al.* (2007) *J. Phys. Condens. Matter*, **19**, 436202.
- 247 Carlier, D. *et al.* (2004) *Inorg. Chem.*, **43**, 914.
- 248 Huang, R. *et al.* (2011) *Appl. Phys. Lett.*, **98**, 051913.
- 249 Carlier, D. *et al.* (2001) *Solid State Ionics*, **144**, 263.

- 250 Boullay, P. *et al.* (1996) *Chem. Mater.*, **8**, 1482.
- 251 Boullay, P. *et al.* (1998) *Chem. Mater.*, **10**, 92.
- 252 Leligny, H. *et al.* (1999) *C. R. Acad. Sci., Ser. IIC Chim.*, **2**, 409.
- 253 Hervieu, M. *et al.* (1999) *J. Solid State Chem.*, **142**, 305.
- 254 Leligny, H. *et al.* (2000) *Acta Cryst. B*, **56**, 173.
- 255 Hervieu, M. *et al.* (2003) *Phys. Rev. B*, **67**, 045112.
- 256 Maignan, A. *et al.* (2002) *Chem. Mater.*, **14**, 1231.
- 257 Klein, Y. *et al.* (2005) *J. Appl. Phys.*, **98**, 013701.
- 258 Morita, Y. *et al.* (2004) *J. Solid State Chem.*, **177**, 3149.
- 259 Masset, A.C. *et al.* (2000) *Phys. Rev. B*, **62**, 166.
- 260 Brisi, C. *et al.* (1968) *Ann. Chim. (Rome)*, **58**, 676.
- 261 Woermann, E. *et al.* (1970) *J. Inorg. Nucl. Chem.*, **32**, 1455.
- 262 Li, S. *et al.* (1999) *J. Mater. Chem.*, **9**, 1659.
- 263 Li, S. *et al.* (2000) *Chem. Mater.*, **12**, 2424.
- 264 Lambert, S. *et al.* (2001) *J. Solid State Chem.*, **160**, 322.
- 265 Grebille, D. *et al.* (2004) *J. Appl. Cryst.*, **37**, 823.
- 266 Miyazaki, Y. *et al.* (2002) *J. Phys. Soc. Jpn.*, **71**, 491.
- 267 Nagatsukawa, H. *et al.* (2007) *Jap. J. Appl. Phys.*, **46**, 3004.
- 268 Ling, C.D. *et al.* (2007) *J. Solid State Chem.*, **180**, 1446.
- 269 Muguerra, H. *et al.* (2008) *Acta Cryst. B*, **64**, 144.
- 270 Tyson, T.A. *et al.* (2009) *Phys. Rev. B*, **79**, 024109.
- 271 Yang, G. *et al.* (2008) *Phys. Rev. B*, **78**, 153109.
- 272 Itahara, H. *et al.* (2005) *J. Am. Chem. Soc.*, **127**, 6367.
- 273 Li, S. *et al.* (2001) *Ceramics Int.*, **27**, 321.
- 274 Wang, L.B. *et al.* (2002) *J. Appl. Phys.*, **92**, 124.
- 275 Maignan, A. *et al.* (2002) *J. Appl. Phys.*, **92**, 1964.
- 276 Pelloquin, D. *et al.* (2002) *Chem. Mater.*, **14**, 3100.
- 277 Pelloquin, D. *et al.* (2003) *J. Solid State Chem.*, **170**, 374.
- 278 Matsubara, I. *et al.* (2001) *J. Appl. Phys.*, **90**, 462.
- 279 Grebille, D. *et al.* (2007) *Acta Cryst. B*, **63**, 373.
- 280 Kobayashi, W. *et al.* (2009) *J. Phys. Condens. Matter*, **21**, 235404.
- 281 Karppinen, M. *et al.* (2004) *Chem. Mater.*, **16**, 2790.
- 282 Yamamoto, T. *et al.* (2002) *Phys. Rev. B*, **65**, 184434.
- 283 Pelloquin, D. *et al.* (2004) *Solid State Sci.*, **6**, 167.
- 284 Miyazaki, Y. *et al.* (2002) *Jpn. J. Appl. Phys. Part 2*, **41**, 1849.
- 285 Maignan, A. *et al.* (2003) *J. Phys. Condens. Matter*, **15**, 2711.
- 286 Itoh, T. *et al.* (2000) *Jpn. J. Appl. Phys. Part 1*, **39**, 6658.
- 287 Liu, H.Q. *et al.* (2009) *Curr. Appl. Phys.*, **9**, 409.
- 288 Créon, N. *et al.* (2006) *Chem. Mater.*, **18**, 5355.
- 289 Maignan, A. *et al.* (2002) *Cryst. Eng.*, **5**, 365.
- 290 Miyazaki, Y. (2000) *et al.* *Jpn. J. Appl. Phys. Part 2*, **39**, L531.
- 291 Li, D. *et al.* (2006) *J. Appl. Phys.*, **99**, 053709.
- 292 Liu, C.-J. *et al.* (2006) *Appl. Phys. Lett.*, **89**, 204102.
- 293 Zhao, B.C. *et al.* (2006) *J. Appl. Phys.*, **99**, 073906.
- 294 Zhao, B.C. *et al.* (2006) *Phys. Rev. B*, **74**, 144417.
- 295 Pelloquin, D. *et al.* (2005) *J. Solid State Chem.*, **178**, 769.
- 296 Sun, J. *et al.* (2006) *Inorg. Chem.*, **45**, 9151.
- 297 Müller-Buschbaum, H. *et al.* (1996) *Z. Naturforsch. B*, **51**, 343.
- 298 Valldor, M. *et al.* (2002) *Solid State Sci.*, **4**, 923.
- 299 Valldor, M. (2004) *J. Phys. Condens. Matter*, **16**, 9209.
- 300 Valldor, M. (2004) *Solid State Sci.*, **6**, 251.
- 301 Tsipis, E.V. *et al.* (2005) *J. Solid State Electrochem.*, **9**, 547.
- 302 Tsipis, E.V. *et al.* (2005) *Mater. Chem. Phys.*, **92**, 33.
- 303 Bychkov, G.L. *et al.* (2005) *J. Cryst. Growth*, **275**, 813.
- 304 Caignaert, V. *et al.* (2006) *Solid State Sci.*, **8**, 1160.

- 305 Juarez-Arellano, E.A. *et al.* (2009) *Phys. Rev. B*, **79**, 064109.
- 306 Huq, A. *et al.* (2006) *J. Solid State Chem.*, **179**, 1136.
- 307 Nakayama, N. *et al.* (2006) *J. Magn. Magn. Mater.*, **300**, 98.
- 308 Gatal'skaya, V.I. *et al.* (2007) *Phys. Solid State*, **49**, 1125.
- 309 Khalyavin, D.D. *et al.* (2009) *Phys. Rev. B*, **80**, 144107.
- 310 Caignaert, V. *et al.* (2009) *Solid State Commun.*, **149**, 453.
- 311 Caignaert, V. *et al.* (2010) *Phys. Rev. B*, **81**, 094417.
- 312 Kadota, S. *et al.* (2008) *Chem. Mater.*, **20**, 6378.
- 313 Karpinnen, M. *et al.* (2006) *Chem. Mater.*, **18**, 490.
- 314 Bychkov, G.L. *et al.* (2005) *Cryst. Res. Technol.*, **40**, 395.
- 315 Soda, M. *et al.* (2006) *J. Phys. Soc. Jpn.*, **75**, 054707.
- 316 Chapon, L.C. *et al.* (2006) *Phys. Rev. B*, **74**, 172401.
- 317 Valkeapää, M. *et al.* (2007) *Chem. Lett.*, **36**, 1368.
- 318 Chmaissem, O. *et al.* (2008) *J. Solid State Chem.*, **181**, 664.
- 319 Jia, Y. *et al.* (2009) *J. Am. Chem. Soc.*, **131**, 4880.
- 320 Tsipis, E.V. *et al.* (2009) *J. Solid State Chem.*, **182**, 640.
- 321 Maignan, A. *et al.* (2008) *Solid State Commun.*, **147**, 470.
- 322 Maignan, A. *et al.* (2000) *Eur. Phys. J. B.*, **15**, 657.
- 323 Fjellvåg, H. *et al.* (1996) *J. Solid State Chem.*, **124**, 190.
- 324 Nguyen, T.N. *et al.* (1995) *J. Solid State Chem.*, **117**, 300.
- 325 Burnus, T. *et al.* (2006) *Phys. Rev. B*, **74**, 245111.
- 326 Nguyen, T.N. *et al.* (1995) *MRS Symp. Proc.*, **376**, 603.
- 327 Vajenine, G.V. *et al.* (1996) *Chem. Phys.*, **204**, 469.
- 328 Chupakhina, T.I. *et al.* (2004) *Russ. J. Inorg. Chem.*, **49**, 661.
- 329 Breard, Y. *et al.* (2001) *Solid State Commun.*, **118**, 517.
- 330 Melkozerova, M.A. *et al.* (2005) *Russ. J. Phys. Chem.*, **79**, 1197.
- 331 Boulahya, K. *et al.* (1999) *J. Solid State Chem.*, **145**, 116.
- 332 Cheng, J.-G. *et al.* (2009) *Phys. Rev. B*, **79**, 184414.
- 333 Shizuya, M. *et al.* (2007) *J. Solid State Chem.*, **180**, 2550.
- 334 Isobe, M. *et al.* (2009) *Physica C*, **469**, 948.
- 335 Isobe, M. *et al.* (2009) *J. Elec. Mater.*, **38**, 1166.
- 336 Müller-Buschbaum, H. *et al.* (1996) *Z. Naturforsch. B*, **51**, 453.
- 337 Mevs, H. *et al.* (1990) *Z. Anorg. Allg. Chem.*, **584**, 114.
- 338 Jansen, V.M. *et al.* (1975) *Z. für Anorg. Allgem. Chem.*, **417**, 31.
- 339 Spitsenbergen, U. (1960) *Acta Cryst.*, **13**, 197.
- 340 Riihl, H. *et al.* (1989) *J. Less Common Metals*, **152**, 139.
- 341 Hernandez-Velasco, J. *et al.* (1994) *J. Solid State Chem.*, **110**, 329.
- 342 Hernandez-Velasco, J. *et al.* (1993) *J. Alloys Compd.*, **198**, 63.
- 343 Rüter, I. *et al.* (1989) *Z. Anorg. Allgem. Chem.*, **573**, 89.
- 344 Klüver, E. *et al.* (1993) *Z. Anorg. Allgem. Chem.*, **619**, 421.
- 345 Hernandez-Velasco, J. *et al.* (1994) *J. Alloys Compd.*, **203**, 15.
- 346 Mattausch, H.J. *et al.* (1971) *Z. Anorg. Allgem. Chem.*, **386**, 1.
- 347 Boulahya, K. *et al.* (2006) *Chem Mater.*, **18**, 3898.
- 348 Boulahya, K. *et al.* (2000) *Solid State Sci.*, **2**, 57.